Master's thesis

NTNU
Norwegian University of Science and Technology
Faculty of Engineering
Department of Civil and Environmental Engineering

Adrian Weidemann Skagseth

In-situ characterization of Øysand sand with CPTU add-on tool Flow Cone and HPT

Master's thesis in Civil and Environmental Engineering
Supervisor: Gustav Grimstad
Co-supervisor: Aleksander Sæthereng Gundersen
June 2023

NTNU
Norwegian University of
Science and Technology

Adrian Weidemann Skagseth

In-situ characterization of Øysand sand with CPTU add-on tool Flow Cone and HPT

Master’s thesis in Civil and Environmental Engineering
Supervisor: Gustav Grimstad
Co-supervisor: Aleksander Sæthereng Gundersen
June 2023

Norwegian University of Science and Technology
Faculty of Engineering
Department of Civil and Environmental Engineering

Preface

This master thesis was written during the Spring semester of 2023 as part of the MSc in Civil and Environmental Engineering at the Geotechnical Division of the Department of Civil and Environmental Engineering at the Norwegian University of Science and Technology (NTNU). The duration of the study comprised 20 weeks.

The thesis was proposed by the Norwegian Geotechnical Institute (NGI), and has been carried out at field location near Trondheim, Norway and laboratory location in Oslo, Norway in collaboration with NGI.

Trondheim, 12-06-2023

Adrian W. Skagseth

Adrian Weidemann Skagseth

Acknowledgment

I would like to thank my supervisor at NGI, Aleksander Sæthereng Gundersen, for giving me the chance to learn more about field and laboratory testing, great support and brilliant feedback during the completion of this thesis.

Secondly I want to thank my NTNU supervisor Professor Gustav Grimstad for great lectures, supervision, feedback and discussion during my last year as a master student and during this thesis.

Thirdly I want to thank Santiago Quinteros and Taeheon Kim at NGI for providing frozen soil samples, help and support during laboratory study in Oslo.

Lastly I want to thank my family for support during these years

Abstract

Hydraulic conductivity plays a critical role in many aspects of geotechnical engineering, like uplift forces in a sheet pile building pit or suction bucket installations at the bottom of the sea. Also, during the process of consolidation, hydraulic conductivity is a fundamental parameter for analyzing the rate at which excess pore water dissipates from saturated soils. Therefore, the accurate determination of hydraulic conductivity is crucial for predicting settlement and getting accurate soil models in numerical calculations. However, the parameter is victim of large variations in numerical value and is tricky to determine in sand, silts or mixtures of these with finer grain material.

In this study, new methods and tools for in-situ measurements and calculations of hydraulic conductivity was employed at sandy, silty test site NGTS Øysand, just outside Trondheim, Norway. In addition, hydraulic triaxial tests were performed on a previous frozen sample from the same test site. The Flow Cone and Hydraulic Profiling Tool was tested at two different test locations at NGTS Øysand and compared to in-situ falling head tests, estimation of hydraulic conductivity by CPTU data and results from hydraulic triaxial tests.

A frozen 103 mm sample of mostly sandy silt with some clay content was trimmed, cored and cut with great caution to not reduce the temperature of the specimens. Two horizontal specimens and one vertical specimens was gathered from the 103 mm frozen sample. In addition, an older piston sampled sandy, clayey silt specimen was made available and tested in triaxial cell.

Field tests were performed by the author with help of crew and boring rig from NGI. In total, four standpipes were relative closely installed at different depths for in-situ falling head tests. Three HPT runs and one Flow Cone run was performed at various locations. Different methodologies were employed to interpret and calculate the hydraulic conductivity. In addition, a excess pore pressure dissipation methodology for estimation of horizontal coefficient of consolidation was trialled for the Flow Cone.

Big variation in results for the different employed methodologies for HPT is eminent, but one method shows good correlation with in-situ falling head tests. Unfortunately, only three of the depth internal Flow Cone tests were acceptable in terms of determining a value for hydraulic conductivity, but the results are promising, compared to CPTU estimations. Estimated coefficients of horizontal consolidation is presented for each internal depth test.

All hydraulic conductivity results were compared with other results from respective locations. By a process of comparison with results from the other tests, the methodology which gave the best fit was presented as hydraulic profile for its position. At last, evaluation of employed methodologies is presented.

Sammendrag

Hydraulisk konduktivitet spiller en kritisk rolle for mange problemstillinger innenfor geoteknisk prosjektering, slik som heving av grunnen i en byggegrop eller bøttefundament på havets dyp. I konsolideringsteori spiller hydraulisk konduktivitet nok en viktig rolle og er med på å bestemme de grunnleggende parameterne for setning og styrke. Hydraulisk konduktivitet bestemmer hvor for dissiperingen av ekstra poretrykk tar for et materiale som er utsatt for en ny last. Derfor er hydraulisk konduktivtet også en svært viktig parameter for nøyaktige numeriske beregninger. Desverre er hydraulisk konduktivitet også en av de geotekniske parameterene som viser størst variasjon i verdi. På grunn av kornskjelletet og oppførselen til sand, silt eller blandinger av disse med finere kornfraksjoner, er det vanskelig å bestemme in-situ hydraulisk konduktivitet.

I denne studien er nye metoder for in-situ målinger og kalkulasjoner av hydraulisk konduktivitet testet ved NGTS Øysand, som består hovedsaklig av sandig silt og noe leire ved enkelte dyp. I tillegg til feltforsøk er hydraulisk konduktivitet testet på gamle, frosne prøver i en treaksiale celle. Flow Cone og Hydraulic Profiling Tool ble testet ved to forskjellige lokasjoner på Øysand og sammenlignet med in-situ falling head prøver, estimering av hydraulisk konduktivitet ved hjelp av CPTU data og resultater fra treaksial forsøk.

Ved en rask prosedyre ble en frossen sylinder med størrelse 103 mm til tre prøveeksemplar ved trimming, kutting og kjerneborring. Dette resulterte i to horisontale prøver og 1 vertikal prøve. I tillegg ble en ikke-fryst prøve skjøvet ut og trimmet. Denne kom fra en annen lokasjon enn de frosne prøvene på Øysand.

Felttester ble gjennomført av forfatter med hjelp fra personell og borerigg fra NGI. Totalt ble 4 standrør installert ved forskjellige dybder for for in-situ falling head tester. Tre kjøringer med HPT og en kjøring med Flow Cone ble gjennomført ved to forskjellige lokasjoner. Forskjellige tolkningsmetoder ble benyttet til å beregne hydraulisk konduktivitet. I tillegg ble dissipasjon av økt poretrykk brukt til å estimere den horisontale konsolideringskoeffisienten ved hjelp av målinger fra Flow Cone.

De forskjellige tolkningsmetodene for HPT viser stor variasjon, men en metode sammenfaller godt med in-situ falling head tester. Desverre ble bare tre kjøringer av tester ved to forskjellige dybder brukbare fra Flow Cone forsøk. Likevell viser resultater fra Flow Cone bra potensiale, sammenlignet med estimeringer av hydraulisk konduktivitet fra CPTU data. Estimater for horisontale konsolideringskoeffisienter er presentert.

Alle resultater for hydraulisk konduktivitet er sammenlignet med hverandre fra sine respektive lokasjoner. Ved sammenligning ble det anbefalt hydrauliske profiler for testlokasjonene. Til slutt ble alle tolkningsmetodene evaluert.

Contents

List of Figures

List of Tables

List of Acronyms

CPTU Piezocone penetration testing.

FCHM1 Flow Cone hydraulic module version 1.

FCHM2 Flow Cone hydraulic module version 2.

FCPTU Flow Cone.

FGS1 Frozen ground sample 1.

GSDC Grain size distribution curve.

GWL Groundwater level.

HPT Hydraulic Profiling Tool.

NGI Norwegian Geotechnical Institute.

NGTS Norwegian Geo-Test Sites.

NGU Geological survey of Norway.

SBTI Soil Behaviour Type Index.

Chapter 1

Introduction

1.1 Background

NGI project SP14 GeoPerm was established in 2020 with the aim and purpose to improve the industry practice for characterisation of hydraulic conductivity in geomaterials. This thesis is a part of a underline project with focus on in-situ measurements of hydraulic conductivity in sand.

1.2 Objectives

The aim of this thesis is to test a prototype of the Flow Cone tool developed by Norwegian Geotechnical Institute (NGI) and the direct-push Hydraulic Profiling Tool (HPT) made by American company Geoprobe.

- Characterize the in-situ hydraulic conductivity for Øysand sand using CPTU add-on tool Flow Cone or direct-push Hydraulic Profiling Tool.
- Evaluate current and further develop interpretation methodology for hydraulic conductivity from FCPTU and HPT using in-situ testing.
- Perform hydraulic testing on frozen ground specimen in triaxial cell with aim to maintain in-situ fabric.

1.3 Approach

Firstly, a literature is carried out to gain knowledge about in-situ measurements of hydraulic conductivity and theory concerning hydraulic properties of soil. Then preparations were made for laboratory testing of frozen soil specimens. These were cut, trimmed and cored and installed in triaxial cell.

After triaxial testing, field excursion and boring plan was made in agreement with supervisor from NGI. After Easter, the field tests were performed.

Lastly the measured data from field tests are interpret.

Symbols are presented directly in the text of this thesis.

1.4 Structure of the Report

The chapters in this thesis is structured as follows:

Chapter 2 Gives a brief overview of relevant theory for understanding hydraulic conductivity and the laws governing it.

Chapter 3 Presents the employed equipment and tools used for field tests. An overview of methodologies for interpretation is also shown in this chapter.

Chapter 4 Gives a brief introduction to NGTS Øysand research site and the geotechnical characterization of the site.

Chapter 5 Presents procedures of each field test and laboratory test.

Chapter 6 Presents the measured and interpret results from field tests. Also conclusions following each field test is included for easier reading.

Chapter 7 Results, interpretations and conclusion of hydraulic triaxial and other laboratory tests are given in this chapter.

Chapter 8 Main comparison, evaluation and discussion of compiled results and used methodologies are presented in this chapter.

Chapter 9 Presents end conclusion and recommendations for further work.

Chapter 2

Theory

This chapter presents theory and background deemed relevant for in situ hydraulic properties of granular soils and related field investigations. Initially, the characteristics and properties most relevant for hydraulic conductivity of granular soils are presented. Then follows a description of the physical phenomenons of fluid transmit, here water, through a porous medium and how they are calculated using Darcy's law in granular soils. In this thesis, soils are considered in terms of a geotechnical engineering point of view. The term "top soil" corresponds to soil of agricultural purposes.

2.1 Properties of Granular Soils

As shown in Figure 2.1 soil sediments are a multiple phase system, containing water, grains, air and eventually organic material. The hydraulic parameters of granular soils are dependent on the relationship between these phases together with the index data, composition and properties of the soil (Janbu, 1989).

2.1.1 Classification and Characteristics of Granular Soils

Classification

Granular soil is used as a collective term for soil fractions like gravel and sand or a combination of these. It is defined as a collection of soil grains of various shapes, visible to the naked eye without magnification, with an amount of gravel and/or sand exceeding 50 % of the weight, according to (Mitchell and Soga, 2005). Granular soil can therefore also include fines, like soil fractions silt or clay. According to ISO 14688-1:2017, the grain size of granular soils can vary in range from fine sand at 0.063 mm to coarse gravel at 63 mm, not including grain size of fines content (Standards Norway, 2018a). The physical characteristics are dictated by the grain shape, size, surface texture and size distribution (Janbu, 1989).

The grain size distribution curve GSDC provides the distribution of grain sizes in a sieved sediment and is used to calculate the uniformity coefficient C_u, as seen in Equation (2.1), where d_{60} (mm) is the grain size at which 60 % of the total solid mass has lesser grain size. Same principle for d_{10}, only at 10 %. The uniformity coefficient together with a visual GSDC shows how uniform the sediment is, and reveals its compressibility (Janbu, 1989).

$$C_u = \frac{d_{60}}{d_{10}} \tag{2.1}$$

Behaviour

By definition, granular soils behaves cohesionless and anisotropic, but can display apparent cohesion when it consists of fine sand and silt particles with a moist, unsaturated pore water condition. Clay minerals can bestow granular soil some plastic characteristics, even at low percentage of total mass. Granular soils also possesses some capillary capabilities, from fine sand and other finer content. With concern of groundwater flow, they can behave either like an aquifer or aquitard, depending on the composition and characteristics of the granular soil (Janbu, 1989).

In solid state, granular soil exhibit solid-like behavior by its shear strength and complex elasto-plastic deformation. Granular soils can also behave like a liquid, i.e. it flows in a dense state due to liquefaction (Mitchell and Soga, 2005). This is apparent when reducing the effective stress to zero.

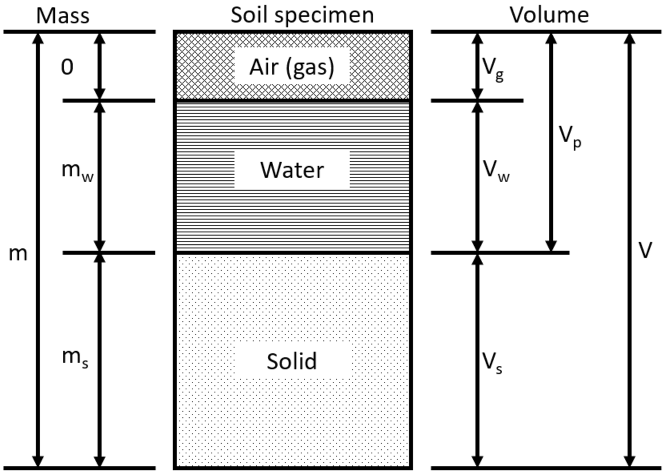

Figure 2.1: Three phase system of soil (adapted from Janbu, 1989).

Grain Shape

Grain shape is described in two scales; morphology and texture, where morphology compares the whole grain to known geometric shapes and texture describes the local features of the grain, such as surface, edges and corners of the grain (Mitchell and Soga, 2005). For granular soils, the grain shape is usually described by roundness and sphericity. The roundness of a grain depends on the angularity of local corners and edges, while sphericity compares the grain to a sphere and captures the deviation, as shown in Figure 2.2 (M. C. Powers, 1953).

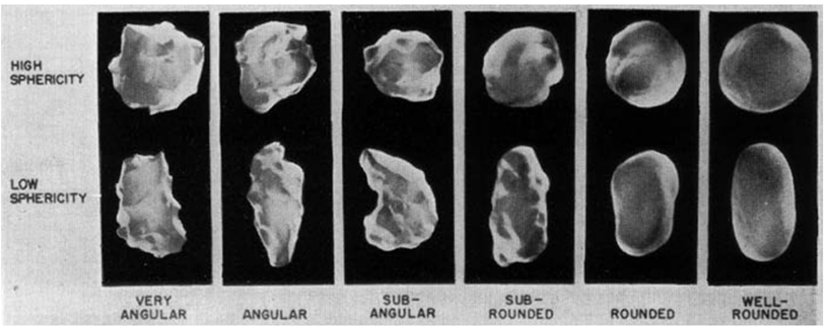

Figure 2.2: Roundness and sphericity of grains (from M. C. Powers, 1953).

Soil Fabric

Soil fabric relates to the spatial and geometrical arrangement of grains and pore space within the soil (Oda, 1977). The fabric shows how the soil matrix or skeleton is built up and are dependent on grain size distribution and the depositional environment. During sedimentation, the longest side of the grain usually aligns normal to gravity and parallel to the deposit floor, but this will vary with the grain shape. Grain associations can be divided between clay suspension aggregates and individual grain arrangement, where clay exhibit a more complex structure. Figure 2.3 displays typical fabric arrangements of granular soil with fines content (Mitchell and Soga, 2005). The orientation of individual grains or aggregates along with voids and cracks in the soil fabric, can make granular soil anisotropic.

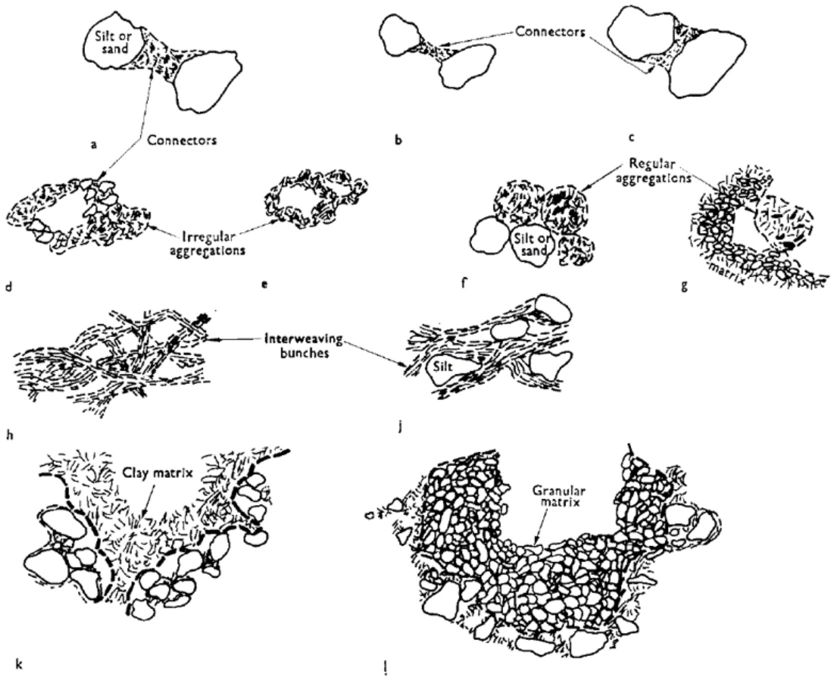

Figure 2.3: Soil fabric arrangements (from Collins and McGown, 1974).

Because sand and gravel are large and vary in roundness and sphericity, they act as independent units. Without fines, granular soil consists of grain-grain contact with relatively dense packing, because of irregular grain shapes. This can be compared to a ideal packing of uniform spheres, as seen in Figure 2.4a. The fines content will act as connectors and occupy pore space between the granular grains, as seen in Figure 2.3, and give smaller void ratio compared to the uniform sphere packing, i.e. the soil fabric becomes almost like a composite.

Soil fabric can be divided into three levels of scale; microfabric, minifabric and macrofabric, according to (Mitchell and Soga, 2005). These scales and the information they contain are important for mechanical and hydraulic properties of the soil. Microfabric details the regular aggregations of grains and the pore space between them on the smallest scale while minifabric gathers the microfabric aggregations and displays how they are connected with possible internal pore pathways. Macrofabric displays the smaller scales and may contain fissures that separates large aggregations, i.e. voids. Figure 2.4b displays the macrofabric of granular soil with fines content and displays clusters of minifabric.

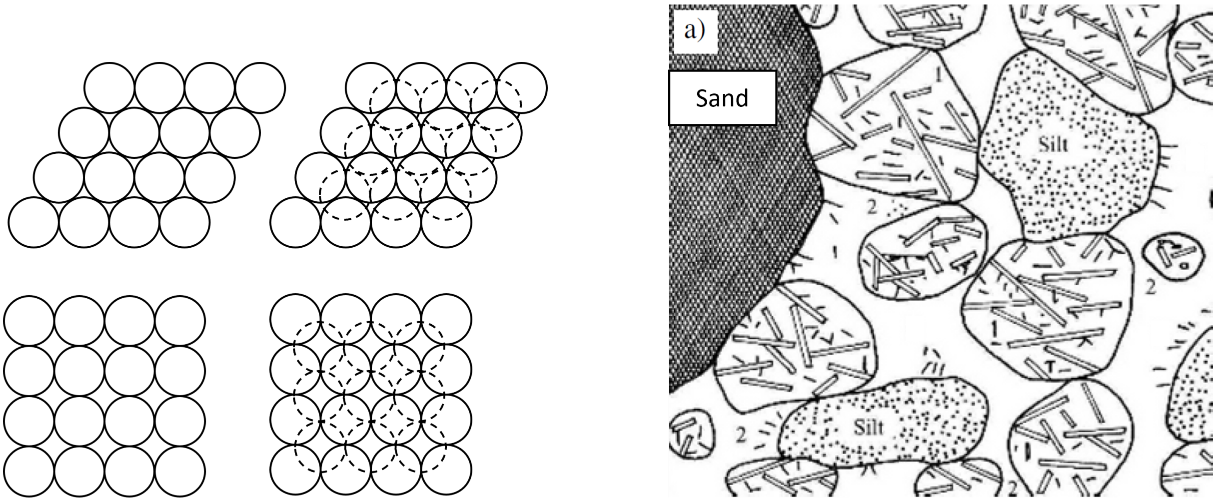

(a) Uniform sphere ideal packings (adapted from Mitchell and Soga, 2005).

(b) Macrofabric of granular soil (modified from Zeh and Witt, 2007).

Figure 2.4: Packing, 2.4a, and fabric of soil, 2.4b where 1: Clusters of aggregates (minifabric), 2: Fissures, transassemblage pores (macrofabric).

2.1.2 Index Properties

Index properties describes the distribution between soil, water and air in Figure 2.1 and depicts the fundamental composition for mechanical and hydraulic parameters.

Volumetric Relationships

Void ratio is the relationship between volume of pores, V_p, and volume of solids, V_s, as seen in Equation (2.2), in percent. Void ratio is often combined with porosity, Equation (2.3) where V is the total volume of the tested soil (Janbu, 1989).

$$e = \frac{V_p}{V_s} \tag{2.2}$$

$$n = \frac{V_p}{V} = \frac{e}{1+e} \tag{2.3}$$

For granular soil, the void ratio can describe how densely packed the soil is, based on maximum and minimum void ratio, see Equation (2.4). e_{max} and e_{min} is the void ratios of the soil in its densest and loosest compactness state. High relative density in granular soils relates to a more compact soil, which alters the hydraulic parameters and mechanical properties (Janbu, 1989).

$$D_r = \frac{e_{max} - e}{e_{max} - e_{min}} \tag{2.4}$$

The relationship between volume of water, V_w, and volume of pores, V_p, gives the degree of saturation in Equation (2.5). In situ soil below the groundwater table is considered to more or less fully saturated, while Figure 2.1 depicts an unsaturated soil (Janbu, 1989). The degree of saturation alters both the hydraulic parameters and the strength of the soil, due to soil suction ψ in unsaturated soils (Fredlund et al., 1994).

$$S_r = \frac{V_w}{V_p} \tag{2.5}$$

2.2 Flow in Granular Soils

Groundwater flow can be divided into two states; steady-state and transient flow. Steady-state refers to a flow where hydraulic head and flow rate, i.e. the flow variables, do not change with time, while in transient (unsteady) state the flow variables can vary in time or be independent of time (Delleur, 2006).

2.2.1 Hydraulic Head, Hydraulic Gradient and Velocity

Hydraulic Head

Water flows through soil because of difference in hydraulic head, i.e. the mechanical energy available in water. Water will flow from higher hydraulic head to lower hydraulic head. From Bernoulli's principle, the hydraulic head h in Equation (2.6) consists of pressure head noted $\frac{P_w}{\gamma_w}$ and elevation head y from a set datum, while velocity head is neglected because of relative low flow rates in typical geotechnical conditions. A flow rate of 0.01 m/s is considered a high flow rate, which yields a negligible velocity head (Janbu, 1989).

$$h = \frac{P_w}{\gamma_w} + y \tag{2.6}$$

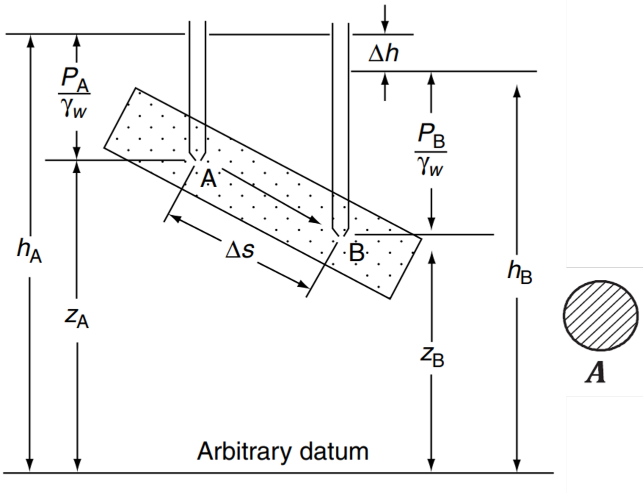

Figure 2.5: Hydraulic head and gradient (adapted from Delleur, 2006).

Hydraulic Gradient

Hydraulic gradient is the change in hydraulic head dh over the distance dl in the flow direction, as seen in Equation (2.7). Figure 2.5 shows water flowing from point A to point B, driven by a loss in hydraulic head over a distance $\Delta s = dl$ (Delleur, 2006).

$$i = -\frac{dh}{dl} \tag{2.7}$$

Velocity

The discharge velocity v in Equation (2.8) is the amount of water Q that flows through a specimen with area A, over a constant length, driven by the difference in hydraulic head over a time period.

$$v = \frac{Q}{At} \tag{2.8}$$

2.2.2 Darcy's Law and Reynolds Number

Darcy's Law

Darcy's law states a proportionality between the discharge velocity and the hydraulic gradient in a saturated porous medium, as seen in Equation (2.9) and Figure 2.6 for one-dimensional flow in x-direction. Darcy's law is fundamental for both steady-state and transient flow problems, but the proportionality in Equation (2.9) is only valid for linear steady and laminar single-phase flow, with isothermal condition and constant fluid viscosity (Mitchell and Soga, 2005). The proportionality factor K in Equation (2.9) and Equation (2.10) is called hydraulic conductivity (Delleur, 2006).

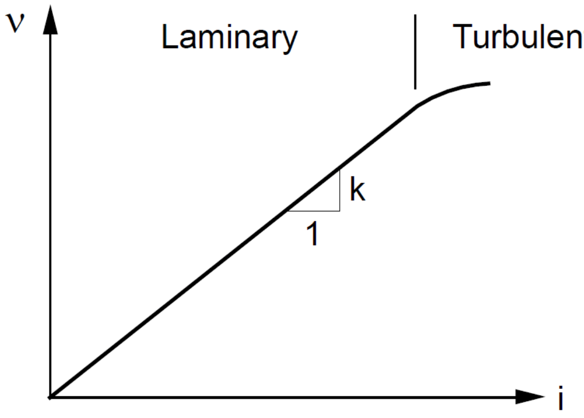

Figure 2.6: Relationship between flow rate and hydraulic gradient in porous medium (from Sandven et al., 2017).

$$v = Ki = K\frac{dh}{dx} \tag{2.9}$$

In Equation (2.10) q is the flow rate through a cross-section A, which considers flow through the whole cross-section area, based on Darcy's law. The true laminar flow through the cross-section takes place in the pores and is called *seepage velocity* (Delleur, 2006). It is given by the discharge velocity and porosity of the tested medium in Equation (2.11). Since porosity in Equation (2.3) can't be larger than unity and is theoretically between 26-48 % for the idealized sphere packed fabric of Figure 2.4a representing granular soil, the seepage velocity will always be faster than the average velocity from Darcy's law (Delleur, 2006).

$$q = KiA \tag{2.10}$$

$$v_s = \frac{v}{n} \tag{2.11}$$

Reynolds Number

Reynolds number Re describes the flow behaviour, laminar or turbulent, in a fluid by the ratio between inertial and viscous forces within the fluid. For steady-state water flow in a saturated porous medium, Re can be used to predict the transition between laminar (Darcy) and turbulent (Post-Darcy) flow, as seen in Figure 2.6. In Equation (2.12) Re is modified to account for average diameter of grains

d, while ρ is the density of the fluid, μ is the dynamic viscosity of the fluid and v is the discharge velocity (Delleur, 2006).

$$Re = \frac{vd\rho}{\mu} \tag{2.12}$$

Deviations in Darcy's Law

As seen in Figure 2.6, the relationship between the flow rate and the hydraulic gradient can not always considered to be linear. When considering groundwater, the relationship mostly depends on the flow rate and the grain and pore sizes of the medium.

With large grain and pore sizes and high flow rate, the flow can become turbulent. According to Khalifa et al. (2002) the critical value of Reynolds number for transition between laminar and turbulent flow in saturated soils, is in the range of 1 to 10. By assuming Reynolds number equal to 1 and using Equation (2.12) with a conservative velocity of 0.0025 m/s and fluid properties of water, Delleur (2006) found that average grain size d equal to 0.4 mm or less is necessary for laminar flow, i.e. Darcy's law is valid, when considering a uniform collection of grains. This is in line with Janbu (1989) which states that Darcy's law can be applied for saturated flow in coarse sand and finer fractions. Turbulent flow is therefore typical for flow through uniform gravel and coarser material.

For lower values of flow rate and hydraulic gradient in porous mediums, the deviation from linear Darcy flow is not yet fully discovered (Dejam et al., 2017). According to (Mitchell and Soga (2005); Janbu (1989)), this deviation is most apparent in clays, where the pore spaces becomes very small.

2.3 Hydraulic Parameters

In geotechnical engineering, the most important hydraulic parameters of granular soils are hydraulic conductivity, infiltration rate and water retention characteristics. These parameters determines the groundwater flow and seepage, which is vital for deformation, volume change and stability behavior in geotechnical design cases. In this thesis, the focus will be on the first mentioned parameter hydraulic conductivity.

2.3.1 Permeability

Pores within a granular soil fabric are interconnected and form pathways for fluid transmit. These pathways are dependent on fabric, grain shape and the relative density of the soil, in which the surface of the grains offer resistance to the fluid and the fabric and density determines the size and regularity of the pathways (Janbu, 1989).

Permeability describes the ease with which a porous medium, like granular soil, will transmit a fluid through its pore spaces, i.e. the pathways (Delleur, 2006). *Intrinsic permeability, k* is permeability that is a function of average pore size d of the medium and other medium properties C that affect flow, like grain shape, volume of pores and grain size distribution, as shown in Equation (2.13). Intrinsic permeability does not include fluid properties, temperature or pressure (Delleur, 2006).

$$k = Cd^2 \tag{2.13}$$

2.3.2 Hydraulic Conductivity

Hydraulic conductivity, K gives a complete description of the ease a specific fluid will flow through a porous medium. It combines the properties of the fluid and the medium, through intrinsic permeability. In Equation (2.14) k represents the intrinsic permeability while ρ is the fluid density, g

is the gravitational acceleration and μ is the dynamic viscosity of the fluid. For this thesis hydraulic conductivity has unit m/s (Delleur, 2006).

$$K = \frac{gk}{\eta} = \frac{k\rho g}{\mu} \tag{2.14}$$

Variations in Hydraulic Conductivity

With water as specific fluid, through dynamic viscosity μ the hydraulic conductivity is dependent on the temperature of the water. In situ temperature of groundwater does not vary much, but for hydraulic conductivity's determined by laboratory tests, usually at 20 °C, corrections must be made for comparison with in situ hydraulic conductivity. As the factor $\frac{g}{\eta} = \frac{\rho g}{\mu}$ in Equation (2.14) does not vary much in situ, the intrinsic permeability is the key factor for hydraulic conductivity of granular soils (Janbu, 1989).

Hydraulic conductivity is dependent on the phase condition of the granular soil sediment, i.e. how saturated the soil sediment is and its grain size distribution and soil matrix, through intrinsic permeability.

Chapter 3

In-situ Measurements of Hydraulic Conductivity

This chapter provides an overview of employed tools and equipment for measurement and determination of in-situ hydraulic conductivity. A brief approach for other associated properties and parameters that aid in assessing the hydraulic conductivity, like soil classification based on CPTU results, is also presented. Secondly, the theoretical approach for calculation of in-situ hydraulic conductivity for the various tools is presented along with some previous work from literature.

3.1 Flow Cone System

The Flow Cone is a prototype tool developed by NGI for in-situ measurements of hydraulic properties. It is best described as a two-part system, where a hydraulic module is below ground level and a control module is above ground level, as seen in Figure 3.1. The hydraulic module is paired with a standard piezocone penetrometer (CPTU) and consists of a bronze filter, placed above the CPTU cone, with a hydraulic tube and pressure sensor inside. Water flows out from the hydraulic tube and the bronze filter into the surrounding soil (A. S. Gundersen et al., 2019). The control module can be divided into three parts:

Part I: A linear step motor driving a piston upwards and downwards in a cylinder containing water.

Part II: Data acquisition system for sampling pressure sensors and flow rate. This system has a connection for software control program which handles valves and step motor and presents sampled measurements live.

Part III: A top head containing ambient pressure and system pressure sensors as well as valves and tubing for connection to the hydraulic module and water container.

The first version, hereby named FCHM1, of the hydraulic module is made with a modified 1 inch standard water pipe with connection for CPTU probe at the end. The outside diameter of the bronze filter, 3.68 cm, is almost the same as the CPTU probe, as seen in Figure 5.3a. The length of the filter is 11.95 cm. This probe does not feature a pressure sensor at filter position and uses 1 inch standard water pipe rods while advancing down into the subsurface. An updated version, hereby named FCHM2, of the hydraulic module was prepared for field tests at Halden in 2022 (A. Gundersen et al., 2022), enabling connection of the hydraulic module to 36 mm CPT rods that are stronger and more suitable for advancing through virgin soil than 1 inch standard water pipes.

Unfortunately, the pressure sensor in the hydraulic module, i.e. u_f in the middle of the flow filter in Figure 3.1, broke right before departure to test site. Therefore, the pressure in the hydraulic module is only measured with the system sensor in the control module, marked "dP" in Figure 3.1. This demands a correction to the pore pressure $u_{f,m}$ for system flow resistance to obtain the corrected pore pressure u_f.

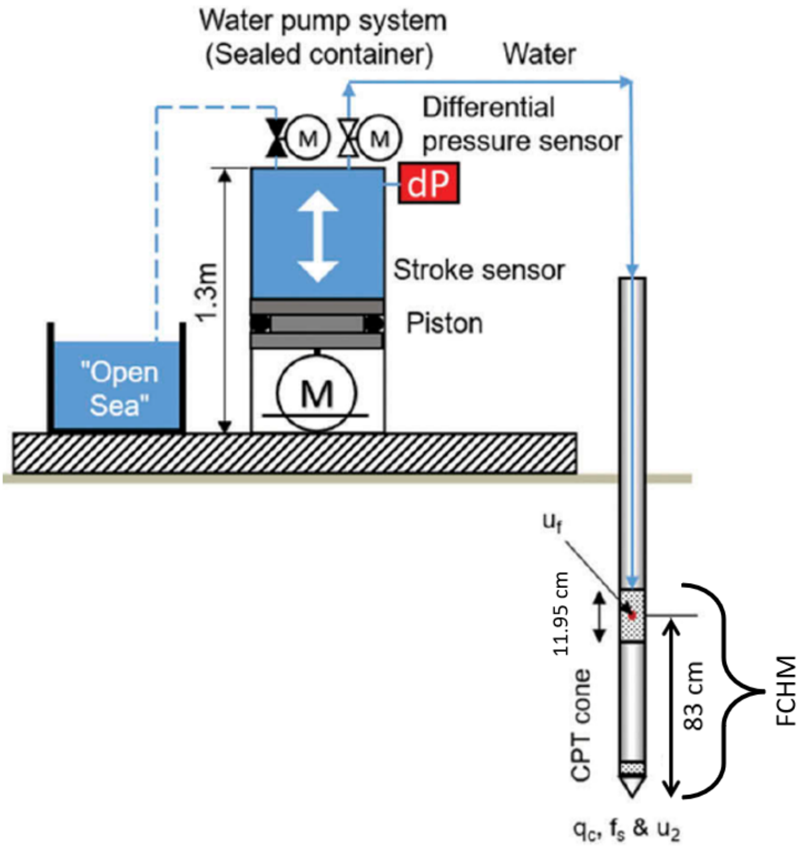

Figure 3.1: Flow Cone system and setup in field (adapted from A. Gundersen et al., 2022).

Flow Cone measures temperature and pressure in both ambient and system sensors, which is logged every 755 millisecond. The software control program is also developed by NGI, made with LabVIEW, and logs data to text files. The subsurface position and advancing speed of the Flow Cone filter is known with data from CPTU and the boring rig. Flow Cone testing is divided into two phases, where stationary phase is used to estimate the in-situ hydraulic conductivity in this thesis:

Penetration phase: During penetration phase the hydraulic module advances down with standard CPTU speed, i.e. 2 cm/s, with a chosen water flow from the bronze filter. The constant water flow reduces clogging of the filter and keeps the system saturated.

Stationary phase: During stationary phase, either falling head tests (dissipation) or constant flow rate test can be performed, as visualized in Figure 3.2, at desired locations subsurface.

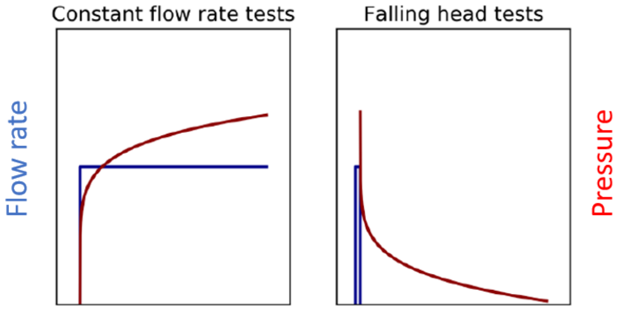

Figure 3.2: Flow Cone stationary test types (adapted from A. S. Gundersen et al., 2019).

3.2 Hydraulic Profiling Tool

The Hydraulic Profiling Tool (HPT) is a logging system developed by American company Geoprobe Systems® for measurement of hydraulic properties in saturated zones and electric conductivity while advancing a probe down into the subsurface. The HPT system works similar to Flow Cone, but injects water into the soil matrix from a single outlet port, rather than from a cylindrical filter and also measures soil resistivity with a Wenner array. The system can be combined with different logging probes, dependent on the survey, but is for this thesis combined with the basic HPT probe by Geoprobe Direct Image®, as seen in Figure 3.3 (Wes McCall, 2013).

The HPT system can be divided into two categories, with letter reference to Figure 3.3:

Surface instrumentation: Water tank (A), data acquisition module FI6000 (C) and HPT flow pump module K6300 (B) connected to a computer with acquisition and control software. Also testing equipment for reference tests of probe sensors before and after log and a string pot for depth reference on the drilling rig.

Subsurface instrumentation: The K6052 HPT probe with pressure sensor (E), injection port (F) 10 mm diameter and 406 mm above the probe tip and electrical conductivity Wenner array (G), which is average 200 mm above the probe tip.

The K6052 HPT probe has outside diameter 44.45 mm and is connected with a modified rod adapter, that was made by NGI, to connect the HPT probe to standard 36 mm CPT rods. In this setup, HPT measures subsurface location, penetration speed, electrical conductivity, water outflow, line pressure and injection pressure (HPT pressure) with time. The operating software, named DI Acquisition, shows live results and is used for post-run interpretation of data. The HPT testing is divided in two phases, as for Flow Cone, but uses the measured data combined from both phases to estimate the hydraulic conductivity:

Penetration phase: The HPT probe advances down the subsurface at CPTU speed, i.e. 2 cm/s, while the pump (B) and pressure sensor (E) works together to maintain a constant set rate of water flow out from the injection port (F). The Wenner array measures electric conductivity while the probe is advancing.

Stationary phase: During the stationary phase, the pump (B) is switched off and a dissipation test is performed, where the HPT pressure from sensor (E) is allowed to dissipate towards hydrostatic pressure (Wes McCall, 2013).

Afterwards, official software DI Viewer is used for post-run data processing or data export.

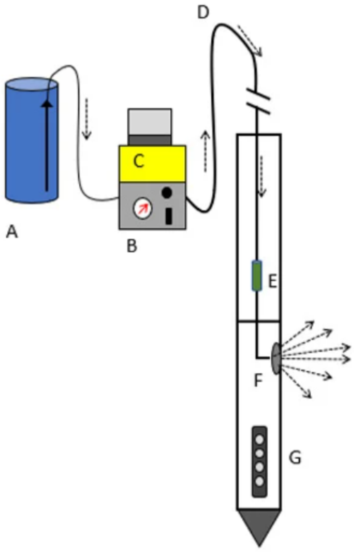

Figure 3.3: HPT system used at Øysand (adapted from Wes McCall, 2013).

3.3 Falling Head Tests

There exists many setups to perform in-situ falling head tests in porous probes, as shown in (Hvorslev, 1951). For this thesis, the setup consisted of equipment presented in Figure 3.4. The falling head tests is performed in open 1 inch (internal diameter, 2.54 cm) standard water pipes with a bronze filter from Swedish company Geotech at the end and with water level logger from Canadian company Solinst® inside the water pipes. Above the surface an atmospheric logger from the same company is mounted in an old open water pipe at the test area. The loggers measure water level and atmospheric pressure with temperature and time and are programmed and read with software from Solinst.

The bronze filter is 27 cm long with an outside diameter of 3.22 cm with connections for standard 1 inch water pipes and pore size 50 μm. The logger used down-hole is the Solinst Levelogger 5 LT M100 and the logger used for atmospheric pressure is Solinst Barologger 5 LT M1.5.

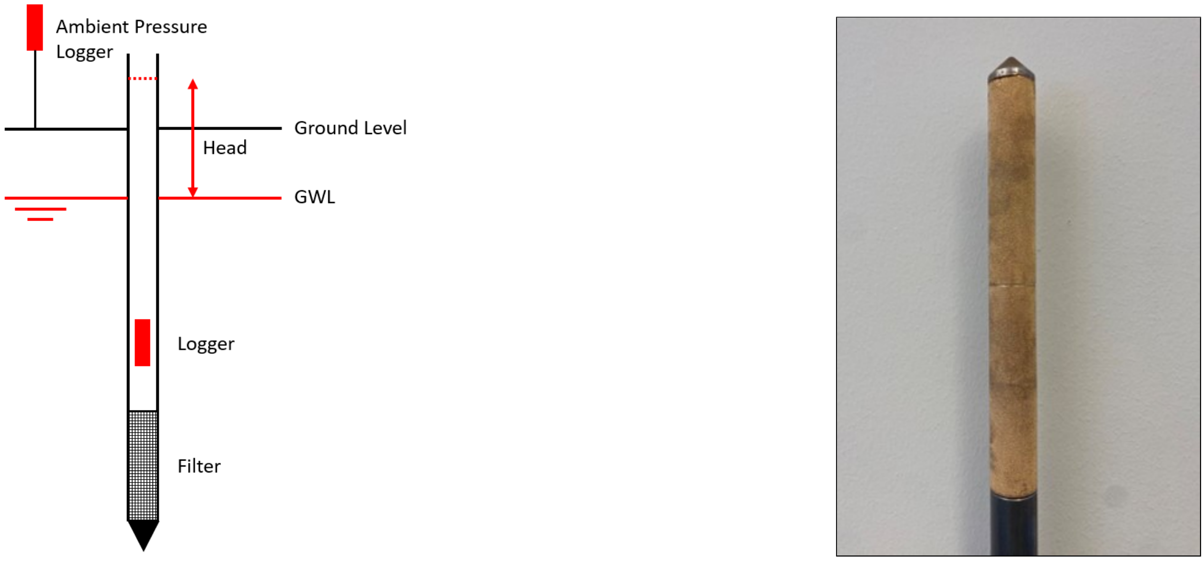

(a) Falling head test setup.

(b) Bronze filter from Geotech.

Figure 3.4: Falling head test setup and filter.

3.4 CPTU

As a part of the Flow Cone system, a Geotech Nova CPTU 10 cm^2 probe is used to support the Flow Cone procedure of determining the hydraulic properties of the tested soil. CPTU measures cone resistance q_c, side friction f_s and pore pressure u_2 behind the tip of the cone, as seen in Figure 3.1, with time and depth while advancing down the subsurface.

3.5 Falling Head Interpretation

In-situ falling head test interpretation provides the local hydraulic conductivity of either an aquifer or an aquitard from well established equations and procedures (Chapuis, R.P, 1998). By assuming Darcy's law is valid and negligible effects from the soil matrix deformation, i.e. saturated and over-consolidated material, the mass balance equation set the foundation of interpretation of hydraulic conductivity (Chapuis, R.P, 1998). Equation (3.1) simply puts that the flow rate injected into the soil is the same as the flow rate out of the soil, where c is the shape factor and H is the applied hydraulic pressure head.

$$Q_{inj} = Q_{soil} = cKH \tag{3.1}$$

The flow rate of the initiated pressure head is dependent on the area S_{inj} of the injection pipe, see Figure 3.4, and the velocity of the falling head.

$$Q_{inj} = -S_{inj}(\frac{dH}{dt}) \tag{3.2}$$

Combining Equation (3.1) and Equation (3.2) yields Equation (3.3), the velocity graph method (Chapuis, R.P, 1998). By using the velocity graph, the piezometric level within the injection pipe can be found by interpretation of the intercept of the mean head, dH/H, and the hydraulic conductivity can be calculated using the slope of a linear, best fit line of the plotted data (Chapuis, R.P, 1998).

$$\frac{dH}{H} = -(\frac{Kc}{S_{inj}})dt \tag{3.3}$$

By integrating Equation (3.3), the classic solution presented by (Hvorslev, 1951) is reached in Equation (3.4). Head pressure gets corrected by the piezometric level from the velocity graph, resulting in $H_r = H(t) - H_0$. By plotting this in a semi-log plot, $LN(H_r)$ versus time, the slope of the linear regression line can be used to determine the hydraulic conductivity.

$$\frac{H_1}{H_2} = -\frac{Kc}{S_{inj}}(t_1 - t_2) \tag{3.4}$$

3.5.1 Shape Factor

Shape factor represents the geometry of the outlet part from where the flow of the initiated head comes and takes boundary conditions and the anisotropy of the soil into consideration (Ratnam et al., 2001). A flow pattern can be approximated by the shape of the outlet, i.e. axisymmetrical flow net from the axisymmetrical filter in Figure 3.4. Based on proposed shape factors by (Hvorslev, 1951), a FEM simulation was performed by (Ratnam et al., 2001) for the two most used filter geometries for optimization based on the ratio of dimensions. For the filter presented in Figure 3.4, (Ratnam et al., 2001) proposed the shape factor in Equation (3.5), where $F = c$, L is the length and d is the outside diameter of the filter.

$$\frac{F}{d} = 0.5691\,(\frac{L}{d}) + 5.2428\,(\frac{L}{d})^{0.5} \tag{3.5}$$

3.5.2 Big Data Approach

With the use of the digital pressure transducers loggers, i.e. levelogger, presented in Section 3.3, comes both accuracy and inaccuracy, determined by the sampling rate of the data logger. Due to the nature of an in-situ falling head test, there might be uncertainties in the data connected to the initiation of the head, leakage, clogging of the filter, air or gas in soil or that time lag because of stress adjustment, i.e. change in volume and void ratio decreasing or increasing the rate of flow (Chapuis, R.P, 1998; Chapuis, 2012 and Hvorslev, 1951).

A simple procedure for correction of large data sets was proposed by (Chapuis et al., 2009). This involves assessing the uncertainty, slicing initial data at small values of t and chose a selecting condition by modified Equation (3.6).

$$\frac{\Delta V_{j,j+1}}{V_{j,j+1}} = \frac{\Delta H_{j+1} + \Delta H_j}{|H_{j+1} - H_j|} \tag{3.6}$$

3.6 Flow Cone Interpretation

3.6.1 Constant Flow Rate

By assuming laminar flow conditions during constant flow rate and that the pressure head has stabilized, the hydraulic conductivity can calculated using Equation (3.7) assuming the soil is incompressible and Darcy's law is valid (Hvorslev, 1951). This relationship can also be used when assessing multiple tests, as the slope of a linear trendline will be equal to hydraulic conductivity K.

$$K = \frac{Q}{Fh} \tag{3.7}$$

The pressure h in Equation (3.7) is the difference from corrected measured pore pressure u_f and the determined in-situ pore pressure u_0.

3.6.2 Dissipation of Excess Pore Pressure

The dissipation of excess pore pressure during a penetration stop of the CPTU probe advancement, can be used to estimate the in-situ horizontal coefficient of consolidation and hydraulic conductivity (Sully et al., 1999; P. K. Robertson et al., 1992). A strain-path method to interpret this dissipation in clay is suggested by (Teh and Houlsby, 1991). During the cone penetration in deep depths, the displaced soil is accommodated by plastic and elastic deformation zones, i.e. cavity expansion, where the extent of plastic deformation zone simplified is related to the rigidity index $I_r = G/s_u$, as seen in Figure 3.5a in radial space (Teh and Houlsby, 1991). By use of the strain-path method, Teh and Houlsby, 1991 included the history of soil strain due to cone penetration to distinguish between the plastic and elastic zones due to the different geometries of the cone.

From a simplified analysis based on Terzaghi-Rendulic uncoupled consolidation theory, i.e no change in total stress and strains by change in pore pressure and effective stress, and strain-path approach with initial pore pressure distribution based on I_r, Teh and Houlsby, 1991 computed the pore pressure distribution at different stages of dissipation Figure 3.5b with time factor $T = c_h t/a^2$ in 2-D radial consolidation.

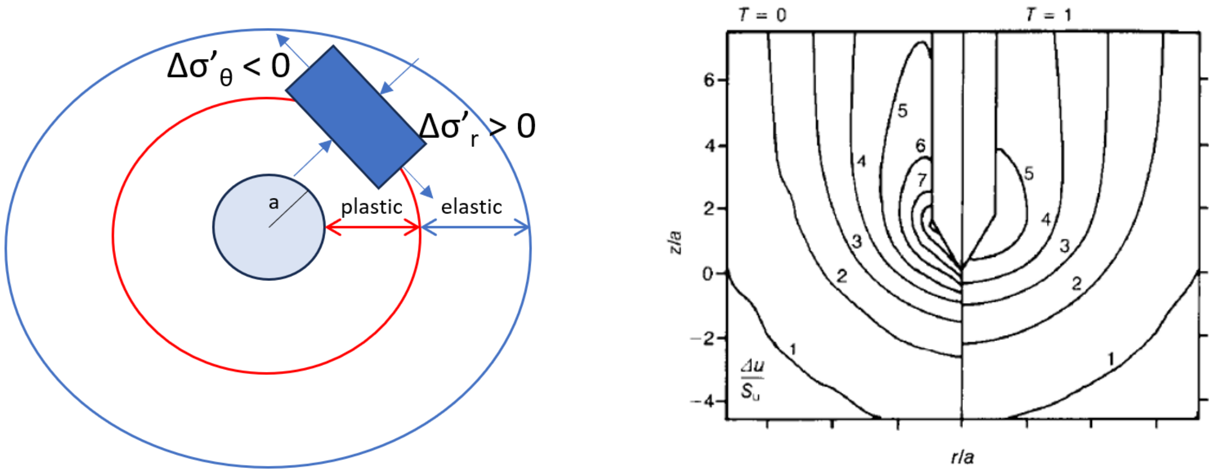

(a) Plastic and elastic deformation zones around CPTU probe.

(b) Pore pressure distribution at different stages of dissipation (from Teh and Houlsby, 1991).

Figure 3.5: Soil cavity expansion theory.

It is important to establish that this radial change in pore water pressure Δu will decrease in an ever growing radius r from the CPTU probe or Flow Cone filter. The initial swelling in the plastic zone surrounding the filter is trialled by an compression in the elastic zone in Figure 3.5a.

From strain-path method, dissipation of excess pore pressure is dependent on its position. As shown in Figure 3.5b, pore pressure along the shaft begins its dissipation a small amount of time after the dissipation of the pore pressure at the tip. Pore pressure along the shaft is also initially influenced by redistribution of high pore pressure from the tip region, increasing slightly before start dissipation (Teh and Houlsby, 1991). A modified time factor T^* accounts for the I_r dependent excess pore pressure, resulting in Equation (3.10), and based on results from dissipation curves using various values of I_r, position-dependent values of time factor T^* is suggested by (Teh and Houlsby, 1991).

Flow Cone injects a constant rate of water radially into the surrounding soil, to achieve a constant pressure head. As the flow is stopped, the radial surrounding soil will dissipate this excess pore pressure. By assuming that this excess pore pressure has induced plastic and elastic deformation on the soil, as for the CPTU, the dissipation is interpret with time factor T^* furthest away from the CPTU cone shoulder and normalized excess pore pressure U. Values of T^* 10 radii above cone shoulder is shown in Table 3.1.

Table 3.1: Modified time factor T^* from (Teh and Houlsby, 1991).

Degree of consolidation [%]	Modified T* at 10 radii above cone shoulder [-]
80	0.378
70	0.662
60	0.995
50	1.46
40	2.14
30	3.24
20	5.24

After stop flow rate, the corrected measured pore pressure u_f starts to dissipate. By using $u_f = u(t)$, the normalized excess pore pressure is established using Equation (3.8) from (Sully et al., 1999).

$$U = \frac{u(t) - u_0}{u_i - u_0} \tag{3.8}$$

From (Teh and Houlsby, 1991; Martínez et al., 2017; P. K. Robertson et al., 1992), Equation (3.9) is used to estimate the in-situ horizontal coefficient of consolidation, using T_{50} equal to T^* from Table 3.1, as time factor for 50% consolidation is most common (Martínez et al., 2017).

$$c_h = \frac{T_{50}\sqrt{I_r}a^2}{t_{50}} \tag{3.9}$$

The modified time factor suggested by (Teh and Houlsby, 1991) is presented in Equation (3.10).

$$T* = \frac{c_h t(U)}{a^2\sqrt{I_r}} \tag{3.10}$$

By combining Equation (3.9) and Equation (3.10), the time factor values T^* is calculated using Equation (3.11) by choosing the time t_{50} corresponding to 50% consolidation from plots of the excess pore pressure U against time t. When calculating T^*, the need for rigidity index I_r and cavity area a^2, which is the radius of the Flow Cone filter, disappears. This is because t_{50} is dependent on the the previous mentioned parameters and the estimated consolidation coefficient c_h.

$$T* = \frac{\frac{T_{50}\sqrt{I_r}a^2}{t_{50}} t(U)}{\sqrt{I_r}a^2} = \frac{T_{50} t(U)}{t_{50}} \tag{3.11}$$

3.7 HPT Interpretation

Hydraulic conductivity is post-estimated during the penetration phase along with measurements done both in the stationary phase and the pre- and post log run quality controls. From the penetration phase, the HPT pressure, penetration speed and water outflow is used along with dissipated ambient piezometric pressure from stationary phase and the atmospheric pressure from pre- and post log run quality controls. These parameters are used to calculate relationships which are compared with models to determine the hydraulic conductivity. The included models used in this thesis is briefly presented in the following sections.

3.7.1 Corrected HPT Pressure

Equal for all models is use of the corrected HPT pressure P_c, as seen in Figure 3.6. The piezometric pressure P_{piezo} is determined by dissipation test, i.e. the stationary phase of a HPT run, while the total HPT pressure P_{tot} is measured in the penetration phase. By assuming that the excess pressure due to probe advancement down the soil layers has dissipated by the time the HPT pressure is measured in the injection port distance 406 mm above the probe tip, P_c is calculated using Equation (3.12) (Wesley McCall and Christy, 2020). In Figure 3.6 the red squares mark performed dissipation test linked together with an assumed hydrostatic pressure increment. The red triangles mark zero datum (top of borehole) and back-calculated static water level, i.e. HPT assumed GWL.

$$P_c = P_{Tot} - (P_{atm} + P_{piezo}) \tag{3.12}$$

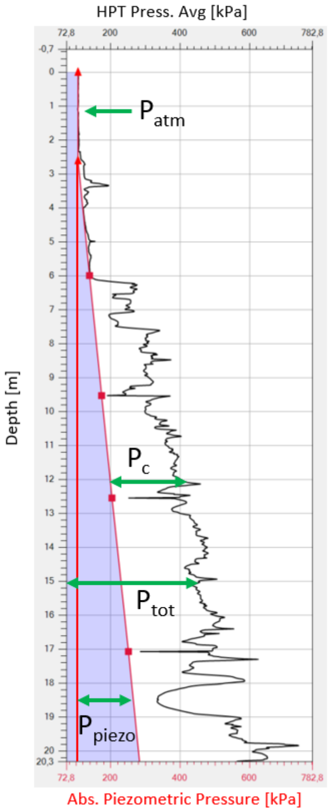

Figure 3.6: HPT pressure explanation. Made from screenshot of DI Viewer with HPT run at OYSC67.

3.7.2 HPT MC Approach

As of the date of this thesis, the suggested empirical model made by (Wesley McCall and Christy, 2020), see Figure 3.7 and hereby named "HPT MC", is the only model directly included in the DI Viewer software to estimate hydraulic conductivity. Based on results from performed co-located HPT logs and separate interval slug tests at various locations in North America, a best fit logarithmic equation with average HPT flow rate Q and corrected average HPT pressure P^* was proposed, as shown in Equation (3.13), where estimated K is in unit ft/day, flow rate Q in unit ml/min and P^* in unit psi (Wesley McCall and Christy, 2020).

The theoretical approach estimates Darcy's law and that the hydraulic conductivity is a function of the flow rate divided by the pressure (Wesley McCall and Christy, 2020). The model limits is approximately 3.53E-04 and 3.0E-07 for hydraulic conductivity K in unit m/s.

$$Est.K = 21.14 \cdot LN(\frac{Q_{inj}}{P*}) - 41.71 \tag{3.13}$$

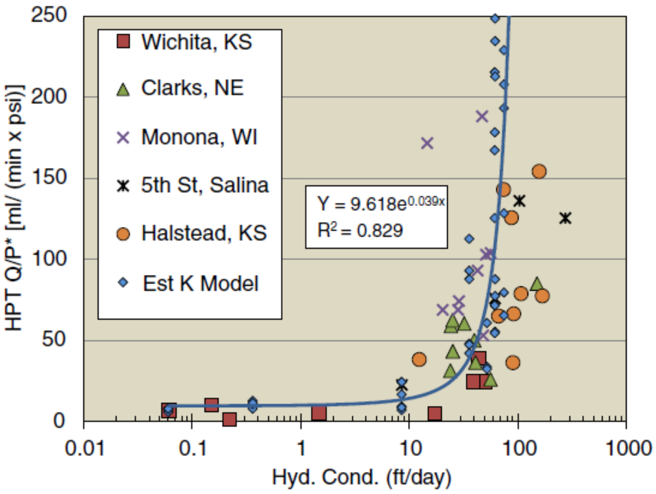

Figure 3.7: Suggested empirical model for estimation of hydraulic conductivity using HPT (from Wesley McCall and Christy, 2020).

3.7.3 HPT BO Approach

Based on a prior numerical model by (Liu et al., 2012) on a different, but similar direct-push injection probe, which considered the potential impacts of the disturbed zone created by the advancing probe tip, (Borden et al., 2021) proposed an alternative numerical model with an empirically derived efficiency factor E to accommodate for loss in hydraulic conductivity in the disturbed soil zone around the HPT probe (Borden et al., 2021). This model, Equation (3.14), takes HPT parameters such as penetration speed V and probe diameter D into consideration when considering the disturbed, remoulded soil zone, where porosity is lowered and hydraulic conductivity is altered. Equation (3.14) gives hydraulic conductivity in unit ft/day, as pressure P_c is in unit psi. A value of $E = 1.0$ is used for assumed uniform isotropic soil, i.e. no empirical correction for penetration generated excess pore pressure and disturbance. (Borden et al., 2021) used benchmark slug tests to fit the efficiency factor for better fit of K compared to the slug tests results.

$$Est.K = E(0.1235VD^2 + 0.119Q)P_c^{-1.017} \tag{3.14}$$

3.7.4 HPT ZH Approach

(Zhao and Illman, 2022) performed an inverse numerical simulation of HPT profiling on a specific test site, to better estimate the local variability in hydraulic conductivity. The groundwater flow simulation conceptualized HPT tests as water injection tests advancing down a 3D model. The advancement down in the simulation was linked with the actual performed HPT runs. A model independent parameter was coupled to the groundwater flow model and calibrated to minimize an objective function equal to the squared residual between observed and simulated head pressure changes Δp. Values for hydraulic conductivity was determined through iterative estimations (Zhao and Illman, 2022). The estimated hydraulic conductivity was used to generate a simple linear empirical model for the specific test site, with the relationship of flow rate Q and corrected pressure P_c as seen in Equation (3.15). This model is tuned to the specific site, NCRS Waterloo in Canada, which consisted of mostly silt and sand, with layers of silty clay and sandy silt.

$$LogK = 1.41Log(\frac{Q}{P_c}) + 4.25 \tag{3.15}$$

3.8 CPTU Interpretation

In addition to soil properties and groundwater setting, the three base parameters measured by the CPTU probe can be derived for interpretation of soil behaviour and thus be used to approximate hydraulic conductivity (Lunne et al., 1997). Used derivations and approach for calculation of the Soil Behaviour Type Index, I_c (SBTI), and approximation of hydraulic conductivity is briefly covered in the following sections.

3.8.1 Soil Classification and SBTI

Based on performance data from CPTU, many charts have been developed to estimate soil type from derived parameters based on an ever growing database with results from CPTU tests (P K Robertson and Wride, 1998).

The soil classification charts proposed by (P. K. Robertson, 1990) uses the relationship of normalized cone resistance Q_{tn} over either normalized friction ratio F_r or the pore pressure ratio B_q, compared to database of soil samples, for classification.

Due to the behaviour of silt and mixed soil fractions like clayey sands and silty clays, a different consolidation condition occurs. Clean sands and clays are traditionally considered drained or undrained, while silt can display partial drainage, i.e. slower consolidation than sand, but faster than clay (Janbu, 1989). This alters the condition during CPTU penetration, as silt can bestow a partial partially drained condition, complicating the interpretation procedure (Bihs, Long, Nordal and Paniagua, 2021). A soil classification chart developed by (Schneider et al., 2008) takes the measure pore pressure u_2 into consideration, quantifying the soil classification of these mixed fractions or "transitional" soil. The soil classification chart by (Schneider et al., 2008) uses the relationship of normalized cone resistance Q_{tn} over change in measure pore pressure u_2 divided by the effective vertical in-situ stress σ'_{v0}.

From the soil behaviour type charts of (P. K. Robertson, 1990), an updated soil behaviour type index I_c SBTI was proposed by (P K Robertson and Wride, 1998), by initial work of (Jefferies, M et al., 1993). The updated SBT index estimates grain charactheristics from the previous mentioned SBT chart and is defined in Equation (3.16).

$$I_c = [(3.47 - Q_{tn})^2 + (logF_r + 1.22)^2]^{0.5} \tag{3.16}$$

3.8.2 Approximated Hydraulic Conductivity from SBTI

From the SBT index, (P. Robertson, 2009) proposed the following equations for approximation of hydraulic conductivity in m/s, based on the normalized SBT chart by (P. K. Robertson, 1990). The range of K derived from I_c for the different the SBT zones can be viewed in the modified Table 3.2, where SBT zones with I_c out of range is left out.

$$1.0 < I_c \leq 3.27 : K = 10^{(0.952-3.04I_c)} \tag{3.17}$$

$$3.27 < I_c < 4.0 : K = 10^{(-4.52-1.37I_c)} \tag{3.18}$$

According to (P. Robertson, 2009), the hydraulic conductivity estimated by the soil behavior type index I_c, must be considered as just an approximation.

Table 3.2: SBT classification by (P. K. Robertson, 1990) modified with suggested K range by (Lunne et al., 1997). Table adapted from (P. Robertson, 2009).

SBT Zone	SBT	Range of K [m/s]	SBT index, I_c [-]
2	Organic soils - clay	1.0E-10 to 1.0E-8	I_c >3.60
3	Clay	1.0E-10 to 1.0E-9	2.95 <I_c <3.60
4	Silt mixture	3.0E-9 to 1.0E-7	2.60 <I_c <2.95
5	Sand mixture	1.0E-7 to 1.0E-5	2.05 <I_c <2.60
6	Sand	1.0E-5 to 1.0E-3	1.31 <I_c <2.05
7	Dense sand to gravelly sand	1.0E-3 to 1.0	I_c <1.31

3.8.3 Rigidity Index Estimation

For estimation of in-situ horizontal coefficient of consolidation, rigidity index I_r, is required. This parameter can be estimated from CPTU results using Method-B by Krage et al., 2014, as seen in Equation (3.19). It requires input of initial shear modulus G_{max} and corrected cone resistance q_t along with best estimated stress in-situ stress parameters.

$$I_r = 0.26\left(\frac{G_{max}}{\sigma'_{v0}}\right)\left(\frac{1}{0.33\left[\frac{0.33(q_t-\sigma_{v0})}{\sigma'_{v0}}\right]^{0.75}}\right) \tag{3.19}$$

3.9 Hydraulic Conductivity in Triaxial Cell

3.9.1 Determination of Hydraulic Conductivity

In a standard triaxial apparatus the soil specimen can be tested under specific stress conditions, usually in-situ effective stress condition. After initial triaxial stages, the hydraulic conductivity test is initiated by an external water source, usually a pump or a volume controller that can provide a stable flow or pressure. Variations in either constant or falling head can be used, but only constant head for triaxial test will be covered in this thesis.

Based on characteristic or expectations of hydraulic conductivity for specimen of known soil fractions, a hydraulic gradient is usually predetermined. This ensures laminar flow so that Darcy's law is valid and prevents unnecessary migration of soil grains. The hydraulic gradient must also high enough to overcome the threshold gradient, to combat eventual deviations from linear Darcy's law (Hansbo, 2001).

Based on Darcy's law, the hydraulic conductivity for a constant head is calculated using Equation (2.7) and Equation (2.9), combined in Equation (3.20).

$$K = \frac{q}{A \cdot i} = \frac{\Delta V}{\Delta t \cdot A \cdot i} \tag{3.20}$$

The hydraulic gradient is determined by either set pressure change or achieved pressure change, depending on test arrangement. For constant flow rate test, ΔV and Δt is known while stable dh must be measured and determined. For constant head test its vice versa. It is important to do calculations with stable dh or ΔV to ensure laminar flow conditions.

By using Equation (3.21), the hydraulic conductivity determined in laboratory temperature is changed due to the dynamic viscosity of water being a subject for temperature (Standards Norway, 2019).

$$K_T = k_{test}\alpha = k_{test}\frac{\eta_{test}}{\eta_T} \tag{3.21}$$

Chapter 4

Øysand Research Site

This chapter presents the NGTS Øysand site and gives a brief overview of the stratification and characteristics. Lastly the chosen relevant parameters is presented.

4.1 Site Description

The Øysand research site is one of the five national test sites of the Norwegian Geo-Test Sites (NGTS) project, which provides test sites as field laboratories for geotechnical research. Field trials of Flow Cone and HPT was carried out at NGTS Øysand and laboratory tests were performed with samples from same site.

4.1.1 Location and Setting

Øysanden is a peninsula about 3.6 km^2 in total size and is located approximatley 20 km south-west from Trondheim city centre in Norway, see Figure 4.1, and consists of mainly farmland and housing. With the deglaciation of the region approximately 10,300 years ago, the land was subject to post-glacial rebound while relative sea-level felt and Øysanden was made by deltaic and fluvial sediments deposits on the seafloor from Gaula river (S. Quinteros et al., 2019).

Øysand research site is located on the east side of the peninsula close to the Gaula river, see red rectangle in Figure 4.1. The research site is mainly a small agricultural field and the site topography comprises of a flat surface around 2.4-3.0 m above sea level. The field starts from a 7 m high vegetation ridge in the south and expands north parallel with Gaula river and a local road for about 120 m. The field is approximately 160 m wide.

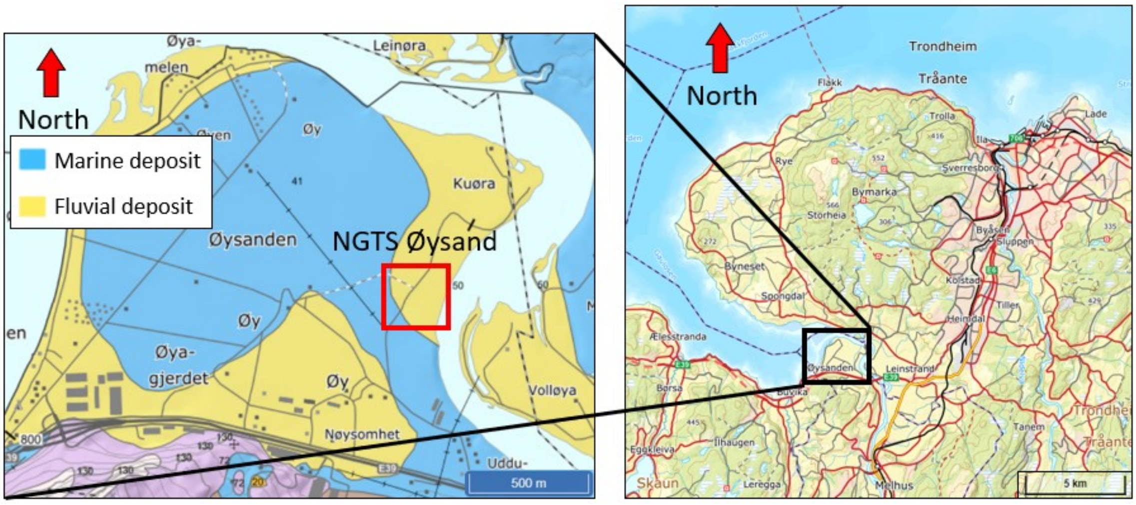

Figure 4.1: Geological map of Øysand (geological data from NGU).

4.1.2 Test Locations and Positions

The field tests was carried out at two locations within the NGTS site, approximately shown in Figure 4.2. Reviewed old field test positions and type is shown in Figure 4.3. Data from old tests was retrieved from NGI. Both test locations is around 2.6 m above sea level and consisted of ploughed agricultural top soil layer during the new field trials.

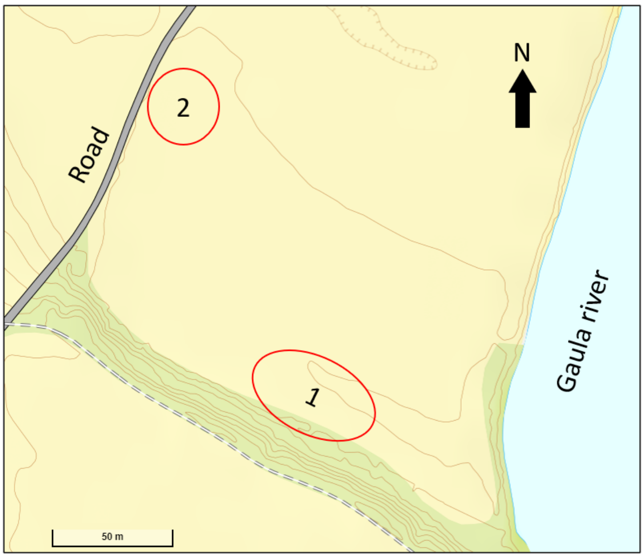

Figure 4.2: Planned test locations at NGTS Øysand.

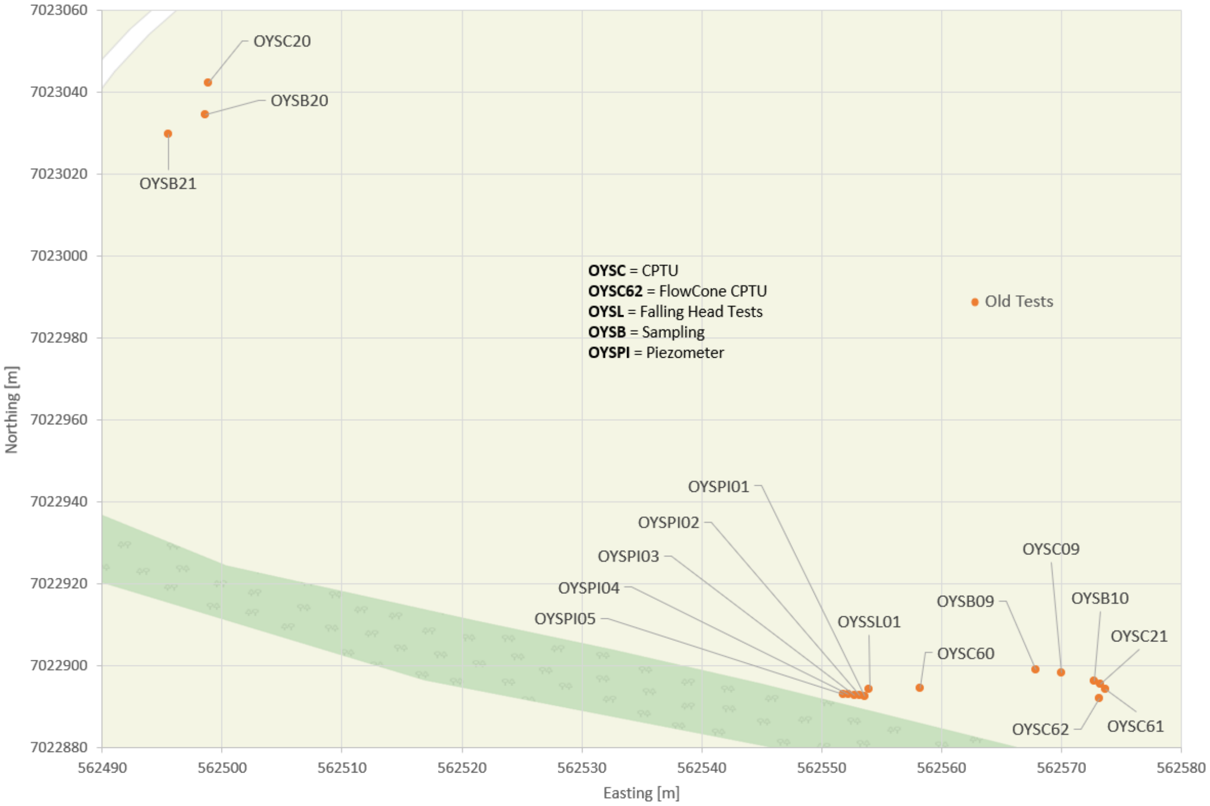

Figure 4.3: Positions of old field tests at Øysand.

Test location 1 is about 100 m from Gaula river, while test location 2 is about 170 m from the river.

4.2 Stratification

A comprehensive characterization of Øysand research site has previously been done, mostly by NGI, as part of a NGTS project. Due to the geological formation of Øysanden, the stratification contains several layers with lateral variability (S. Quinteros et al., 2019). The stratification is based on borehole samples and interpretation of in situ soundings and geophysical data down to about 20 m depth. Because of its daily purpose, the top soil of the field consists of agricultural soil. Below the surface, the soil is generally divided into two main units across the whole site, according to (S. Quinteros et al., 2019):

Unit I: First unit consists of 6-10 m coarse to gravelly sand.

Unit II: Second unit below consists of mostly fine silty sand, with some layers of clay and silt.

4.2.1 Test Location 1

Figure 4.4 shows soil stratification from borehole log OYSB09 at test location 1, interpreted by (S. Quinteros et al., 2019) with use of 54 mm soil samples, multi-sensor core logging and nearby OYSC09 CPTU test. The complete borehole log is given in Appendix A and the grain size distributions is presented in Appendix D. Performed soil classification of previous CPTU test results within test location 1 in Appendix C and Figure 4.6 generally reveals the same stratification as in Figure 4.4.

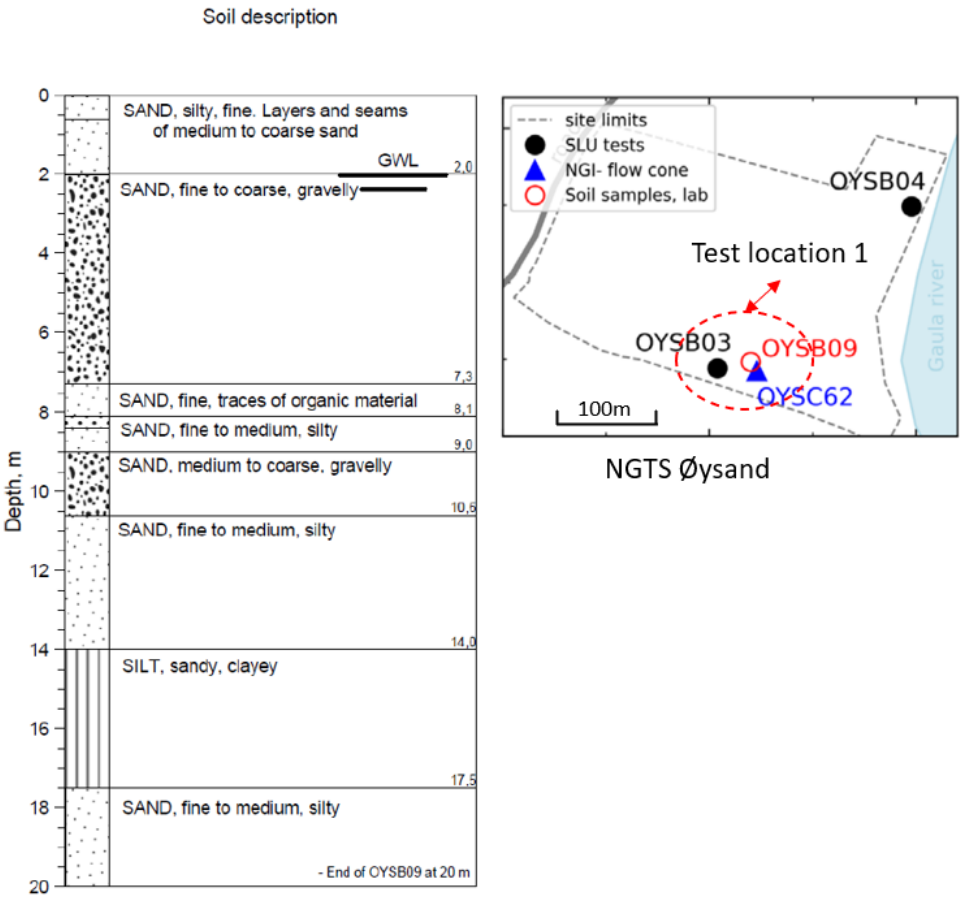

Figure 4.4: Stratification interpreted from borehole log OYSB09 at planned test location 1. Also showing previous field tests by (A. S. Gundersen et al., 2019) (figures adapted from S. Quinteros et al., 2019).

Old CPTU results reveal apparent local variability in the stratification, as seen in Figure 4.5. OYSC60 shows generally higher corrected cone resistance q_t in depth range 6-15 m. This gives an impact on the soil classification seen in Appendix C, as the Robertson 1990 classification for OYSC60 within the range 6-15 m is mostly classified as soil behaviour type zone: 6. Sands - clean sand to silty sand. For comparison OYSC61, OYSC62 and OYSC09 within the same depth range classifies mostly as soil behaviour type zone: 5. Sand mixtures - silty sand to sandy silt. The same pattern within the same depth range can also be seen for Schneider et al. 2012 classification, where OYSC60 classifies as mostly soil type: 2. Essentially drained sands where as the other positions include more soil type: 3. Transitional soils.

Corrected cone resistance, q_t, for OYSC09 and OYSC21 in Figure 4.5 reveal a hard layer of estimated gravelly sand at depth around 4 m. This is also shown as a thin layer in Figure 4.6. The linear straight line of q_t and f_s for OYSC09 from 4 m depth to 6 m depth is due to a stop, because of high cone resistance. Given stratification, corrected cone resistance q_t, soil content and soil classification in Appendix A and Appendix C was used to plan field tests at location 1.

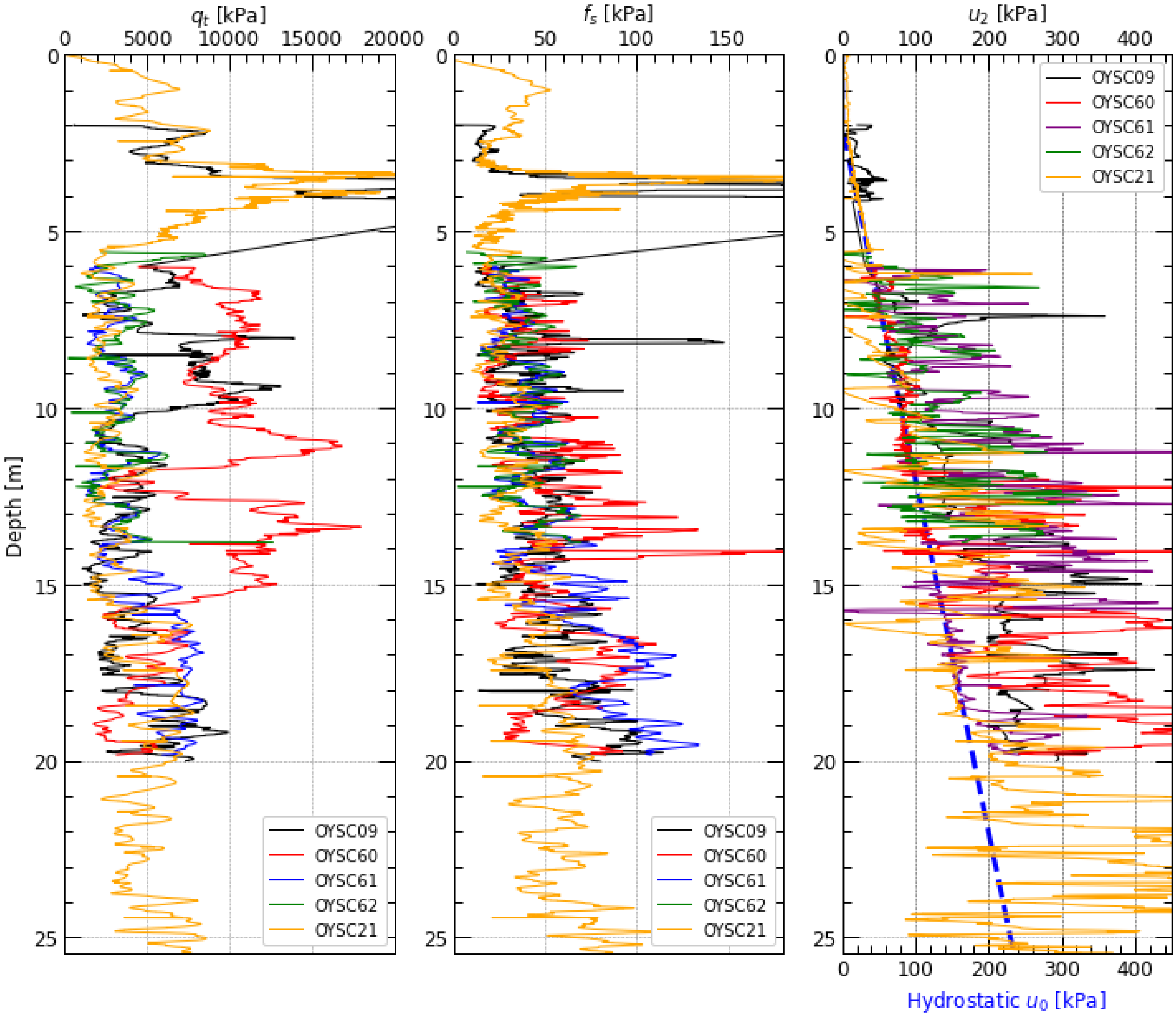

Figure 4.5: Old CPTU results for test location 1.

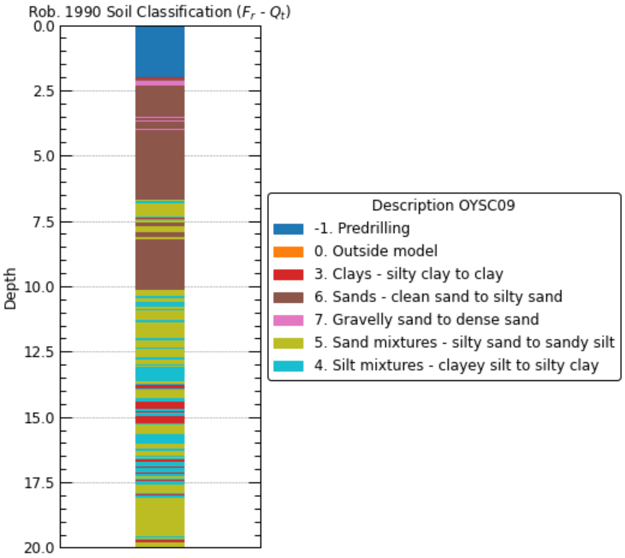

Figure 4.6: Robertson 1990 soil classification of OYSC09.

Results from 5 in-situ piezometer positions at test location 1, see Figure 4.3, is shown in Figure 4.7 with installation depth. The piezometers recorded pressure once every day from 2017 to 2021. Figure 4.7b shows comparison of assumed hydrostatic GWL starting from 2.0 m below surface and min/max results from piezometers. On average the groundwater pressure acts hydrostatic, but with ± 10 kPa cyclic variation due to tide.

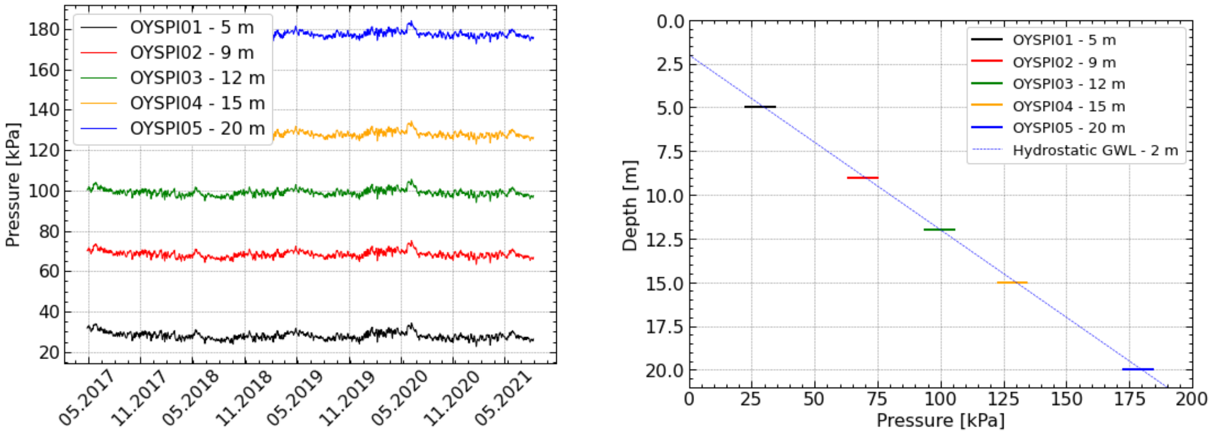

(a) Piezometer readings **(b)** Hydrostatic GWL and piezometer variability

Figure 4.7: Piezometer readings and assumed hydrostatic GWL at test location 1.

4.2.2 Test Location 2

Figure 4.8 shows stratification at test location 2 interpreted by (S. Quinteros, 2022) with use of soil sampling, CPTU, and SDMT (seismic dilatometer). The complete borehole log is given in Appendix B. GWL is the same as for location 1, with hydrostatic increase in groundwater pressure from depth 2.0, according to (S. Quinteros et al., 2019).

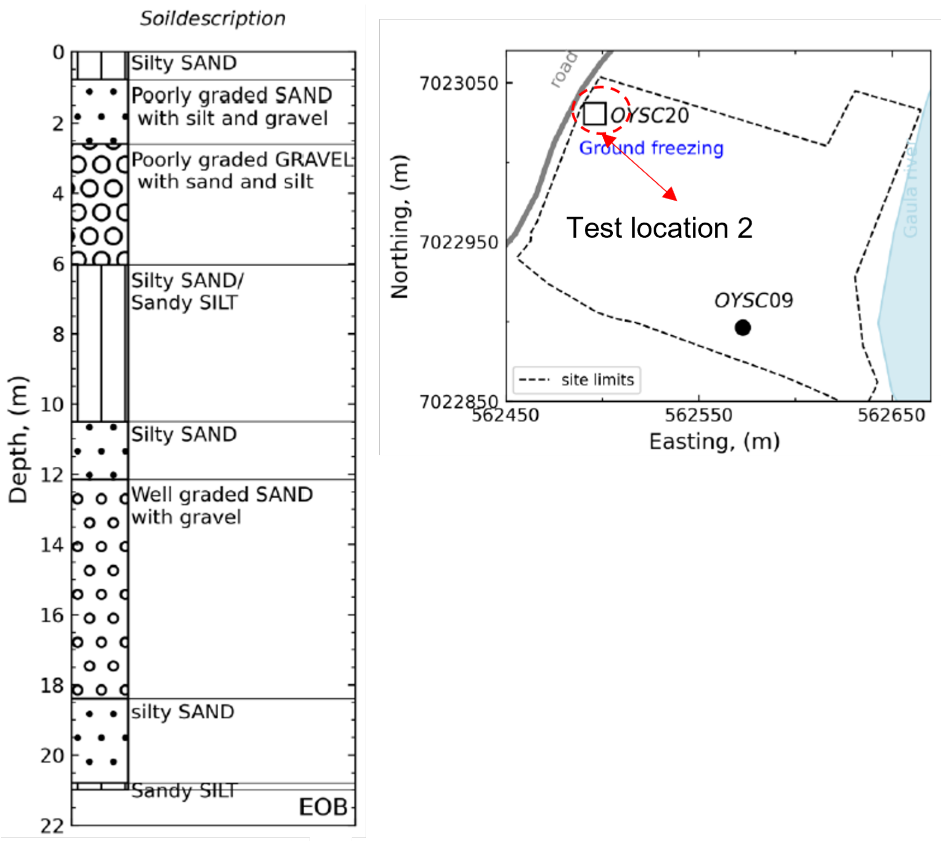

Figure 4.8: Stratification at test location 2 (figures adapted from S. Quinteros, 2022).

Performed soil classification of OYSC20, presented in Figure 4.10 and Appendix C, coincides well with the stratification given in Figure 4.8. CPTU results from OYSC20, starting from 6.5 depth, presented in Figure 4.9, along with complete borehole log in Appendix B was used to plan field test at location 2.

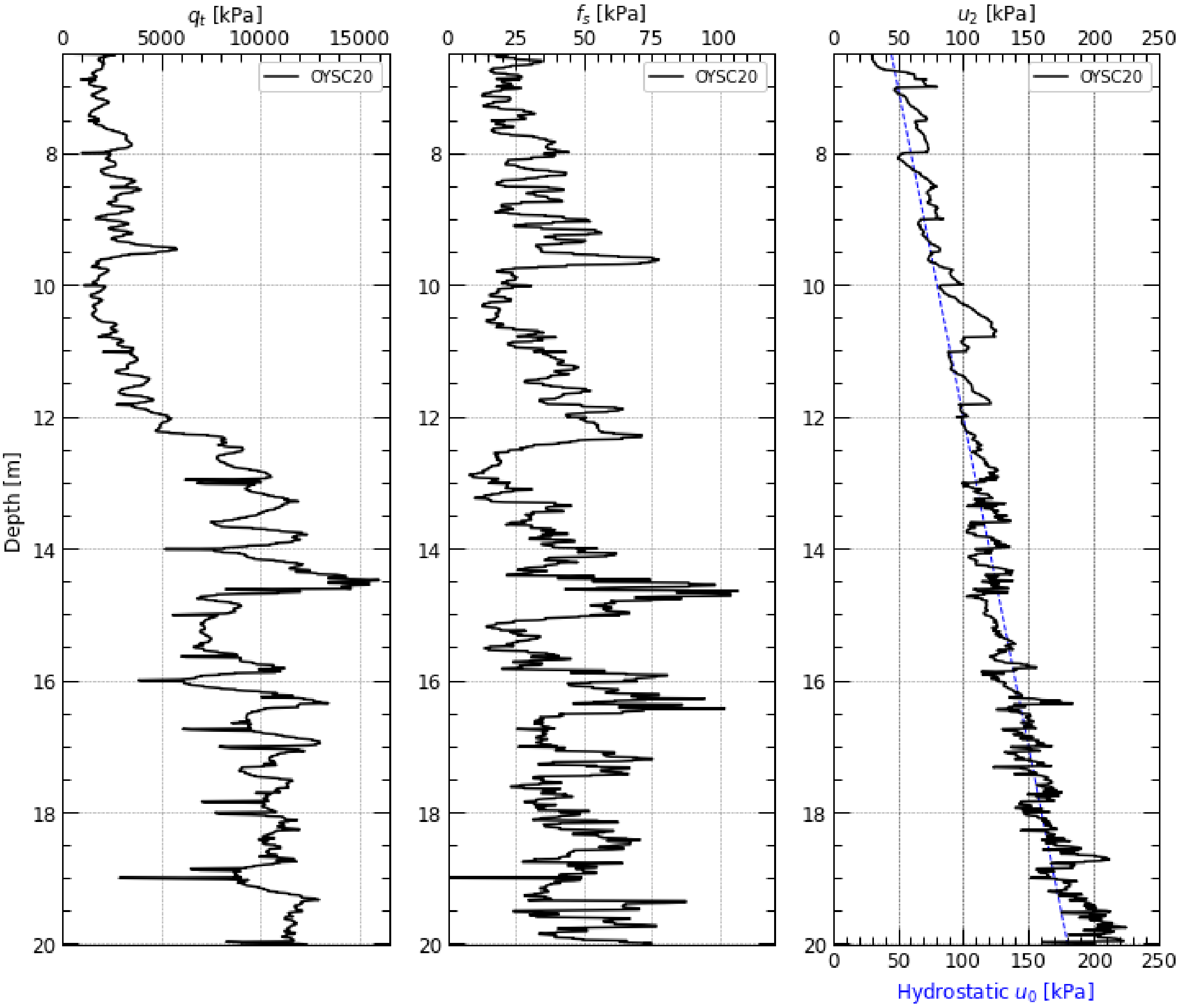

Figure 4.9: Old CPTU results for test location 2

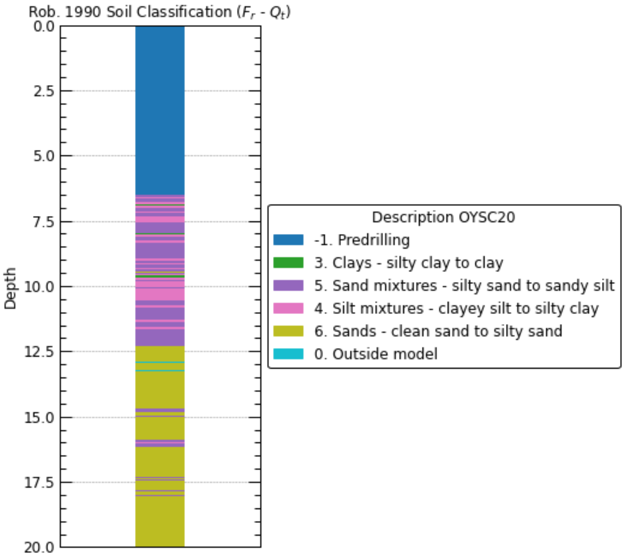

Figure 4.10: Robertson 1990 soil classification of OYSC20.

4.2.3 Comparison of Test Locations

Location 2 differs from location 1 with overall more gravelly content and less fine grained content in depths below 12 m, as seen in stratification and content diagram in Appendix A and Appendix B. The corrected cone resistance q_t increases towards and stays around 10 MPa below 12 m depth for OYSC20 in Figure 4.9, while lower resistance around 3-5 MPa is present for results in Figure 4.5, but with local variability. Both locations offer sand and silt mixtures to be tested for hydraulic conductivity.

4.3 Preparations for Field and Laboratory Tests

Test location 1 was chosen due to previous trial of Flow Cone system and falling head tests by (A. S. Gundersen et al., 2019), along with available CPTU data and stratification. Test location 2 was chosen due to available CPTU data, stratification and samples from previous ground freezing experiment done by (V. S. Quinteros and Carraro, 2023).

4.3.1 Parameters

Relevant parameters for preparation of field and laboratory tests were chosen based on results from (S. Quinteros et al., 2019) for test location 1 and Appendix B for test location 2.

Unit weight

From results presented in Figure 7(e) in Appendix A, the unit weight γ profile of borehole OYSB09 shows quite scattered results the first 4 m, between 15 kN/m^3 and 22 kN/m^3. This is because of sampling process issues (S. Quinteros et al., 2019). From 5 m to 20 m depth the unit weight ranges between 17 kN/m^3 and 20 kN/m^3, but with most result points at 19 kN/m^3.

The unit weight results from borehole OYSB20 in Appendix B, Figure 4.4(e), are beyond the main soil of interest for this thesis, due to high gravel content. Therefore, a representative average unit weight profile of 19 kN/m^3 is chosen for both test locations.

Coefficient of Earth Pressure at Rest

For the laboratory tests at location 2, the coefficient of earth pressure at rest, K_0, is chosen from Figure 24(b) in (S. Quinteros et al., 2019), where CPTU data has been used to determine K_0 values with depth. The most relevant CPTU test is OYSC20 and for the depth range of soil samples, a $K_0 = K_0'$ value of 0.38 at depth 10.0 m is chosen for frozen samples from OYSB21.

From the same figure, K_0 value for laboratory specimen from OYSB10 is interpreted from estimated K_0 by OYSC10 and set to 0.43, a bit higher than for samples from OYSB21, due to lower depth range.

4.3.2 Flow Cone Tests

Flow Cone tests was initially intended to be tested at test location 1, close to old Flow Cone test done by (A. S. Gundersen et al., 2019), but was moved to test location 2, see Section 5.1.2.

Flow Cone stationary tests, see Section 3.1, is aimed to be performed in granular soils, like sand or silt mixtures. From stratification in Figure 4.8 and resistance q_t in Figure 4.9, two test depths for stationary tests were chosen: 8.0 and 10 m.

4.3.3 HPT Tests

The HPT penetration phase, see Section 3.2, is aimed to be performed in mainly sand and silt mixtures to be compared with Flow Cone and previous hydraulic conductivity tests. The main layer of interest is between 5-16 m depth, see Figure 4.4, but penetration phase was run down to 20.6 m depth to also test HPT at deeper levels.

Tests depths for HPT stationary phase, see Section 3.2, was chosen for optimal dissipation speed and to be within the same range as planned falling head tests for comparison.

4.3.4 Falling Head Tests

From stratification in Figure 4.4, filter depth locations is chosen to represent the main soil layers of interest, for comparison to older and new field tests. The installation also provides opportunity to measure the depth to groundwater, for comparison of old piezometer readings. The chosen depths are: 7.6, 12.2, 9.2 and 16.7.

Chapter 5

Field Testing

This chapter presents an overview of the performed field tests and thorough run-through of the executed procedures.

5.1 Procedure of Field Tests

This section gives an overview of the performed field tests and an explanation of the procedure of each in-situ test. Every test and water pipe installation was prepared using pre-drilling to various depths using rotary pressure technique and normal total sounding 57 mm drill bit with 44 mm rods. Table 5.1 shows a complete list of technical equipment and rods used in the different field tests.

Table 5.1: Equipment used for field tests at Øysand.

Test type	Technical equipment	Rods
Flow Cone	Flow Cone control module FCHM1 Geotech Nova CPTU probe 5657 10 cm^2	1 inch standard water pipe length 2 m CPT add-on rod
HPT	FI6000 Field instrument K6300 HPT flow controller HPT K6052 probe	36 mm CPT length 2 m
Falling head tests	Geotech bronze filter tip Solinst Levelogger 5 LT M100 Solinst Barologger 5 LT M1.5	1 inch standard water pipe length 2 m

5.1.1 Performed Field Tests

The field tests at Øysand were performed during week 16-18 of 2023 by the author of this thesis and with help from personnel and Geotech 607 boring rig from NGI. Table 5.2 shows an overview of the performed tests with depths according to Section 4.3.2, Section 4.3.3 and Section 4.3.4. Figure 5.1 display new field tests positions, with relevant old positions.

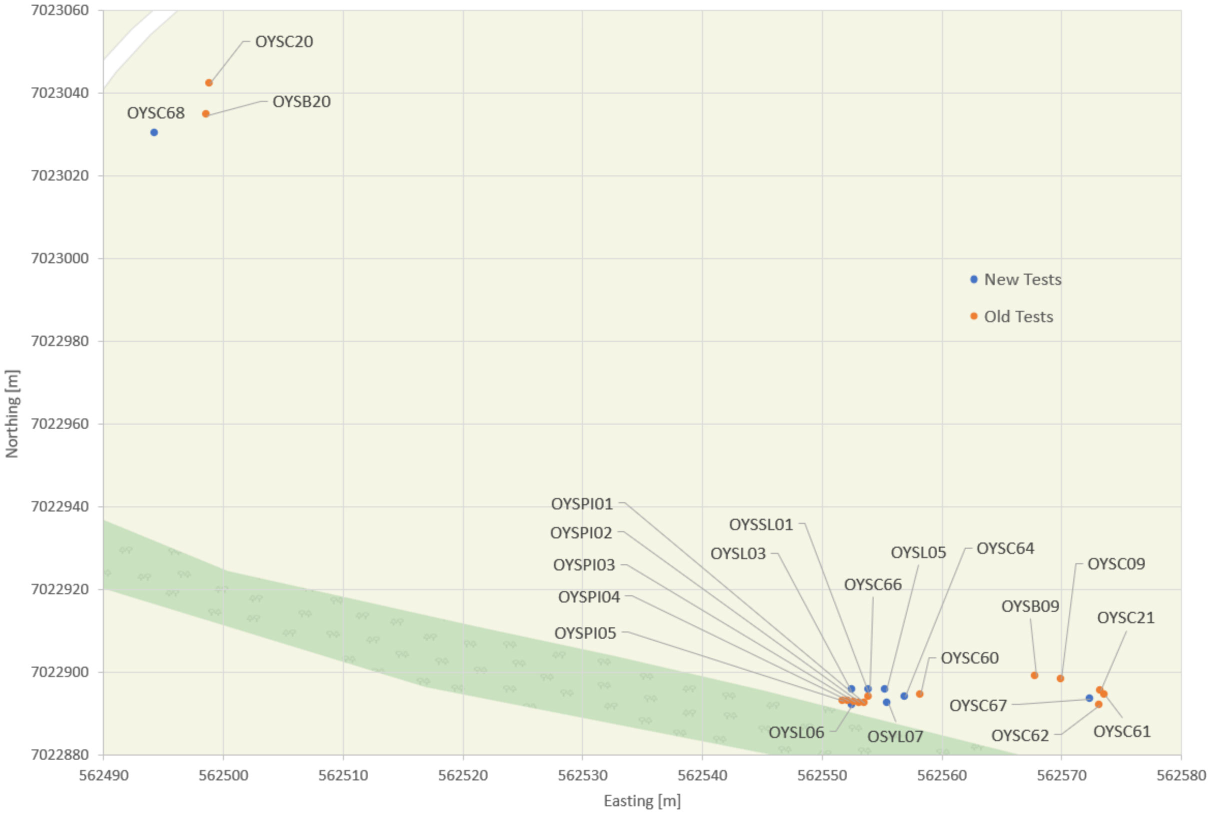

Figure 5.1: Performed field tests at Øysand. Flow Cone and HPT locations marked with CPTU symbol.

Table 5.2: Overview of performed field tests.

Type	Test type	Location ID	Number of tests	Depth range bgl*	Date
Flow Cone	Penetration w/CPTU	OYSC68	1	6-10.83 m	25.04.23
Flow Cone	Constant flow rate	OYSC68	6	Tests at 7.9 m**	25.04.23
Flow Cone	Constant flow rate	OYSC68	6	Tests at 10.0 m**	25.04.23
HPT	Penetration	OYSC64	1	0-20.6 m	17.04.23
HPT	Dissipation	OYSC64	5	***	17.04.23
HPT	Penetration	OYSC66	1	0-20.6 m	24.04.23
HPT	Dissipation	OYSC66	4	***	24.04.23
HPT	Penetration	OYSC67	1	0-20.6 m	24.04.23
HPT	Dissipation	OYSC67	4	***	24.04.23
Falling head	-	OYSL03	2	7.6 m**	19.04.23****
Falling head	-	OYSL05	2	12.2 m**	20.04.23****
Falling head	-	OYSL06	2	9.2 m**	20.04.23****
Falling head	-	OYSL07	2	16.7 m**	20.04.23****

* bgl = below ground level
** Mid filter location (depth).
*** Dissipation tests performed at various depth locations.
**** Date installed. Tests performed at varying dates after installation

5.1.2 Flow Cone With CPTU Test Procedure

Initial Deviation

Initially, Flow Cone was set to be tested at location OYSC66 but due to unexpected high resistance in the FCHM2 hydraulic module during saturation of the system above surface, location OYSC66 was assigned to HPT testing. The updated hydraulic module, with never-before-tested bronze filters and assembly compartment, gave higher than expected resistance to outflow above surface, where the outflow should be effortless. Subsequently, flow tests to verify system pressure sensor, hydraulic tube, hydraulic tube in compartment without surrounding bronze filter and final assembly was performed. Every test before the final, lock-and-tight assembly of FCHM2, gave normal expected pressure readings. Due to shortage of time further testing of FCHM2 could not be performed and Flow Cone testing with the old FCHM1 was moved to location OYSC68, test location 2, were it has not been tested before and for comparison to the frozen soil samples tested in laboratory.

Test for Correction of System Flow Resistance

To obtain the correct pore pressure u_f, the measured pore pressure $u_{f,m}$ was be corrected for resistance in the hydraulic tube, valves and other parts of the system. A setup as viewed in Figure 5.2 was used.

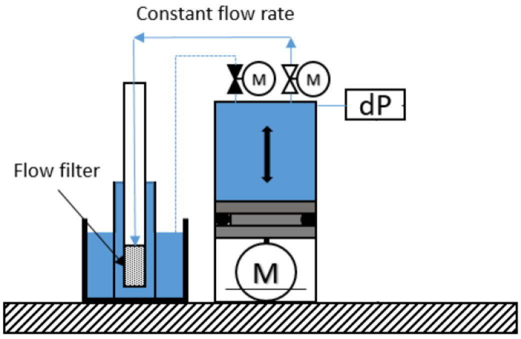

Figure 5.2: Flow Cone system resistance idealized setup (adapted from A. S. Gundersen et al., 2019).

Test Procedure at OYSC68

Flow Cone system was set up at test location 2 along with the boring rig and other equipment, see Figure 5.3. Initially a system flow resistance test was performed using de-aired water, which was also used for the actual Flow Cone run at OYSC68. Due to top layers containing gravel, as seen in Figure 4.8, pre-drilling was done down to 6 m depth to prevent unnecessary wear and tear to CPTU probe and FCHM1. The standard water pipe rods used for advancing down the subsurface were pushed down using clamp mode. These would most likely buckle or be clamped flat if pushed down the first layers at 0-6 m depth.

Right before assembly, the CPTU probe was prepared and saturated after standard procedure while the FCHM1 was chambered and saturated, making sure no air was within the system. After assembly, Flow Cone and CPTU probe were initiated at zero datum, top of the pre-drilled borehole, and advanced down pre-drilled soil with outflow 50 ml/min from Flow Cone filter. At 6 m depth, the probe started to advance through virgin soil at normal CPTU speed of 2 cm/s with penetration 50 ml/min outflow from the filter. Stationary constant flow rate tests, Figure 3.2, was performed at two depths with different flow rates. When reaching test depth, penetration outflow was switched off and the measured pressure was allowed to dissipate to stable, assumed hydrostatic pressure. After the first stationary test, the probe advanced down with 40 ml/min outflow until reaching the next test depth. After the last stationary test, the penetration outflow was turned up to 60 ml/min while the probe was pulled up and the test ended.

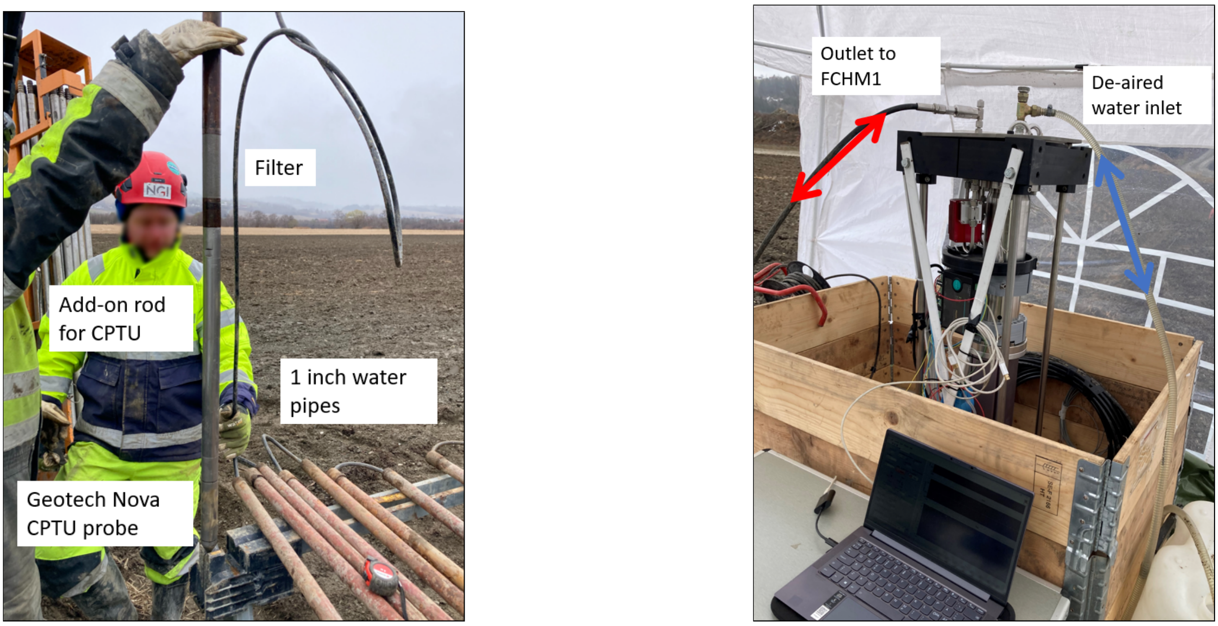

(a) FCHM1 assembled and ready for test. **(b)** Flow Cone pump and control PC.

Figure 5.3: Flow Cone setup at OYSC68.

5.1.3 HPT Tests Procedure

All HPT tests were executed at test location 1, viewed in Figure 5.1, and started with pre-drilling to 5 m depth to avoid much of the top gravelly sand layer, as displayed in Figure 4.4. The same procedure was done at every HPT test and followed instructions from HPT manual, summarized in (Wesley McCall and Christy, 2020).

The HPT system was setup as shown in Figure 5.5 and tests started with a pre-log QA, where both the Wenner electrical conductivity array and the HPT probe pressure sensor was tested. The Wenner array was tested in accordance with Figure 5.4. A loader sends currents and the operating software controls the readings from the Wenner array. The HPT pressure sensor was tested in the HPT reference tube, also used for Flow Cone system resistance test as shown in Figure 6.3, and logged atmospheric pressure and verified that the pressure sensor could measure a head pressure difference of 1.524 kPa or 15.24 cm water within accuracy limits.

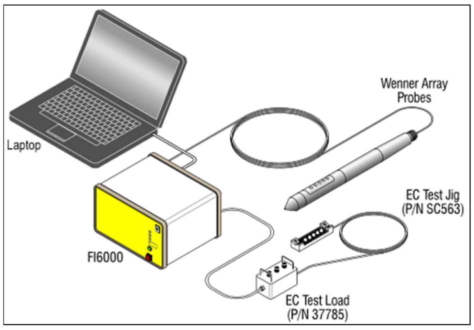

Figure 5.4: HPT QA EC test (screenshot from operating DI Acquisition software).

After the pre-log QA tests, HPT testing was initiated at zero datum, surface of the pre-drilled boreholes, and advanced down at speed 2 cm/s using clamp mode and a string potentiometer attached to the boring rig head for accurate depth measurements. The chosen outflow during penetration phase was 200 ml/min with normal tap water for all runs at test location 1 and logging was paused during rod adding. Stationary dissipation tests were aimed at depths given in Section 4.3.3, but was adapted according to live EC and HPT pressure readings. The depth position correlates to the HPT probe filter tip. Low EC and HPT pressure readings correlates with increasing permeability and reduces the time spent on each dissipation test. Each HPT log was stopped at around 20.6 m and pulled up with the same outflow. After each log run, post-log QA tests were conducted, with the same procedure as pre-log QA tests. This to ensure that the system was operational during penetration and measured data is valid.

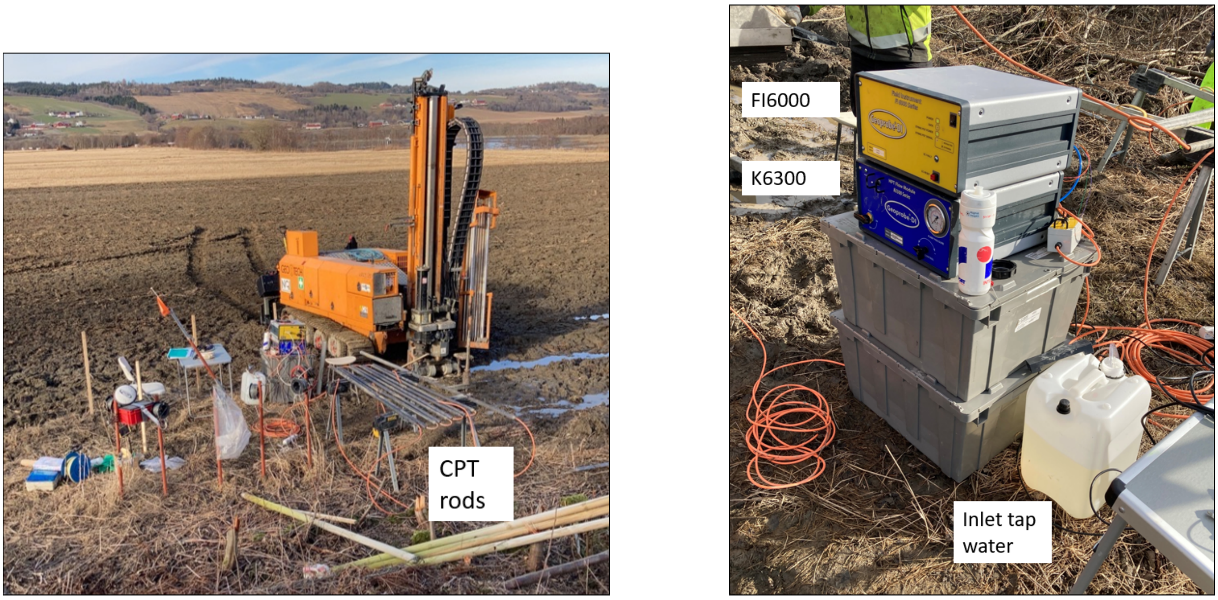

(a) Overview of HPT test OYSC64 **(b)** HPT instrumentation at field tests.

Figure 5.5: HPT test setup at OYSC64.

5.1.4 Falling Head Tests

Before installation of 1 inch water standpipes, pre-drilling was performed to an offset depth of approximately 80 cm above mid-filter location to ensure that the bronze filters was pushed down into undisturbed soil. During installation each connection between rods were fitted with thread seal tape and topped with tap water to reduce clogging of the filter while advancing down, as seen in Figure 5.6. The filter was pushed carefully into the undisturbed soil towards designated depth location.

Before every falling head test, both loggers were programmed in a linear sampling mode, starting and ending at a set time, with a set sampling rate, before they were installed. The levelogger was lowered inside the water pipes to a certain, chosen depth with a small rope. The falling head tests were performed by sudden injection of a known volume of water, i.e. introducing a pressure head to the soil surrounding the filter, and measuring the decrease in head with time using the loggers, as displayed in Figure 3.4. Only one levelogger was available, therefore only one falling head test could be performed simultaneously.

Figure 5.6: Installation procedure of water stand pipes

5.2 Previous Frozen Ground Sampling

5.2.1 Soil Sampling and Ground Freezing

Soil sampling for geotechnical purposes can be performed with various techniques dependent on desired information outcome. For determination of hydraulic conductivity on undisturbed soil samples in laboratory tests, NS-EN 1997-2:2007+NA:2008 demands soil sample quality class 1 or 2 (Standards Norway, 2008). This usually requires a push piston or block sampling technique. For granular soils, such as gravel, sand and mixtures, sampling undisturbed soil quality class 1 or 2 is very hard to accomplish. Usually, granular soil gets reconstituted to estimated in-situ volumetric relationship void ratio in the laboratory, but the in-situ initial fabric will remain inaccessible to replicate. To access undisturbed samples of sand, silt or mixtures, state-of-art soil sampling techniques still impose risk of disturbing the initial fabric of the specimen (V. S. Quinteros and Carraro, 2023). Therefore the soil needs to be stabilized before extraction. According to (V. S. Quinteros and Carraro, 2023) this can be achieved by either ground freezing or soil impregnation with different locking chemical substances. To achieve undisturbed specimens with ground freezing, the soil should to be insusceptible to frost heave. Simply put, it requires absence of frost-heave applicable silt fractions (Saetersdal, 1981). For clean sands, undisturbed state can be achieved by radial freezing of the soil. As the frost front expands radially, the pore water is expelled and drained by the frost front moving outwards. If there is any volumetric expansion of the soil due to the freezing, horizontal stresses will increase due to the sand being confined by the frost front (Yoshimi et al., 1978).

5.2.2 Ground Freezing at Øysand

Ground freezing technique was performed by (S. Quinteros et al., 2019; V. S. Quinteros and Carraro, 2023) to stabilize fluvial sandy soil layers at test location 2, see Section 4.2.2, between April and May in year 2019. The main layers of interest for the study by (V. S. Quinteros and Carraro, 2023) was the well graded sand layer, see Figure 4.8, in depth range 12.0 - 18.2 m. For this thesis, the main layer of interest at test location 2 is within the depth range of Flow Cone testing, around 7.9 - 10.0 m. A trimmed specimen from depth range 10.2 - 10.4 m was kindly contributed by (V. S. Quinteros and Carraro, 2023) from NGI.

Initial experiments performed by (V. S. Quinteros and Carraro, 2023), to determine what layers at test location 2 were receptive for ground freezing, concludes that silty sand/sandy silt layer in depth range 6.0 - 10.5 m, see Figure 4.8, is expected to expand during ground freezing. This will be assessed by visual inspection of triaxial specimen and deformation during test. The GSDC presented in Appendix E and soil fractions for each trialled test also contributes to this expectation.

Ground Freezing Procedure

The executed procedure of ground freezing at Øysand in 2019 is outside the scope of this thesis. For further details, see (V. S. Quinteros and Carraro, 2023). The specimen contributed to this thesis is from borehole OYSB21, where 103 mm samples were extracted out using a special coring system, with length about 1.5 m. OYSB21 is located 40 cm from centre-centre freezing pipe OYSB18, not shown in Figure 4.3. Pre-trimmed frozen specimen FGS1 is shown in Figure 5.7. FGS1 has been kept in a frozen state since extraction from Øysand in May 2019.

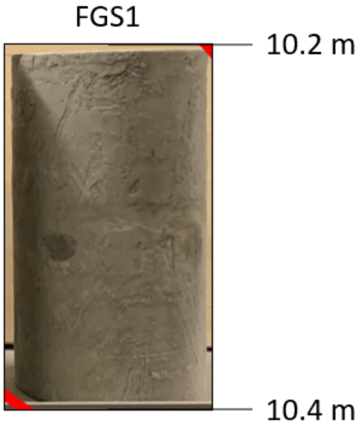

Figure 5.7: Original trimmed 103 mm frozen ground specimen from Øysand.

5.3 Procedure of Preparing Frozen Triaxial Specimens

5.3.1 Trial Coring

From experience of trimming, cutting and coring the frozen specimens by (V. S. Quinteros and Carraro, 2023), a coring plan was made, see Section 5.3.2. Unfortunately, equipment for coring out 54 mm samples from FGS1 was not available to be moved into a temperature controlled room. Therefore an old 73 mm tube from push piston sampling at test location 1 was extruded and a dummy specimen named 1Bf was cut and put in a -21°C freezer for a period of twelve days. Other cuts from same piston tube was sliced open to visually confirm the soil content, being sand with assumed silt and other fine grained content.

A trial 54 mm coring with an air vented diamond cup drill bit in 20°C room was performed on 1Bf to see effects of coring, see Figure 5.8. The coring took about 20 seconds to perform and most of the heat dissipated outwards, as noticed on the plastic encased scrap rests. The upper horizontal edge proved vulnerable and resulted in a damaged part, as seen in Figure 5.8b. The temperature of the cored 54 mm part was not measured, but it was still frozen after the coring procedure.

The results from trial coring of 1Bf showed acceptable cut edges and negligible temperature loss. In addition to coring, 1Bf showed that the horizontal edges of specimens are due for trimming to accomplish an acceptable flat circular surface.

(a) 1Bf trial coring 1.

(b) 1Bf trial coring 2.

Figure 5.8: Trial 54 mm coring of sample 73 mm 1Bf at NGI laboratory.

5.3.2 Coring of Frozen Triaxial Specimens

Coring plan can be seen in Figure 5.9 and resulted in 3 specimens; 2 horizontal and 1 vertical. Coring and trimming was executed with haste to prevent temperature loss in specimens. Initially FGS1 was cut into three pieces and brought back to the -21°C freezer. Every specimen was cored, trimmed and kept in freezer one day prior to installation in triaxial cell. The resulting dimensions of specimens by executed coring in shown in Table 7.1.

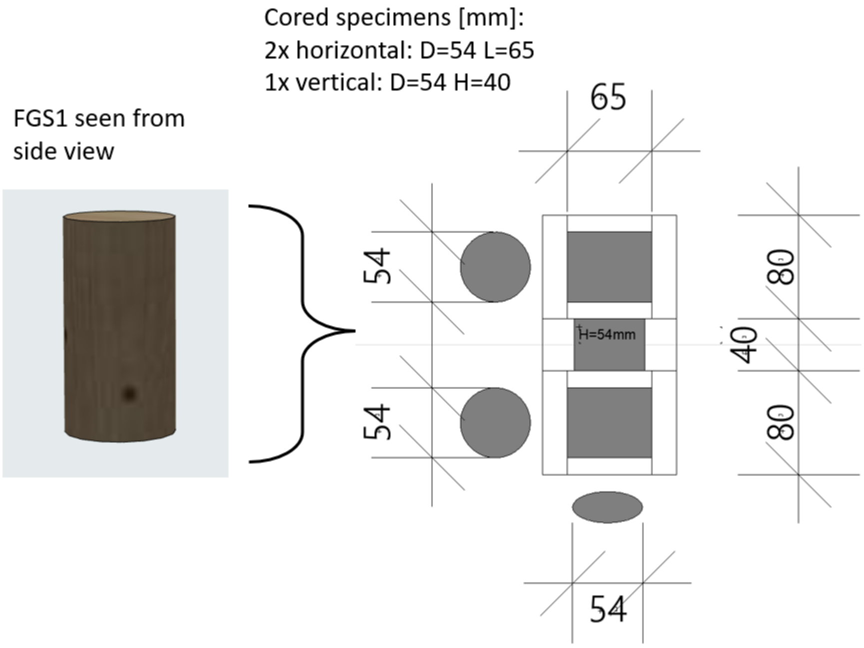

Figure 5.9: FGS1 coring and trimming plan. White areas are cut-offs.

5.3.3 Build-in Procedure of Frozen Specimens in Triaxial Cell

In order to keep the thawing process under control, all frozen specimens were measured and installed in a triaxial cell within a temperature controlled room, a walk-in freezer kept at -9°C. Prior to each installation the triaxial base pedestal and plexiglass cover with axial load rod and sensor was washed and dried before being cooled for minimum twelve hours within the walk-in freezer.

Initially, weight and dimensions of the specimen were measured prior to installation on the triaxial base pedestal. A 0.5 mm thick impervious nitrile membrane was trimmed and measured for correction factors, dimensions and strain, before being carefully wrapped around the specimen, top cap and bottom cap with porous filters. The membrane was cooled for a while in the walk-in freezer and grease was applied to bottom and top cap to create a better watertight seal between prior to wrapping. The membrane was sealed using 4 O-rings, two on the bottom cap and two on the top cap. Thereafter, a vacuum of -20 kPa was applied to remove air between membrane and specimen, as seen in Figure 5.10. Then the circumference and height with vacuumed membrane was measured using a millimeter band with -0.02 cm correction and a Mitutoyo millimeter frame. Five heights and three circumference measurements were performed to apply mean values for specification sheet used in the triaxial controlling software.

Figure 5.10: Installation of specimen 2Bf on triaxial base pedestal in walk-in freezer. Also showing applied vacuum -20 kPa.

The installation in the walk-in freezer was finished by locking in the plexiglass cover to the triaxial base and filling the cell with an -36°C anti-freeze liquid, glycol with brand name Xstream-G30. The liquid was applied slowly from the bottom of the triaxial base using a funnel and a hose with applied head difference. The glycol was allowed to squirt out before closing the top valve to ensure no air within the cell. Figure 5.11 shows triaxial cell ready for setup and connection at testing bench in laboratory room temperature (21°C ± 0.5°C).

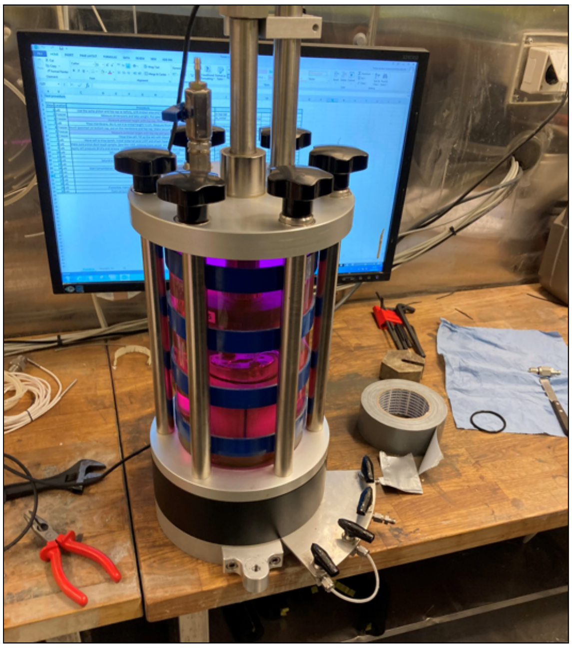

Figure 5.11: Finished installation of specimen 2Bf in triaxial cell with glycol.

5.3.4 Triaxial Testing Bench Setup

The built-in specimens were brought from the walk-in freezer to a designated triaxial testing bench at NGI laboratory. The thawing process starts immediately when exiting the walk-in freezer, but the triaxial cells were quickly connected to the testing bench setup. This process took about 6 minutes and temperature measurement with hand-held infrared thermometer still showed negative temperatures after setup was complete.

A very simplified sketch of the triaxial testing bench setup is shown in Figure 5.12. All transducers and sensor, except the load sensor, was at room temperature prior to setup of frozen triaxial cell. The GDS pressure/volume controller pumps initiate cell- and back-pressure within the triaxial cell with de-aired water, while the axial linear variable differential transducer (LVDT) measures axial deformation. The differential pressure transducer measures pore water pressure within the specimen and the load sensor measures axial load. The axial load frame pedestal applies load to the specimen. All of these are monitored and controlled with PC software, ModLab, connected via a data acquisition system.

A custom glycol - water interface pressure chamber was set up for separation of glycol and de-aired water from the back pressure pump. This did not work completely as intended, as the glycol mixed with water, but it made sure that no 100% de-aired water entered the cell while temperatures were below negative degrees.

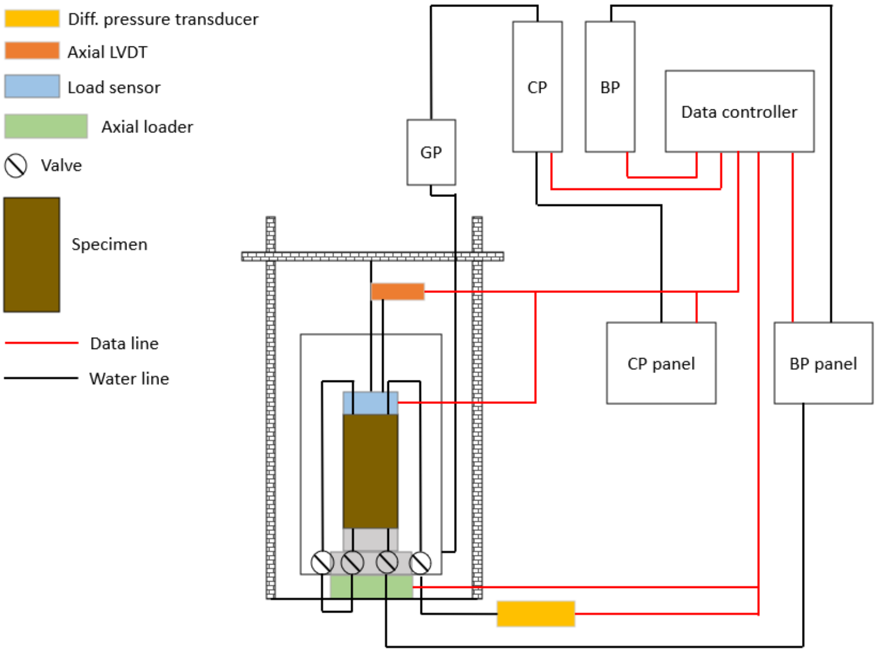

Figure 5.12: Simplified model of used setup at triaxial testing bench during thawing, saturation and consolidation. BP = back pressure GDS pump, CP = cell pressure GDS pump and GP = Glycol - water interface pressure chamber.

A photo of the actual triaxial setup used during thawing, saturation and consolidation is shown in Figure 5.13. The load frame, bars filled with dotted symbols in Figure 5.12, was locked in place. This can also be seen by hand-screw tuners in the top of the frame in Figure 5.13.

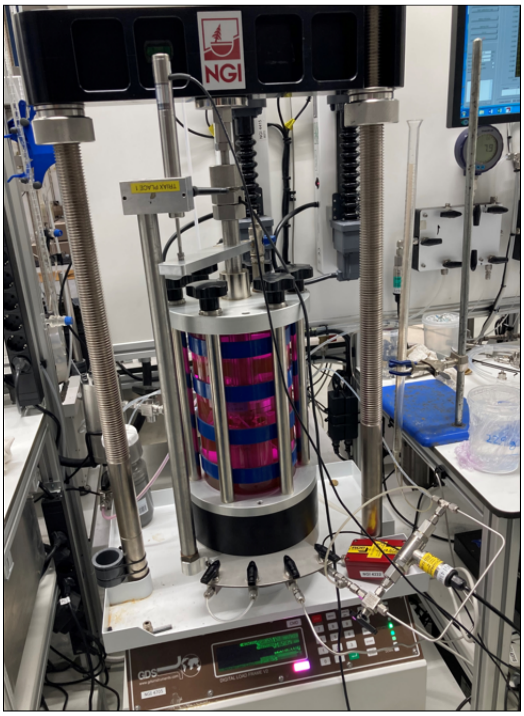

Figure 5.13: Photo of triaxial bench setup with frozen specimen.

5.4 Procedure of Triaxial Hydraulic Conductivity Test

The test phases for the triaxial hydraulic conductivity test after setup was the following: (i) thawing, (ii) flushing, saturation and B-value check, (iii) Consolidation, slightly anisotropic (iv) hydraulic conductivity test and (v) dismounting.

5.4.1 Initial Start and (i) Thawing

Immediately after connecting the cell to the system and initial zero calibration of load sensor, a very small axial load of 0.001 kN was applied with the axial loader frame. This was done to ensure that the axial LVDT and top load sensor had connection to the specimen. Second zero calibration of axial LVDT was done immediately after a visible touchdown of the load cell on the top cap of the specimen. The small axial load of 0.001 kN remained applied for all test phases, resulting a very small anisotropic stress state for the specimens, where $\sigma_1 = \sigma_a = \sigma_{cell} + F/A_0$ and $\sigma_2 = \sigma_3 = \sigma_r = \sigma_{cell}$ resulting in $\sigma_a - \sigma_r \approx 0.44$ kPa based on initial area. This is only for the purpose of maintaining contact between the load cell and the specimen, so LVDT can read axial deformation. The load frame was set to contain F = 0.001 kN with very minor increments in action, upwards or downwards movement by the bottom plate pedestal, to follow deformation of the specimen.

The vacuum of -20 kPa was released slowly by fine tuning of the pressure pumps, applying small increments in confining cell pressure set at 20 kPa while vacuum was released, to maintain effective confining stress at 20 kPa for the still frozen specimen. 20 kPa effective confining stress was chosen based on previous thawing trials by (Sivathayalan, S and Vaid, Y, 2004; V. S. Quinteros and Carraro, 2023).

Thawing was performed radially inwards by the cell fluid, i.e. glycol, going from -9°C towards room temperature 21°C ± 0.5°C, with 20.44 kPa effective stress initiated by cell pressure set at 20 kPa, back pressure set at 0 kPa and the small axial load F = 0.001 kN. In addition, the top and bottom pedestals were connected with water lines to an ice-bath with de-aired water at about 10 cm head. This was to ensure that the pedestals remained cold and avoid sudden axial thawing and facilitating volume deficiency compensation resulting from the conversion of pore ice into water (Sivathayalan, S and Vaid, Y, 2004). Axial deformation was measured by the external LVDT. All frozen specimens were left to thaw over 24 hours.

5.4.2 (ii) Flushing, Saturation and B-value Check

Flushing was performed after thawing to remove air from the cell drainage lines. This was done with 22°C de-aired water and by a small head difference to the top of the specimen, for about 20 minutes until no visible air bubbles could be spotted in the drainage lines.

To ensure close to full saturation of the specimen, back pressure saturation was performed. The cell pressure was increased in $\Delta 100$ kPa increments, while the back pressure increased in $\Delta 80$ kPa increments. Monitoring and fine tuning of the volume change rates on both pumps during these increments were crucial to maintain the effective stress at 20.44 ± 2.0 kPa. The increments up to target saturation value took about 1 hour for each test. Saturation was performed with cell pressure in range 600 - 950 kPa and for over twelve hours for every specimen.

Skempton's pore pressure coefficient B was used to determine the level of saturation of the specimens. B-value is the relationship between the change in pore water pressure and the change cell pressure in undrained conditions, i.e. non-active back pressure pump, see Equation (5.1). Cell pressure $\Delta\sigma_c$ between 50 - 100 kPa was used to initiate B-value check. Specimens were assumed fully saturated if $B \geq 95\%$. For lesser B-values, the cell and back pressure was increased and saturation continued for at least 3 hours.

$$B = \frac{\Delta u}{\Delta \sigma_c} \tag{5.1}$$

5.4.3 (iii) Consolidation

To recreate best estimated in-situ condition for the specimens, consolidation with mean effective stress was performed, using Equation (5.2) and parameters in Table 5.3 from Section 4.3.1 and GWL from Section 4.2.2 and Section 4.2.1

$$\sigma'_m = \frac{1}{3}(\sigma'_v + 2\sigma'_h) \tag{5.2}$$

Table 5.3: Parameters for effective mean stress.

Origin	K'_0 [-]	unit weight, γ $[kNm^3]$	GWL bgl [m]	σ'_m [kPa]
OYSB10	0.38	19	2.0	66
OYSB21	0.43	19	2.0	88

For frozen specimens from OYSB21, internal depth difference is neglected. Due to more variations in GWL at test location 1, mean effective stress was set to $\sigma'_m = 88$ kPa for specimen from OYSB10. During consolidation, axial LVDT deformation and volume change in GDS pressure/volume controller was noted. The volume change in the GDS controller during consolidation refers to the volume change in the specimen (Dawidowski and Koolen, 1987). Consolidation was considered ended when volume change $\Delta V \leq 20$ mm^3 per 5 minutes (Sandven et al., 2017) and passing NS-EN ISO 17982-9:2018(E) requirement, ϵ_{vol} rate per hour is less than 0.1 % (Standards Norway, 2018b). Consolidation was performed by either lowering the back pressure, i.e. pore pressure, or increasing the cell pressure. For all but specimen 1Cf, the cell pressure were increased to initiate mean effective stress.

5.4.4 (iv) Hydraulic Conductivity Test

After consolidation, an external hydraulic conductivity test rig was connected to the specimen as seen by simplified sketch in Figure 5.14. An external water pump, same type as used for both back and cell pressure, marked "HP" in the sketch was connected to the system. A second differential pressure transducer marked with pink color was also connected in the loop.

The external pump HP and second differential pressure transducer was employed with measurement setups, were constant head was induced by:

Volume ramp setup: HP pushed in an exact volume of de-aired water at a set rate over a specified time period. ΔPore pressure stabilized at an interpreted constant head.

Target pressure setup: HP worked with feedback from the second differential pressure transducer, pushing in de-aired water to maintain a specified set target pressure, i.e. Δpore pressure, in kPa.

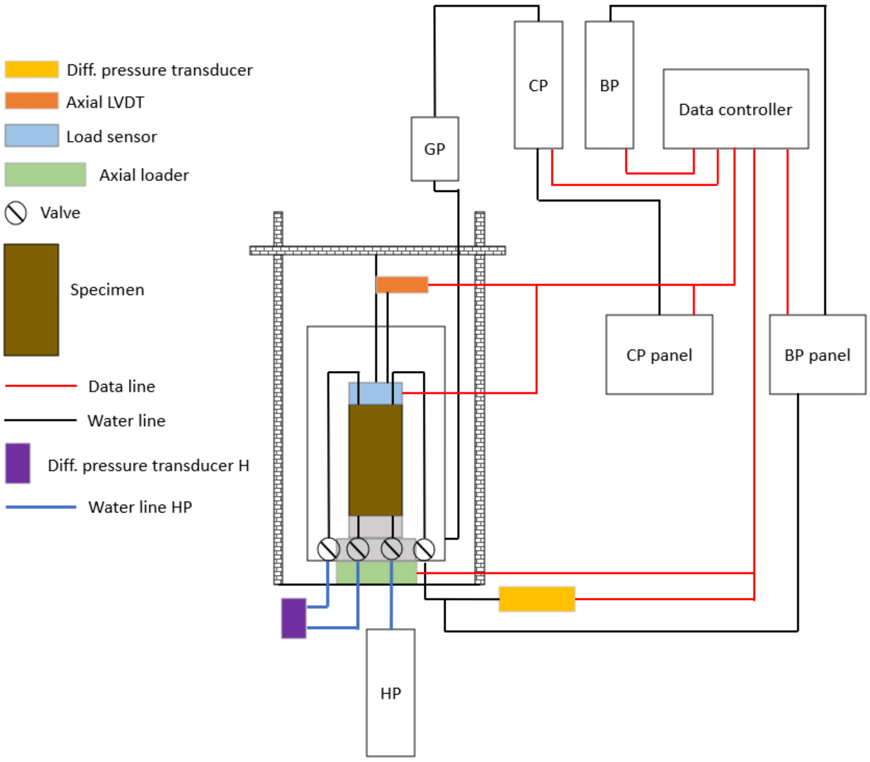

Figure 5.14: Simplified model of triaxial setup used during Hydraulic conductivity tests. HP = water pump for water pressure, i.e. head.

Both measurement setups was used to calculate the hydraulic conductivity of the frozen specimens, using Section 3.9 and Equation (3.20). Only target pressure setup was used for test 1 C. Δtime and Δvolume in specimen was noted from both systems and used for calculations, where Δvolume is the amount of water going as inflow or outflow in the test measured by the GDS controllers.

Height was adjusted to axial deformation under the previous stages. Area of the specimen was adjusted for known volume change during consolidation. The flow conditions during target pressure method were interpreted by the inflow and outflow rate relationship, i.e. inflow/outflow, which was deemed acceptable if $0.75 \leq$ inflow/outflow ≤ 1.25 after NS-EN ISO 17892-11:2019(E) (Standards Norway, 2019).

Variations in volume ramp or target pressure, i.e. variations in gradient, was used to check the variability of the hydraulic conductivity determinations and to ensure that correct hydraulic gradient was initiated.

5.4.5 (v) Dismounting

Dismounting was done after hydraulic conductivity tests. The membrane was carefully removed and pictures of intact and split specimens were taken. Porous discs and membrane was flushed with deaired water into a tray with the specimen to capture all of the specimen mass, before being placed in a 105°C oven to get water content. The porous discs were thoroughly washed and cleaned before being re-used on next specimen.

Grain size distribution test was performed after oven treatment. GSD was performed not by the author of this thesis, but by NGI laboratory personnel.

Chapter 6

Results from Field Tests

This chapter presents the measured results and interpretations of field tests. A conclusion for each field test is included underneath measured results and interpretations.

6.1 Measured and Interpret Results

Measured parameters used for calculation of estimated hydraulic conductivity for field equipment is shown in Table 6.1. Measured pore pressure and atmospheric pressure for Flow Cone are converted from unit bar to kPa.

Table 6.1: Measured parameters from field tests.

Equipment	Used parameters
Flow Cone	Pore pressure at filter, $u_{f,m}$ [kPa]
	Atmospheric pressure, atm [kPa]
CPTU	Cone resistance, q_c [kPa]
	Sleeve friction, f_s [kPa]
	Pore pressure behind cone, u_2 [kPa]
	Depth bgl, z [m]
Both	Timestamp
HPT	Depth bgl, z [m]
	Timestamp
	EC [mS/m]
	HPT Flow avg. [mL/min]
	HPT Pressure avg. [kPa]
	Atmospheric pressure, atm [kPa]
	HPT Line pressure [kPa]
	Penetration speed [mm/sec]
Falling head	Timestamp
	Atmospheric pressure, atm [kPa]
	Water level [m]
	Temperature [°C]
	Depth bgl, z [m]

6.2 Flow Cone and CPTU at OYSC68

Estimated hydraulic conductivity was determined using Section 3.6, Section 3.5 and Section 3.8 for CPTU and Flow Cone results in following sections. A spreadsheet, version CPTu v.2021.01, made by the Norwegian Public Roads Administration (NPRA) was used for soil classification and calculation of SBTi from Section 3.8. The estimation of hydraulic conductivity from the SBT index is done using Equation (3.17) and Equation (3.18).

6.2.1 CPTU Results OYSC68

Figure 6.1 shows CPTU results and estimated hydraulic conductivity K from position OYSC68 during Flow Cone run. Corrected cone resistance q_t shows the same resistance as old OYSC20 CPTU test in Figure 4.9. Estimated K below 6.80 m depth is generally between 10E-08 and 10E-07, while above 6.80 m it ranges from 10E-05 and 10E-04. This is inline with the soil classification and cone resistance, as between 6.0 - 6.5 m depth, these indicate coarser material.

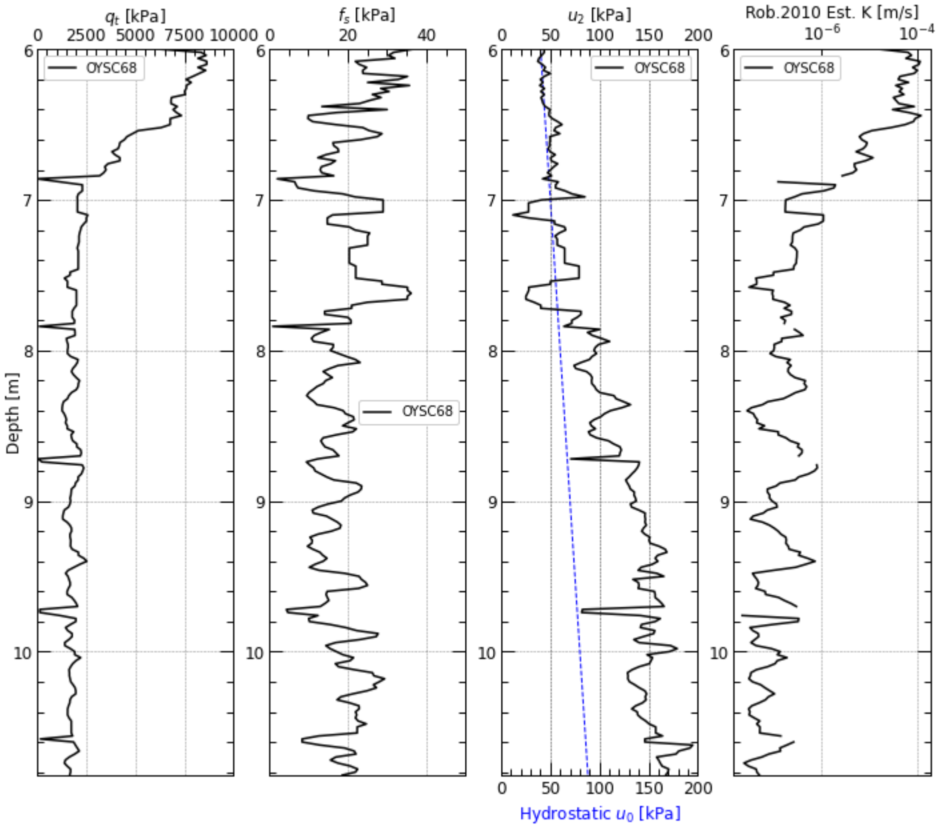

Figure 6.1: CPTU results from Flow Cone test at OYSC68.

Dissipation test was performed at 8.73 m depth while Flow Cone testing was performed. The measured pore pressure u_2 dissipated towards assumed hydrostatic pressure at 2.0 m GWL, blue line in Figure 6.1. Unfortunately, no dissipation test at 10.83 m dept, last Flow Cone testing depth, was performed as CPTU logging was terminated upon reaching goal depth.

The soil classification viewed in Figure 6.2 shows mostly silty sand or silty clays. This agrees with the soil content in Appendix B and soil classification by OYSC20 in Appendix C for test location 2.

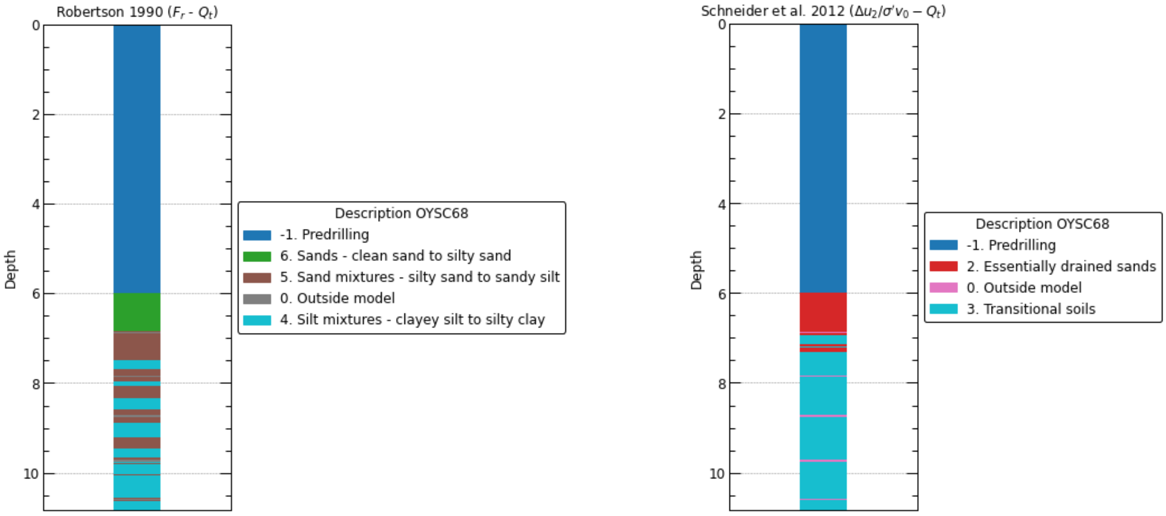

(a) Soil classification Robertson 1990. **(b)** Soil classification Schneider et al. 2012.

Figure 6.2: OYSC68 soil classification.

6.2.2 Head Loss Test for System Resistance

System resistance test was performed using setup viewed in Figure 6.3. FCHM1 was lowered in the HPT reference tube and filled with water. Vertical distance from top tube, i.e. top water pressure level, to sensor location at control module was 57.3 cm.

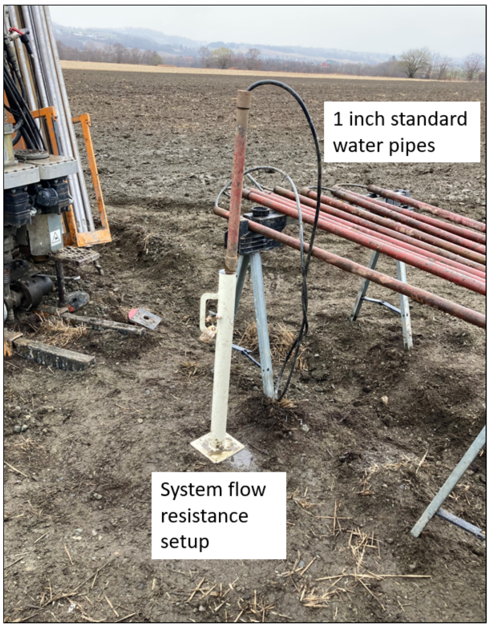

Figure 6.3: Used setup for system resistance test.

Results and complete measurement run from system resistance test is shown in Figure 6.4. The head loss $H_l = u_{f,m} - atm_{local}$ is corrected by setting local atmospheric datum at top reference tube, i.e. atm_{local}. Head loss is therefore the pressure needed to upkeep the set constant flow rate Q, i.e. flowing water out of the top of the tube. The negative value in the complete run, red line plot, is due to cylinder refill of de-aired water. The system pressure sensor monitors also the pressure used to refill the cylinder within the pump.

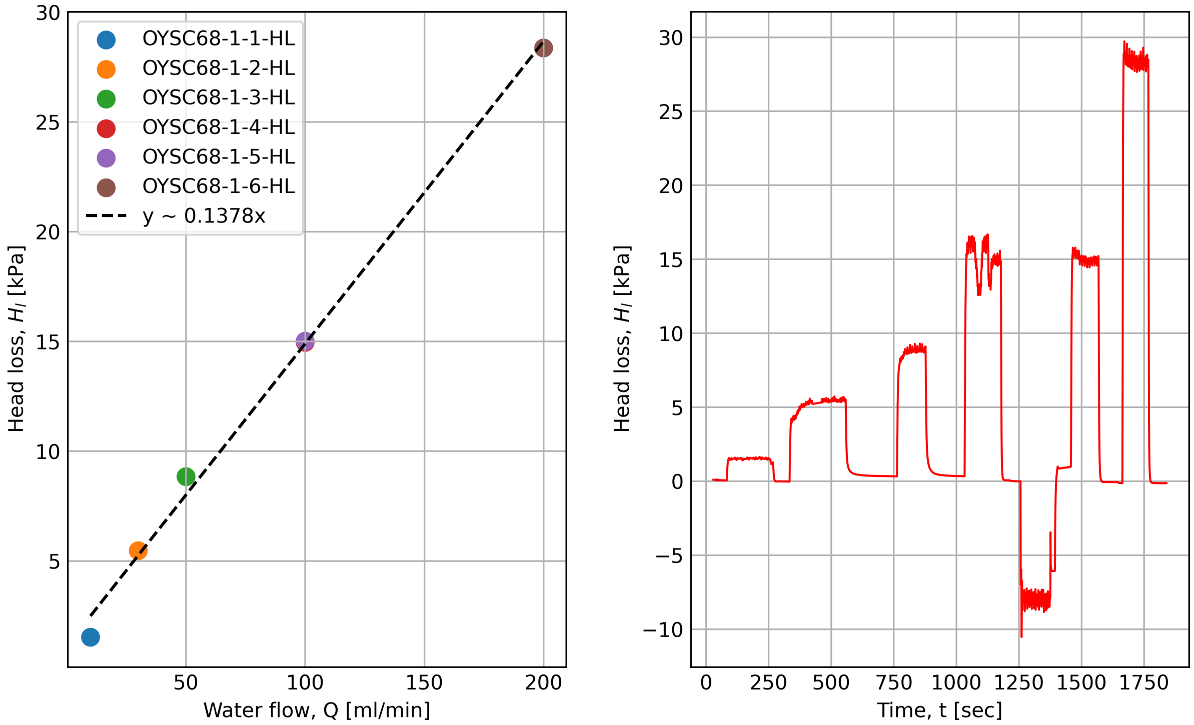

Figure 6.4: Results from system resistance test using FCHM1 for Flow Cone.

Some seconds after initiating constant flow rate Q, the pressure stabilized and the average H_l was derived from the stable pressure plateau. For test OYSC68-1-4-HL, the pressure plateau varies more than the rest. This is due to movement in the reference tube during test, to see the reaction in the live measurement and that the system was working. A linear regression of the average head loss H_l points resulted in very good fit, as seen by the coefficient of determination R^2 in Table 6.2. Slope of the linear regression line is hereby used to give the corrected pore pressure u_f in following stationary flow tests, as seen in Equation (6.1). Intercept value in Table 6.2 is assumed to be system resistance when no flow is initiated. This corrects all values besides when flow is activated.

$$u_f = u_{f,m} - 0.1378 \cdot Q \tag{6.1}$$

Table 6.2: System resistance flow and result.

Test ID	Water flow, Q [ml/min]	Avg. Head Loss [kPa]
OYSC68-1-1-HL	10	1.52
OYSC68-1-2-HL	30	5.46
OYSC68-1-3-HL	50	8.84
OYSC68-1-4-HL	100	14.96
OYSC68-1-5-HL	100	15.01
OYSC68-1-6-HL	200	28.37
R^2 [-]	0.9960	
Intercept [kPa]	1.1112	

6.2.3 Stationary Phase Results for Flow Cone at OYSC68

Executed stationary phase tests at depth 7.9 m is shown in Table 6.3, while results of corrected pore pressure u_f with interpreted dissipation pressure u_0 is shown in Figure 6.5. Initially and after every flow test, pore pressure u_f dissipated towards pressure u_0, which back-calculated to GWL at 2.112 m depth. Pressure u_f is initially lower than u_0 for high values of flow rate Q, as seen by u_f starting below u_0 before rising upwards towards pressure plateau. This is due to time lag in the system, i.e. that the pump uses a second to initiate flow and correction factor applied immediately at start flow.

Table 6.3: Stationary flow cone tests at 7.9 m depth.

Test ID	Flow rate, Q [ml/min]
OYSC68-1-1	10
OYSC68-1-2	20
OYSC68-1-3	40
OYSC68-1-4	50
OYSC68-1-5	40
OYSC68-1-6	20

OYSC68-1-1 and OYSC68-1-2 with flow rates 10 and 20 ml/min shows tendency to parabolic stabilization of u_f with time at pressures about 100 and 128 kPa. This results in $\Delta u = u_f - u_0$ of almost 43 and 65 kPa. These test were ended when as the change Δu_f became small. For OYSC68-1-1 $\Delta u_f = 0.26$ kPa for the last 40 sec, while for OYSC68-1-2 $\Delta u_f = 1.04$ kPa for the last 40 sec.

OYSC68-1-3 with flow rate 40 ml/min stabilize fast at a pressure plateau at about Δu 88 kPa. But this seems to have fractured the soil or migrated grains and created flow channels since the following test, OYSC68-1-4 with higher flow rate, doesn't reach the same Δu value, and stabilize at a much lower pressure. The following tests shares the same tendency, stabilizing on a much lower pressure plateau than previous test with same flow rate.

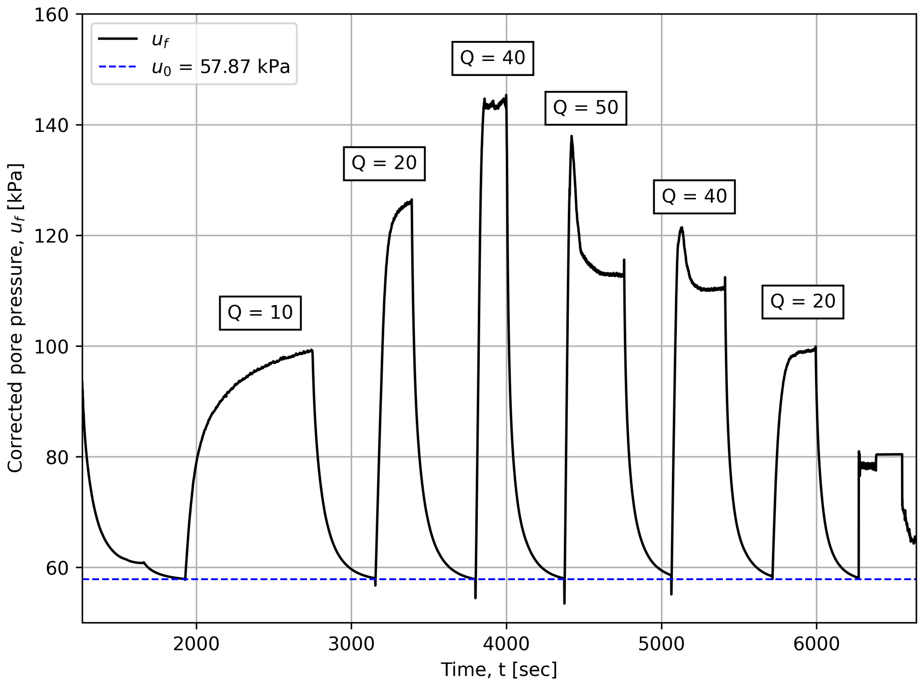

Figure 6.5: Corrected pore pressure for OYSC68-1 stationary phase testing at 7.9 m mid filter depth.

Stationary tests performed at 10.0 m depth is shown in Table 6.4 and Figure 6.6. The same range of flow rates, except 10 ml/min, were also tested at 10.0 m depth. From dissipation before and after each test, u_0 was back-calculated to fit GWL at 1.986 m.

Table 6.4: Stationary flow cone tests at 10.0 m depth.

Test ID	Flow rate, Q [ml/min]
OYSC68-2-1	20
OYSC68-2-2	30
OYSC68-2-3	40
OYSC68-2-4	50
OYSC68-2-5	40
OYSC68-2-6	30

Unfortunately, the initial test OYSC68-2-1 seems to have created the same fracture in the surrounding soil fabric at 10.0 m as OYSC68-1-3 did at depth 7.9 m, as it rises fast to a high pressure Δu and then stabilize at a lower pressure plateau. Similar pattern is created by the following tests, even when the flow rate is increased, the initial Δu of the first test is never reached again.

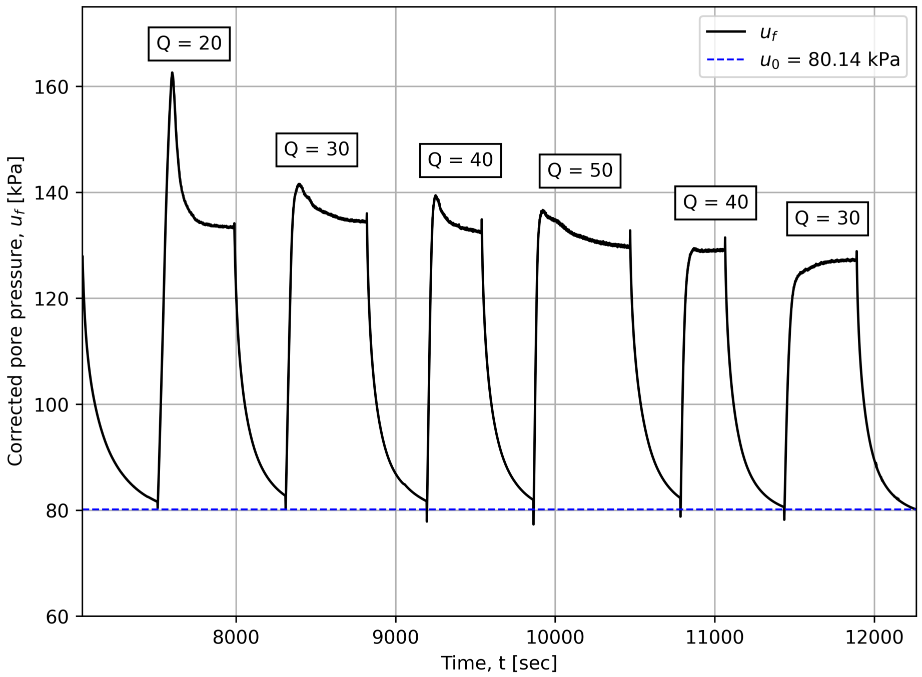

Figure 6.6: Corrected pore pressure for OYSC68-2 stationary phase testing at 10.0 m mid filter depth.

6.2.4 Flow Cone Constant Rate Interpretation

From the stable pressure plateau or the stabilized, consistent pressure of end time period on the parabolic pressure inclination, steady state for the constant flow rate test is assumed reached and the pressure head H in Equation (6.2) is interpret by the best average value of u_f. Pressure head H is plotted with flow rate to examine the pattern and behaviour of the interpreted pressure heads. Hydraulic conductivity is calculated using Equation (3.7). For FCHM1, the dimensions of the filter mentioned in Section 3.1 was used to calculate the shape factor by Equation (3.5), which resulted in C equal to 0.4157 m used for calculation of hydraulic conductivity by Flow Cone tests. This shape factor accounts for only horizontal flow, as determined by the filter of FCHM1.

$$H = u_f - u_0 \tag{6.2}$$

For OYSC68-1 at depth 7.9 m, an acceptable fit of linear relationship between the first two tests is found in Figure 6.7, see coefficient of determination in Table 6.5. This indicates a laminar flow response in soil. The first two tests that are part of the linear regression analysis is symbolized with circles. The slope m of the regression line was used to calculate the hydraulic conductivity, after Equation (6.3).

$$K = \frac{m}{C} \tag{6.3}$$

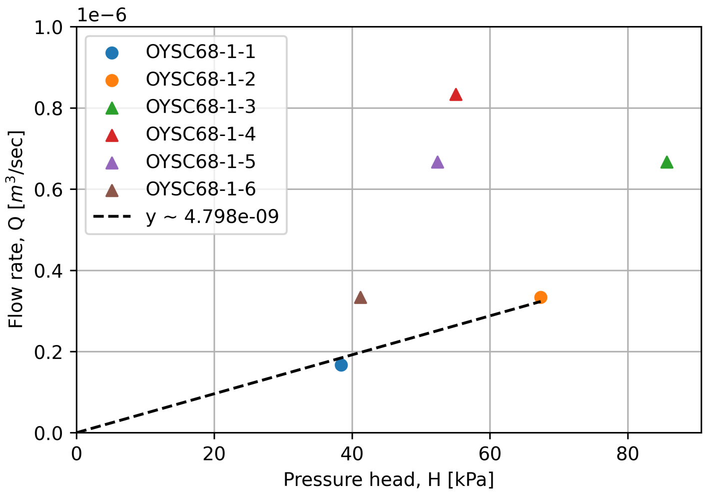

Figure 6.7: Best average pressure heads versus flow for stationary Flow Cone tests at 7.9 m depth.

The difference in pressure head for tests with same flow rate is clearly shown in Figure 6.7. This suggest that there has been a migration of fine grains within the surrounding soil fabric, changing the initial conditions of the test and resulting in hydraulic conductivity for a altered soil layer or created a fracture in the soil. The last test with same flow rate as second test, shows about 40 % reduction in pressure head. The chosen flow rates gave pressure head which overcome the effective horizontal stress and being dangerously close to overcome effective vertical stress, as shown in Table 6.5, leading to radial extension and effective radial stress reduced to zero in the confined soil around the filter, creating a vertical crack. The radius of these effects are unknown. Horizontal effective stress is surpassed for one out of two of the initial tests, were assumed laminar flow conditions has occurred. Since the ratio H/σ'_v of OYSC68-1-3 surpasses recommendations by (Bjerrum et al., 1972), assuming soil layer at 7.9 m is of medium compressibility and driven method of installation, it is believable that OYSC68-1-3 induced a hydraulic fracture in the soil, creating a vertical crack that re-opened after dissipation for the next tests. Parameters from Section 4.3.1 was used to calculate effective stresses.

Hydraulic conductivity is nevertheless calculated for all tests, using Equation (6.4) and converting pressure head from unit kPa to unit mH2O, for comparison to the assumed established laminar flow, named LinReg in Table 6.5. Values are not far off each other, with the assumed laminar flow being in the lower range of the total averaged conductivity. The hydraulic conductivity of LinReg, 1.15E-07, is chosen as representative for this test depth.

$$K = \frac{Q}{CH} \tag{6.4}$$

Table 6.5: Calculated hydraulic conductivity, K for tests at depth 7.9 m.

Test ID	K [m/s]	R^2 [-]	H/σ'_v [-]	H/σ'_h [-]
OYSC68-1-1	1.043E-07	-	0.42	0.84
OYSC68-1-2	1.190E-07	-	0.74	1.48
OYSC68-1-3	1.872E-07	-	0.94	1.88
OYSC68-1-4	3.641E-07	-	0.60	1.21
OYSC68-1-5	3.061E-07	-	0.58	1.15
OYSC68-1-6	1.946E-07	-	0.45	0.90
LinReg	1.154E-07	0.9970	-	-

Figure 6.8 shows results of best average pressure heads H versus flow rate for tests at depth 10.0 m. Initially OYSC68-2-1 reaches a maximum pressure head of H = 82.45 kPa, as seen in Figure 6.6, before falling down and stabilizing at about 54 kPa in the pressure plateau. The maximum pressure results in a H/σ'_v ratio of 0.75 and H/σ'_h ratio of 1.97, as seen within parentheses in Table 6.6. These ratios along with the response of the later tests at higher flow rates, implies that a hydraulic fracture unfortunately also has occurred for test depth 10.0 m. Due to this, no linear relationship is proposed for the resulting pressure heads in Figure 6.8.

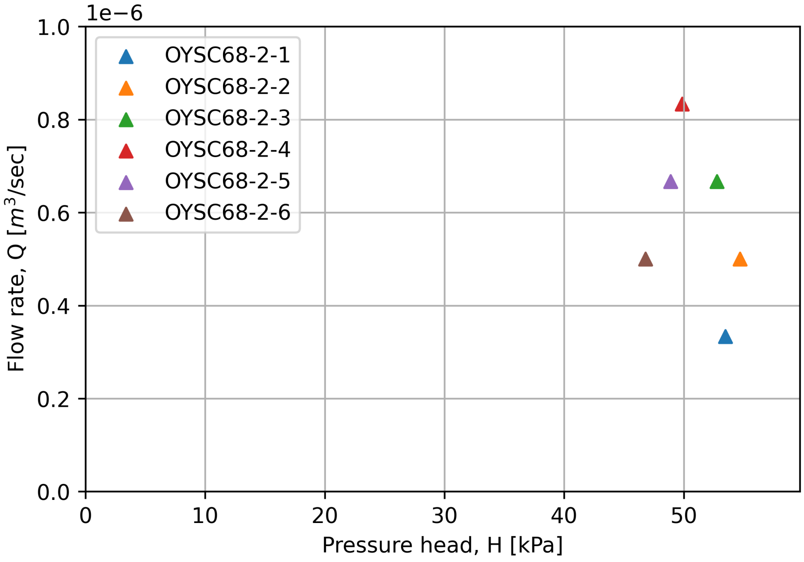

Figure 6.8: Best average pressure heads versus flow for stationary Flow Cone tests at 10.0 m depth.

As the flow rate is increased, the pressure heads of the tests results in values within 50.0 ± 5 kPa range. This implies a channeled, laminar water flow in the surrounding soil, as the pressure behaves relative stable with different flow rates. The calculated hydraulic conductivity's using Equation (6.4) in Table 6.6 is assumed to be the hydraulic conductivity of this channeled, fractured soil. Because of Equation (6.4), while the pressure head stays within the same range, the higher the flow rate, the higher the hydraulic conductivity, leading to non-reliable results.

Table 6.6: Calculated hydraulic conductivity, K for tests at depth 10.0 m.

Test ID	K [m/s]	H/σ'_v [-]	H/σ'_h [-]
OYSC68-2-1	1.500E-07	0.49 (0.75)	1.28 (1.97)
OYSC68-2-2	2.199E-07	0.50	1.31
OYSC68-2-3	3.040E-07	0.48	1.26
OYSC68-2-4	4.021E-07	0.45	1.19
OYSC68-2-5	3.281E-07	0.44	1.17
OYSC68-2-6	2.570E-07	0.43	1.12

The hydraulic fracture occurred at 20 ml/min for tests at 10.0 m depth, while at 40 ml/min for test depth 7.9 m and at a lower ratio of H/σ'_v, confirming the soil content in Appendix B and the lower K'_0 from Section 4.3.1, implying a soil layer with higher compressibility and void ratio.

6.2.5 Flow Cone Dissipation Interpretation

The dissipation of corrected pore pressure $u_f = \Delta u$ after each test in Figure 6.5 and Figure 6.6 is interpret using Section 3.6. The corrected pore pressure is initiated by previous constant flow rate tests, but is interpret as a Δu for the surrounding soil at the end of each flow rate test.

Previous triaxial bender element tests of specimens from Øysand is from position OYSB09, see Figure 5.1, at test location 1. Unfortunately, no available tests with calculated initial shear modulus G_{max} is available for test location 2. By comparing GSDC from frozen specimens from OYSB21 at test location 2, see Appendix E, with GSDC of previous triaxial bender element tests from test location 1, see Appendix D, G_{max} was chosen from test with best GSD fit. Therefore, the calculated rigidity index I_r is at best a rough estimation. Results in Table 6.7 by using Equation (3.19) was used to estimate the in-situ horizontal coefficient of consolidation c_h for dissipation tests in following sections. In-situ stress parameters was calculated using Section 4.3.1.

Table 6.7: Approximated rigidity index for dissipation tests

Depth CPTU [m]	G_{max} [MPa]	q_t [kPa]	I_r [-]
7.9	52.8	1937.139	112.52
10	52.8	1924.74	109.76

OYSC68-1 at 7.9 m Depth

Figure 6.9 shows the normalized excess pore pressure U versus time and time factor T^* for dissipation of tests at depth 7.9 m. Degree of consolidation with time factor T^* from Teh and Houlsby, 1991 is included for comparison. The estimated coefficients of horizontal consolidation c_h along with interpret t_{50} is presented in Table 6.8.

Normalized excess pore pressure U show some internal variation, where OYSC68-1-3 deviates most from the average result. There is big internal variation in estimated c_h.

Table 6.8: Results for Flow Cone dissipation at 7.9 m depth

Test ID	t_{50} [sec]	c_h [m^2/year]
OYSC68-1-1	39.218	4219.021
OYSC68-1-2	23.609	7008.41
OYSC68-1-3	17.224	9606.454
OYSC68-1-4	19.827	8345.265
OYSC68-1-5	18.846	8779.665
OYSC68-1-6	23.467	7050.819

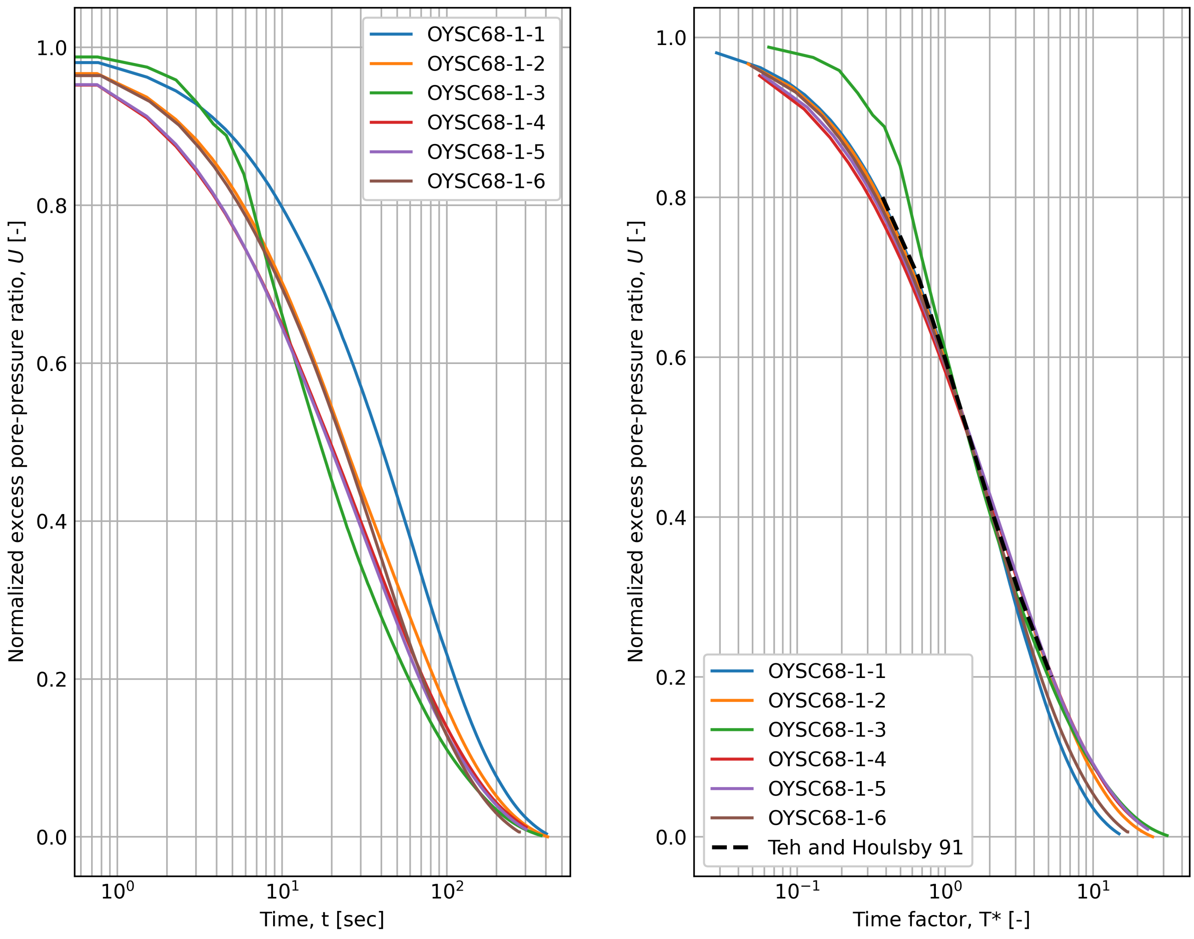

Figure 6.9: Dissipated excess pore pressure and versus time and time factor T* for Flow Cone at depth 7.9 m.

OYSC68-2 at 10.0 m Depth

Dissipation of tests at 10.0 m depth exhibit very similar behaviour, as shown in Figure 6.10. This results in Table 6.9 show some internal variation.

Table 6.9: Results for Flow Cone dissipation at 10.0 m depth

Test ID	t_{50} [sec]	c_h [m^2/year]
OYSC68-2-1	38.116	4287.388
OYSC68-2-2	33.104	4936.506
OYSC68-2-3	34.116	4790.072
OYSC68-2-4	40.005	4084.942
OYSC68-2-5	33.379	4895.835
OYSC68-2-6	31.702	5154.820

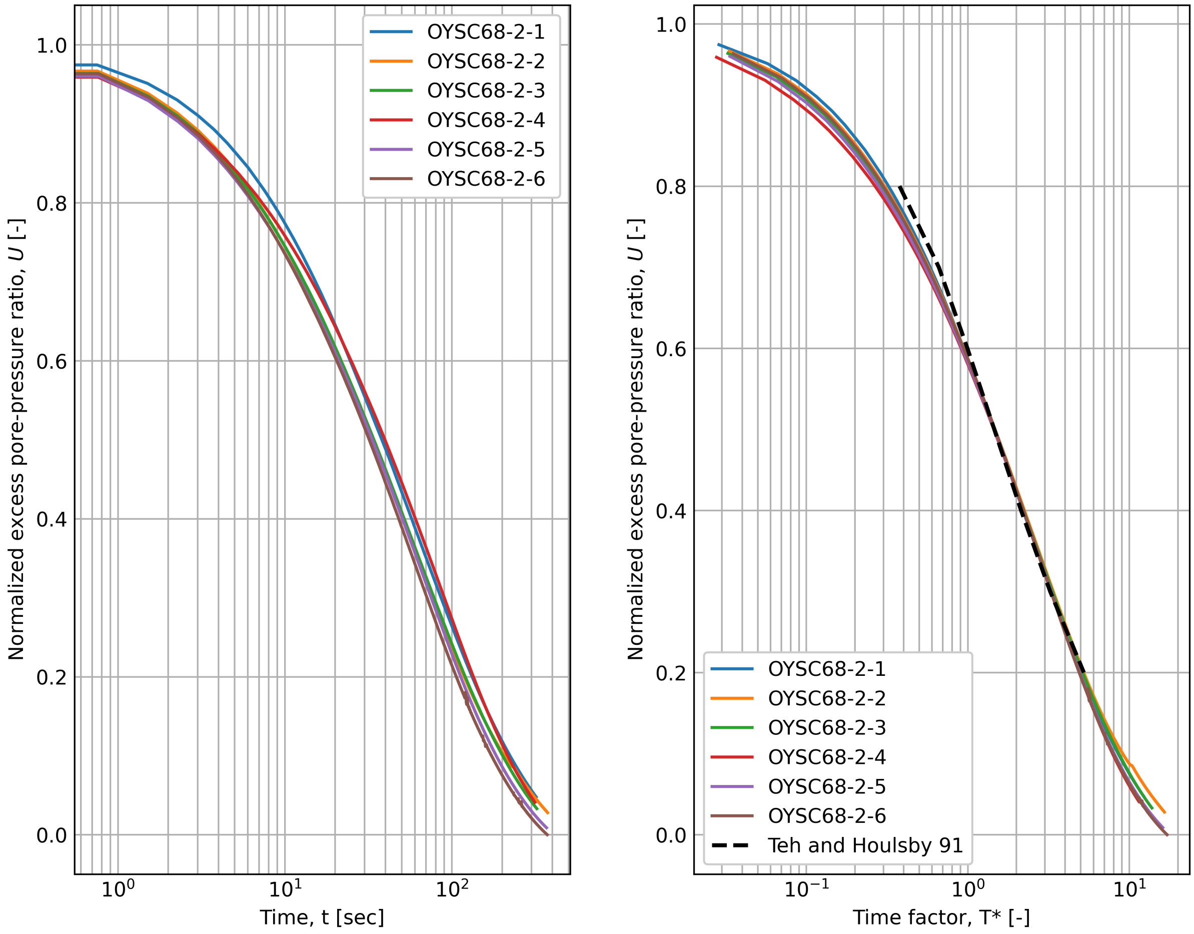

Figure 6.10: Dissipated excess pore pressure and versus time and time factor T* for Flow Cone at depth 10.0 m.

6.2.6 Conclusion Flow Cone and CPTU at Position OYSC68

Estimating Ground Water Level

Both CPTU and Flow Cone tests show plausible and good results from back-calculation of measured pore pressure compared to determined ground water level in Section 4.2.2. The results are shown in Table 6.10.

Table 6.10: Back-calculated GWL at position OYSC68 from dissipation of CPTU and Flow Cone.

Test	GWL, bgl [m]
CPTU, u_2	2.0
OYSC68-1, u_f	2.112
OYSC68-2, u_f	1.986

Estimated Hydraulic Conductivity from Constant Rate Interpretation

Most results from constant rate interpretation in Section 6.2.4 was unfortunately disturbed by high pore pressure heads Δu, resulting in assumed hydraulic fracturing of the surrounding soil close to the filter. The results is therefore considered with caution and only the first two tests at 7.9 m test depth is deemed credible. Hydraulic conductivity calculated from the linear slope in Figure 6.7 is chosen to represent K at 7.9 m depth.

By assuming that test OYSC68-2-1 stabilized at maximum pressure ratio $\Delta u/\sigma'_v = 0.75$ and did not induce a hydraulic fracture, the resulting estimated conductivity is presented in Table 6.11 assuming 20 ml/min flow rate.

Since the compressibility is assumed higher for the soil at layer 10.0 m than for 7.9 m, backed up by soil content graph in Appendix B and the lower pore pressure versus effective stress ratio at assumed hydraulic fracture failure, a bottom limit can be set. By assuming that the lowest stable flow rate of Flow Cone can be set at 1.0 ml/min, 5 ml/min as penetration flow has previously been tested (A. Gundersen et al., 2022), and using the maximum pressure ratio set at one decimal lower $\Delta u/\sigma'_v = 0.74$, the bottom limit for estimation of hydraulic conductivity can be set to 4.926E-09 m/s. This is in the range of hydraulic conductivity for fine grained material, clays (Janbu, 1989). It can therefore be assumed that the hydraulic conductivity for soil at layer 10.0 m is between 4.926E-09 to 1.154E-07, where the highest value is the result from 7.9 m depth.

Overall the result for estimated K using soil behavior type index I_c in Figure 6.1 and Table 6.11 is within the same range as K from constant rate method for Flow Cone.

Table 6.11: Estimated hydraulic conductivity at position OYSC68

Test	Est. K [m/s]	
-	Depth 7.9 m	Depth 10.0 m
CPTU	4.069E-07	8.83771E-08
Flow Cone	1.154E-07	9.725E-08* (4.926E-09 - 1.154E-07)**

*Assumed with flow rate 20 ml/min and $\Delta u/\sigma'_v = 0.75$
** Theoretical range

Dissipation and Estimated Coefficient of Horizontal Consolidation

The normalized excess pore pressure U versus time factor T^* for dissipation of $u_f = \delta u$ at depths 7.9 and 10.0 m in Figure 6.9 and Figure 6.10 show overall good fit between values of 0.8 to 0.2 % compared to the theoretic degree of consolidation at position 10 radii above cone shoulder from (Teh and Houlsby, 1991). But this is expected because of calculation method in Equation (3.11), they are destined a good fit because of chosen value T_{50}. The Δu dissipation will be influenced by the soil deformation during the constant flow rate tests, as these indicate hydraulic fracture, and its starting point $\Delta u(t = 0)$. From Equation (3.9), it is assumed that the extent of the plastic zone is determined by $a\sqrt{I_r}$ (Teh and Houlsby, 1991).

The estimated coefficients of horizontal consolidation in Table 6.8 show large internal variation due to internal difference in max Δu, i.e. starting point for dissipation of excess pore pressure, from Figure 6.5. Estimated c_h from 10.0 m depth in Table 6.9 show less variation than results from 7.9m depth, but this is because starting point Δu is more similar in the different test, as seen in Figure 6.6.

Results show that variation in estimated c_h is prominent and overall high compared to other silt sites in Trøndelag region (Bihs, Long, Nordal and Paniagua, 2021), which has comparable GSD and corrected cone resistance q_t. The dissipation time is also considerably lower. This implies that the estimated c_h is from dissipation of a highly disturbed zone of soil with big volumetric change around the Flow Cone filter.

6.3 HPT

Each HPT test run is presented in the following sections and figures. There is a slight delay to the depth measurement, EC readings and the average HPT pressure, due to distance between the tip of the probe and the outlet injection port and EC Wenner array during live run. This is corrected for in the post-data software DI Viewer, so the average HPT pressure and EC measurements is at its original depth measurement, not with delay, in following figures. Measured data retrieved from the pre-drilled depth is extracted and only data from undisturbed depth is presented.

Firstly the measured results and estimated hydraulic conductivity using included empirical model in DI Viewer software, see Section 3.7.2, is presented. Secondly and thirdly, the other models for estimation of K is presented.

6.3.1 OYSC64 with MC Approach

Results from dissipation tests conducted at OYSC64 are presented in Figure 6.11. The static pressure reveal close to hydrostatic groundwater pressure distribution with depth from linear regression analysis, but the deepest test, OYSC64-5, deviates from the bgl static water level back-calculation. This indicates either a less permeable layer, and that the dissipation test should have been run longer, or a small confined zone with higher groundwater pressure. By examining the dissipation run, the pressure decreased only 0.07 kPa during the last 100 seconds, but fine grained materials can use long time to dissipate excess pore pressure. The difference in groundwater pressure based on GWL at 2.350 m depth versus 2.520 is only 1.70 kPa. Therefore, the impact of the static water level of OYSC64-5 is small considering the estimated hydraulic conductivity, because the red piezometric line in Figure 6.12 would only have a small change of 1.7 kPa.

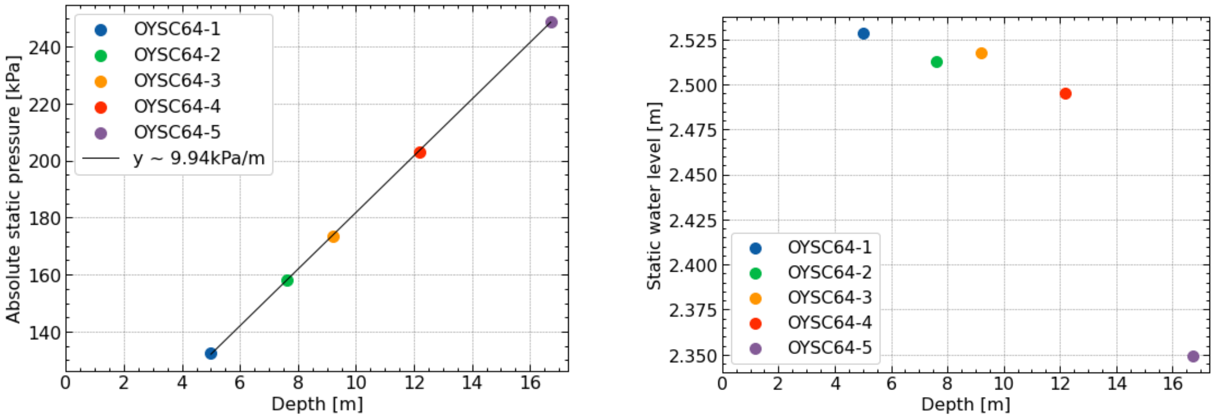

(a) OYSC64 bgl dissipation pressure results

(b) OYSC64 bgl static water level results

Figure 6.11: OYSC64 dissipation test results

Results from penetration phase is shown in Figure 6.12. Low EC and low average HPT pressure between 5.0-12.5 m depth indicate a more permeable, sandy material with estimated hydraulic conductivity around $(2.0 \pm 1.0) \times 10^{-4}$ m/s, but with thin layers of more impermeable material.

Around 13 m depth, the average HPT pressure rises, but with only a relative very small increase in EC. As a result of the HPT pressure, the estimated K drops below the calculation model limit.

Below 14 m depth, the EC rises fast and the pressure is generally high, with some deviations. Est. K is mostly low or below the model limit.

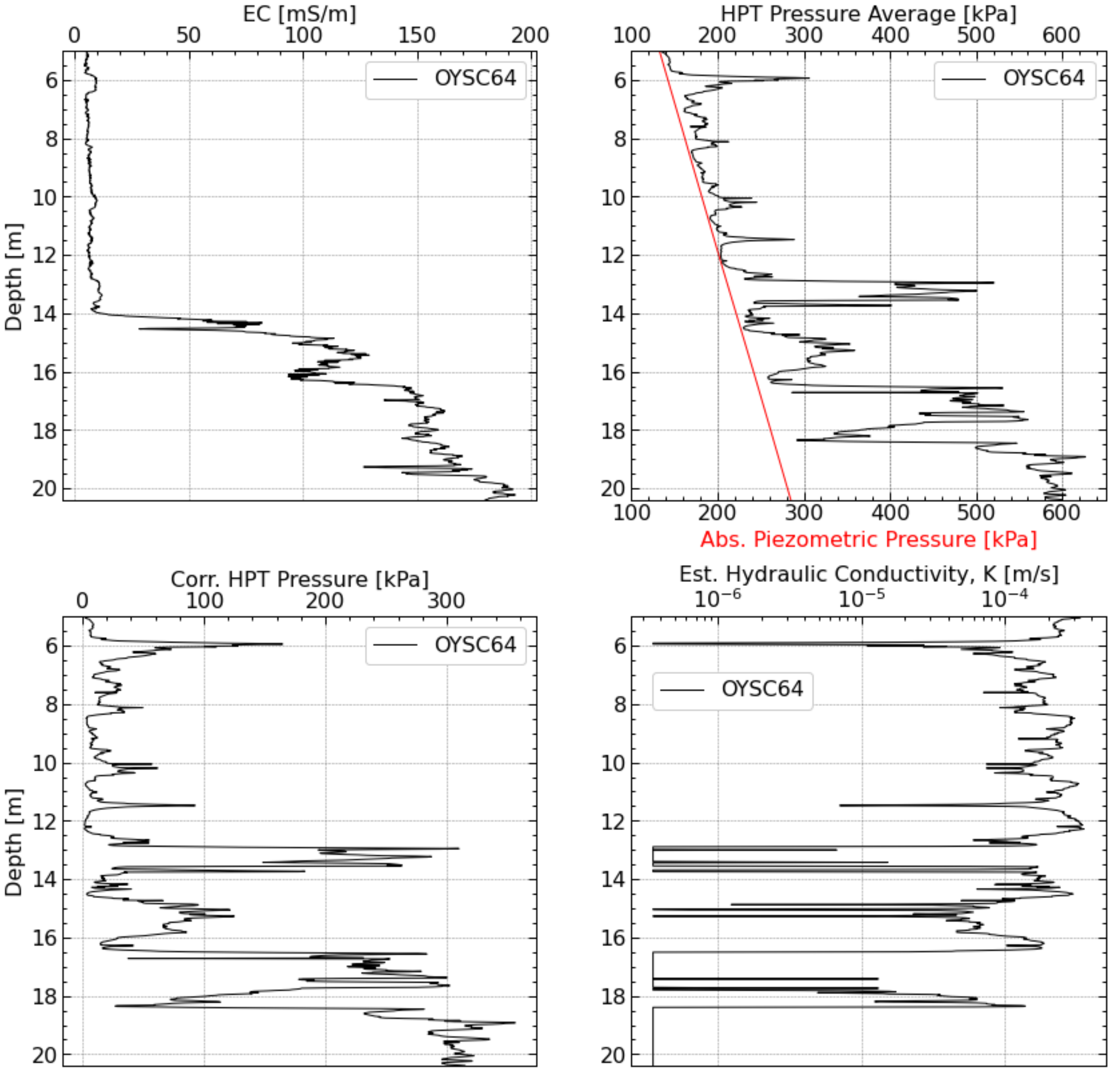

Figure 6.12: Penetration results from OYSC64

6.3.2 OYSC66 with MC Approach

Figure 6.13 show results from dissipation tests conducted at OYSC66. The results show very close similarity in the bgl static water level back-calculation. The linear regression analysis of groundwater pressure distribution deviates some from hydrostatic pressure distribution, but gives a negligible difference to further calculations of estimated hydraulic conductivity because of the relative small depth range, when compared to a hydrostatic distribution.

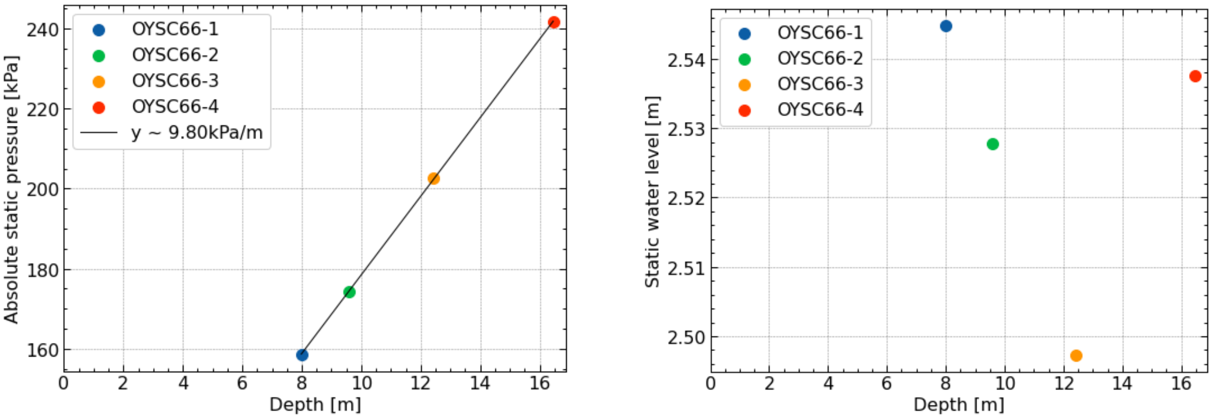

(a) OYSC66 bgl dissipation pressure results **(b)** OYSC66 bgl static water level results

Figure 6.13: OYSC66 dissipation test results

Penetration phase results for OYSC66 is presented in Figure 6.14. Low EC and average HPT pressure between 5-14 m depth results in an estimated hydraulic conductivity stable around $(2.0 \pm 1.0) \times 10^{-4}$ m/s. The average HPT pressure follows the piezometric pressure closely and is relatively stable until 14 m depth, were EC rises. Below 14 m depth, the average HPT pressure shows more variation, in tune with higher EC. This results in more variation of estimated K.

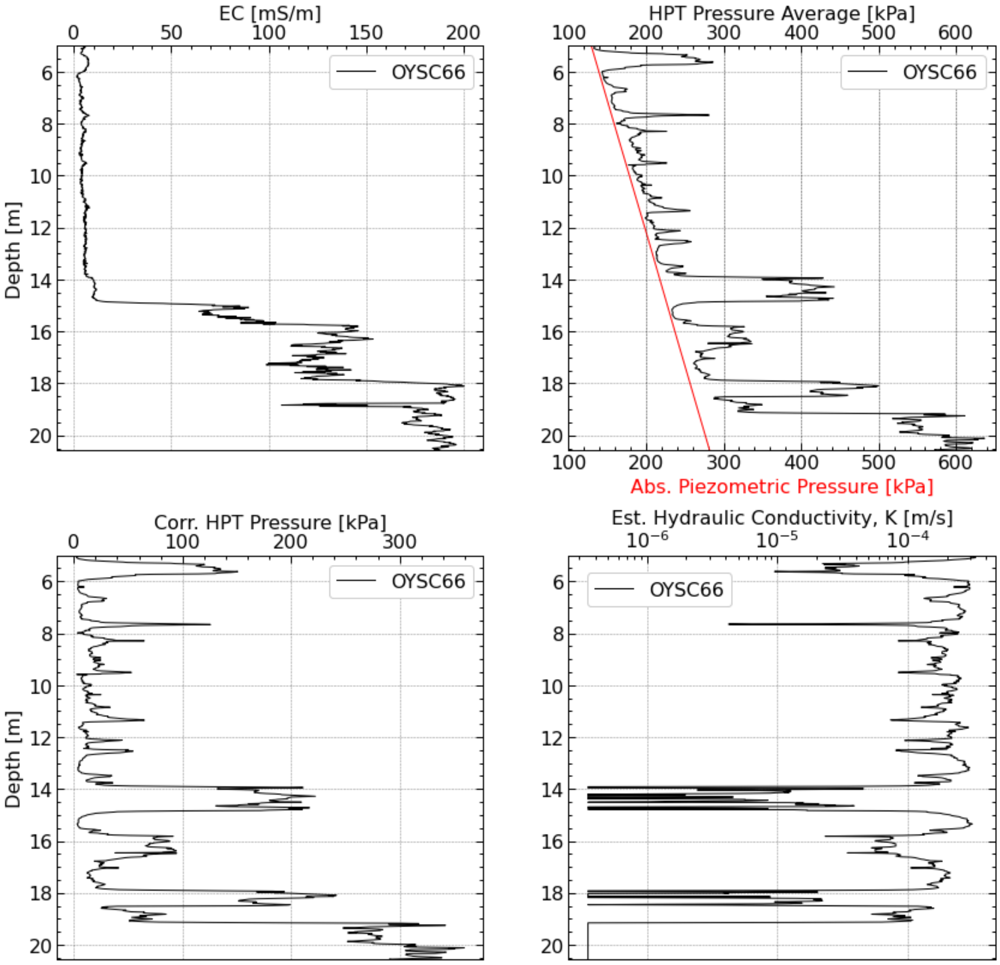

Figure 6.14: Penetration results from OYSC66

6.3.3 OYSC67 with MC Approach

Results from dissipation tests at OYSC67 is shown inFigure 6.15. OYSC67 shows close to hydrostatic groundwater pressure distribution with depth, but more variety in results from the static water level back-calculation. The deepest test, OYSC67-4, decreased 0.63 kPa in pressure during the last 100 seconds of the dissipation, which indicates that the dissipation towards ground water pressure was not finished. This is deemed negligible for the calculation of the HPT average pressure.

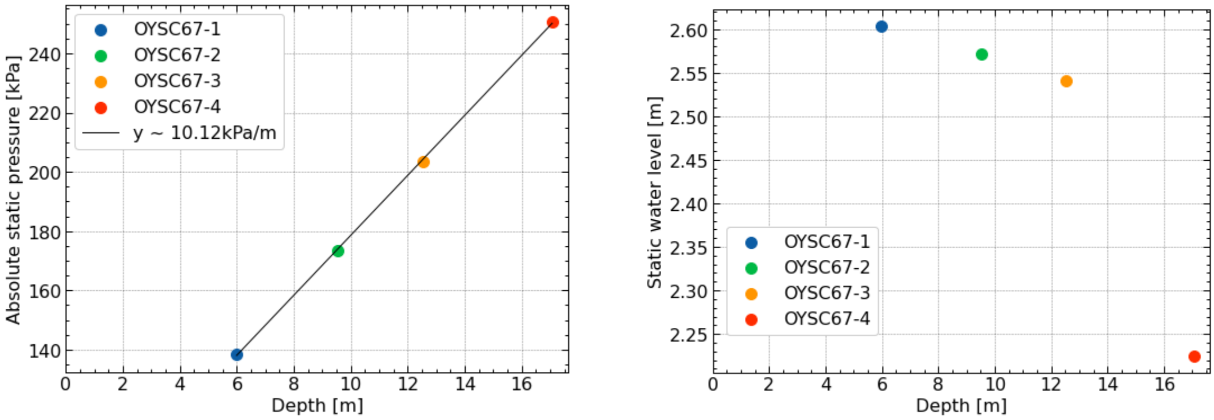

(a) OYSC67 bgl dissipation pressure results **(b)** OYSC67 bgl static water level results

Figure 6.15: OYSC67 dissipation test results

Figure 6.16 shows results from penetration phase at location OYSC67. From 6 m depth the average HPT pressure is higher than the piezometric pressure and increases linearly along with the piezometric pressure until about 16 m depth, with some minor deviations. As a result, the estimated hydraulic conductivity show more tendency to linearly decrease with depth from $(2.0 \pm 1.0) \times 10^{-4}$ m/s at 5 m depth towards $(2.0 \pm 1.0) \times 10^{-6}$ m/s at 13.5 m depth. The EC starts to increase from 10 m depth. Parts of the estimated K is below model limit.

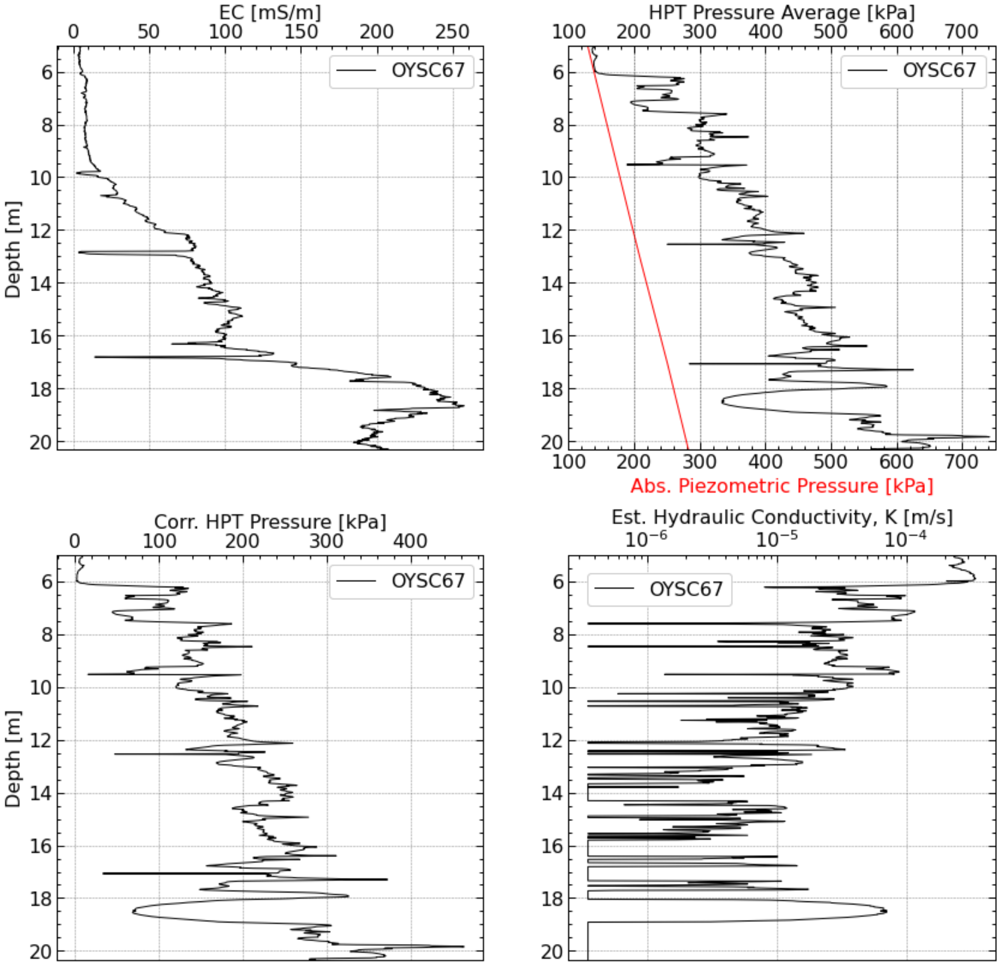

Figure 6.16: Penetration results from OYSC67

6.3.4 HPT Estimation of Hydraulic Conductivity Using BO Approach

By using Section 3.7.3, Equation (3.14) and assuming efficiency factor E = 1.0 for fairest approach, the estimated hydraulic conductivity using EQ ref results are shown in Figure 6.17. Overall the lower values of estimated K is filtered out and higher values are lowered.

OYSC64-B

For OYSC64, the estimated K in Figure 6.12 differs from OYSC64-B by being generally more stable with est. K around $(2.0 \pm 1.0) \times 10^{-4}$ m/s above 12 m depth. In OYSC64-B, this is lowered and a visual average is around $(2.0 \pm 5.0) \times 10^{-5}$ m/s, but with more flickering. OYSC64-B is not impacted as much by sudden drops in estimated K and therefore can be viewed more stable at lower depths than 12 m.

OYSC66-B

For OYSC66-B, a visual average above 14 m depth can be interpret to $(2.0 \pm 5.0) \times 10^{-5}$ m/s, but with much more flickering than OYSC66 in Figure 6.14. Below 14 m depth, the variation is bigger, but trends a lower est. K.

OYSC67-B

OYSC67-B is generally stable and show a slight linear fall from $(4.0 \pm 1.0) \times 10^{-6}$ m/s at 6 m depth towards $(1.5 \pm 1.0) \times 10^{-6}$ m/s at 18 m depth. This differs from OYSC67 in Figure 6.16, where the linear tendency is visual less stable, with more drops, and trends down a whole exponential power from 6 m depth towards 14 m depth. OYSC67-B seems therefore more stable than OYSC67.

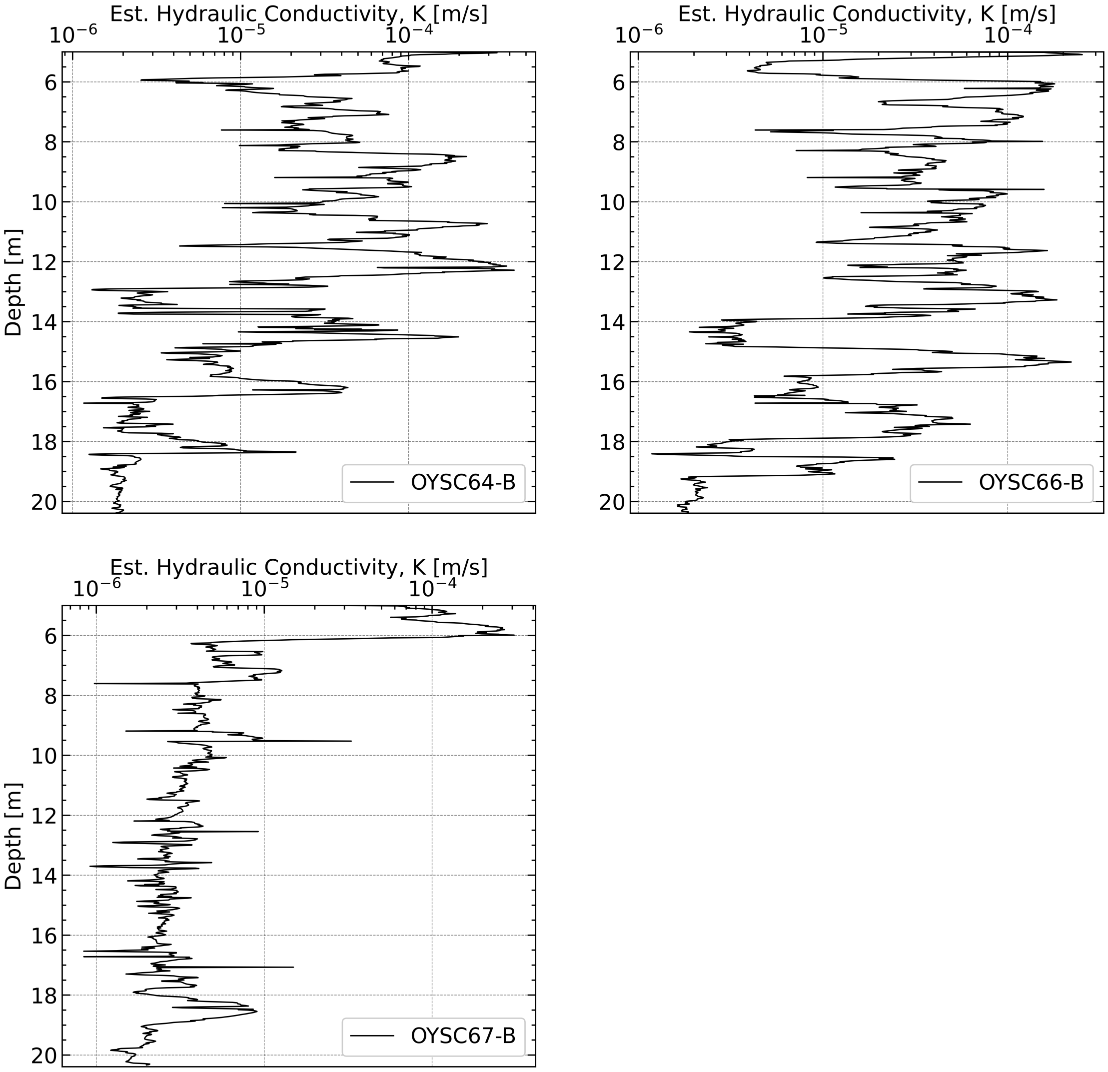

Figure 6.17: Est. hydraulic conductivity for HPT runs at test location 2 using equation by (Borden et al., 2021).

6.3.5 HPT Estimation of Hydraulic Conductivity Using ZH Approach

By using Equation (3.15), the estimated hydraulic conductivity is presented in Figure 6.18.

OYSC64-Z

OYSC64-Z displays much lateral variability with jumps in up to two exponential powers over relative small depth change. A rough visual average of rise from 2.0E-07 towards 2.0E-06 m/s from depth 5.0 m down to 12.0 m is proposed. Below 12.0 m depth, the trend in K is overall lower, ending with 1.0E-08 at 20.5 m depth.

OYSC66-Z

OYSC66-Z displays very similar behaviour as OYSC64-Z, but with slightly lower visual lateral variability. A trend linear decline from 4.0E-07 at 14.0 m towards 2.0E-08 at 20.5 m exists. A rough average of 1.0E-06 *K* above 14.0 m depth is present.

OYSC67-Z

OYSC67-Z display the most relative stable values of estimated hydraulic conductivity in Figure 6.18. A rough profile can be interpret starting at 1.0E-06 at 5.0 m going down to 12.0 m, before decreasing linearly down to 1.0E-08 at stopped depth.

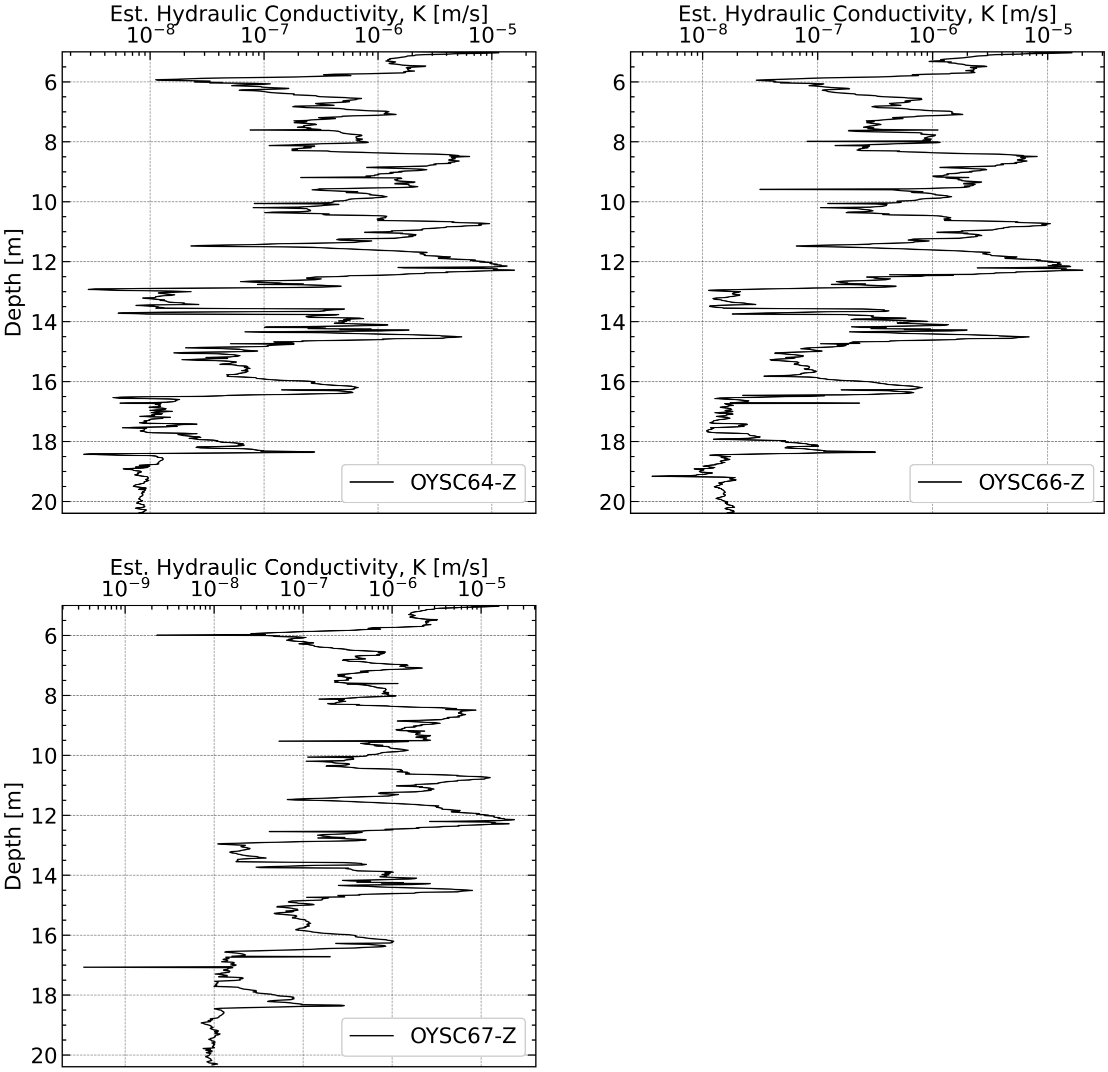

Figure 6.18: Estimated hydraulic conductivity from HPT using model by (Zhao and Illman, 2022).

6.3.6 Conclusion HPT Runs at Test Location 2

Estimating Ground Water Level

Generally, dissipation stops for HPT shows stable results, with only minor internal variations in back-calculated static water level. Overall the average static water level determined by HPT tests is at 2.5

m below ground level. All tests display more or less perfect hydrostatic behaviour down to 16.7 m. This gives a good foundation for calculations of estimated hydraulic conductivity down to 16.7 m, but also assumes hydrostatic groundwater pressure down to stopping depth, about 20.4 m. This could vary, but is not expected to do so at Øysand, due to the stratification in Appendix A and the corrected cone resistance for test location 1 in Figure 4.5, implying coarser material at depths between 16.7 to 20.4 m. All back-calculated static water levels by the HPT dissipation tests was lower than old piezometric readings and H_0 readings by falling head tests, by average around ΔGWL = 25 cm. This was neglected for the calculation of corrected HPT pressure P_c.

Electric Conductivity

Both OYSC64 and OYSC66 shows stable, low EC until around 14 m depth, were a steep rise occurs. OYSC67 shows a more stable, linear rise from depth 10 m. High EC implies clay content in freshwater formations (Slowiok et al., 2022; Wesley McCall and Christy, 2020), but must be considered with caution, as the Wenner array is sensitive to contamination and non-freshwater conditions. Piezometric measurements performed close to the river by (S. Quinteros et al., 2019) shows that the ground water pressure is affected by neap and spring tides from the nearby fjord with sea water, but measurements presented in Figure 4.7 don't show the same cyclic variation. Therefore it is assumed that EC is not affected by seawater at test location 1.

Variability in stratification is confirmed by CPTU results in Figure 4.5 and Appendix C, implying finer grained content can be present in layers identified as variations of "SAND" below 10 m depth in Figure 4.4. The high EC below 14 m depth for all test supports this variability, implying clay content below mentioned depths.

Variations in Estimated Hydraulic Conductivity

Results from HPT tests implies estimated hydraulic conductivity in the range 3.50E-04 to 3.53E-07 m/s for interpretation using Equation (3.13), but the lowest values in the 10E-07 range is mostly straight vertical, as OYSC67 from depth 19.0 to 20.4 m in Figure 6.16, is considered to be outside the model limit.

In Section 6.3.4 the results vary in the range 4.25E-04 to 1.5E-06. Overall the hydraulic conductivity presented in Section 6.3.5 displays the lowest values.

Considering all models for estimation of K, the suggested profiles are difficult to interpret and show large variation. This may be due to K being in the lower end of the models or that only a single-screen injection port gives a complex flow pattern, not true radial but more horizontal. Also, the assumption that excess pore pressure by the probe penetration is dissipated when reaching the injection port, i.e. sensor location, is true for drained material, but the soil at test location 1 will exhibit partial-drained behaviour, as indicated by pore pressure u_2 in Figure 4.5 (Bihs, Long, Nordal and Paniagua, 2021). This will affect the measured pressure at the injection port.

6.4 Falling Head Tests

Results and estimated hydraulic conductivity for falling head tests is presented in the following sections, by employed approach as shown in Section 3.5. Data was filtered to start the interpretation at maximum pressure head. The falling head pressure data is corrected for atmospheric pressure, measured by the barologger. Due to procedure in Section 5.1.4 leakage is not expected to occur, which would give error in falling head pressure. When the logger is lowered down the standpipe, the pore pressure at filter location will rise. This is accounted for by starting the falling head test 10-15 minutes after logger is lowered down the standpipe, to let the Δu by the logger induced volume to dissipate. An overview of performed tests with back-calculated change in pore pressure, Δu, is presented in Table 6.12.

Table 6.12: Performed falling head tests.

Test ID	Logger depth bgl [m]	Δu [kPa]	Date performed
OYSL03-3-1	6.6	20.224	29.04.23
OYSL03-3-2	6.6	19.717	30.04.23
OYSL05-5-1	10.2	23.257	20.04.23
OYSL05-5-2	10.2	23.254	30.04.23
OYSL06-6-1	8.2	22.517	30.04.23
OYSL06-6-2	8.2	22.209	30.04.23
OYSL07-7-1	12.94	35.911	30.04.23
OYSL07-7-2	12.94	33.979	01.05.23

Used dimensions and shape factor is presented in Table 6.13, calculated using Equation (3.5).

Table 6.13: Used dimensions for calculation of estimated hydraulic conductivity

Relationship, L/D [-]	Internal cross-section liason tube, S_{inj} $[cm^2]$	Shape factor, c [cm]
8.385	5.0671	64.5873

6.4.1 Chapuis Interpolation Method

Figure 6.19 displays the measured falling head pressure with the interpolation points and the calculated velocity for all tests but OYSL07. Measurements done by the logger the first 10 seconds after maximum head pressure was skipped and Δ15 cm was used as a selecting condition for interpolation points, due to assessed data uncertainty of water pressure H. Number of interpolation points varies, range n = 12-14, due to falling head pressure and the selecting condition. Since the water pressure flats out with time, the dissipation of the induced head is assumed completed and the pressure stabilize around static water level inside the standpipe. Same amount of water was used to initiate head $H(t = 0)$ for all tests.

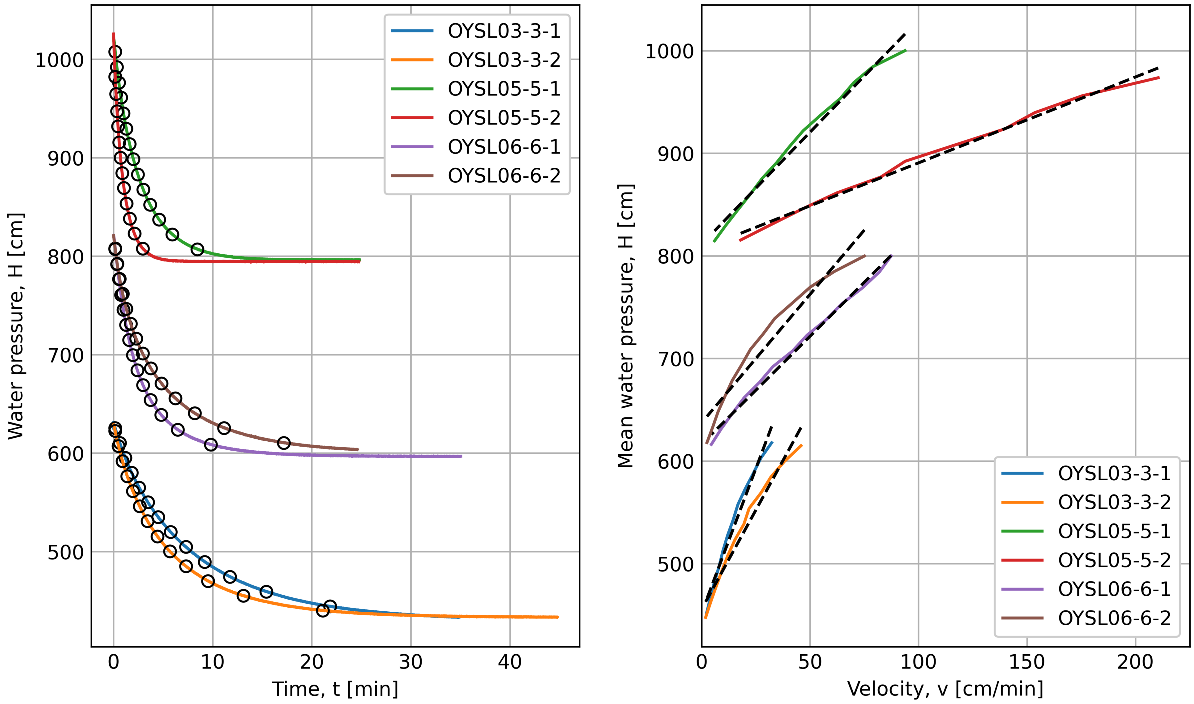

Figure 6.19: Pressure head and velocity using Chapuis method.

Results from interpretation of velocity graph in Figure 6.19 is shown in Table 6.14. There is some internal variation in piezometric error, interception of linear regression with mean pressure head, which gives variation in back-calculated GWL. The fit of the linear regression analysis is overall good, as shown by the coefficient of determination. The estimated hydraulic conductivity is within the same exponential power for tests, except results for OYSL05.

Table 6.14: Results from velocity graph in Figure 6.19

Test ID	H_0 [cm]	GWL bgl [m]	R^2 [-]	Est. K velocity graph [m/s]
OYSL03-3-1	451.93	2.08	0.9732	2.337E-06
OYSL03-3-2	455.51	2.04	0.9672	3.402E-06
OYSL05-5-1	811.20	2.09	0.9863	6.012E-06
OYSL05-5-2	806.84	2.13	0.9916	1.570E-05
OYSL06-6-1	616.30	2.04	0.9943	6.241E-06
OYSL06-6-2	637.20	1.83	0.9335	5.249E-06

Linear interpolation of selected points from pressure head in Figure 6.19 is corrected $H_r = H - H_0$, with H_0 values from Table 6.14. The result is presented in Figure 6.20. Some negative values of corrected head pressure exists, as seen by the cut-off line. The negative values and correlating time-step values were excluded from natural logarithm plot.

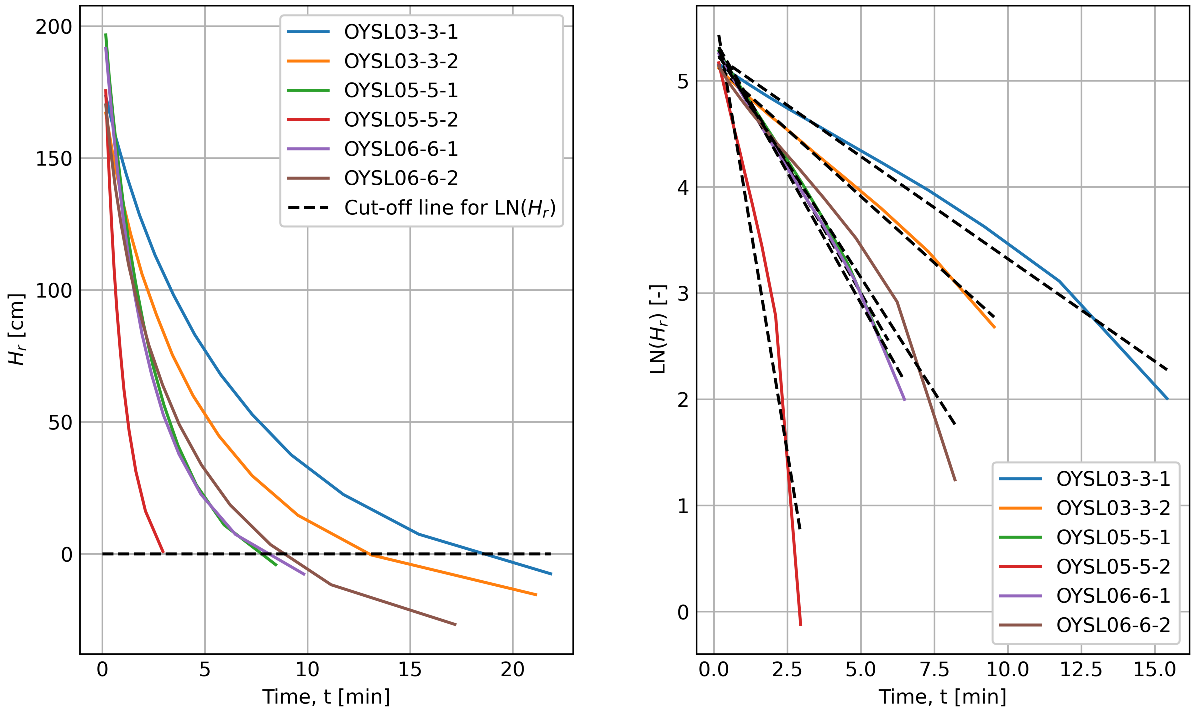

Figure 6.20: Corrected water pressure H_r and semi-log plot using Chapuis method.

Linear regression analysis of the semi-log plot in Figure 6.20 show acceptable fit in Table 6.15. The estimated hydraulic conductivity show internal variation, and again OYSL05 has the biggest internal difference.

Table 6.15: Results from semi-log plot in Figure 6.20.

Test ID	R^2 [-]	Est. K Hvorslev graph [m/s]
OYSL03-3-1	0.9844	2.535E-06
OYSL03-3-2	0.9968	3.296E-06
OYSL05-5-1	0.9942	6.300E-06
OYSL05-5-2	0.9295	2.216E-05
OYSL06-6-1	0.9941	6.478E-06
OYSL06-6-2	0.9599	5.679E-06

6.4.2 OYSL07

Due to expected clay content, as viewed by soil GSDC in Appendix D, measurements at position OYSL07 were performed over a longer period of time. The falling head pressure and interpolation points is shown in Figure 6.21. The first 10 sec of measurements were skipped and selecting condition was set to Δ10 cm.

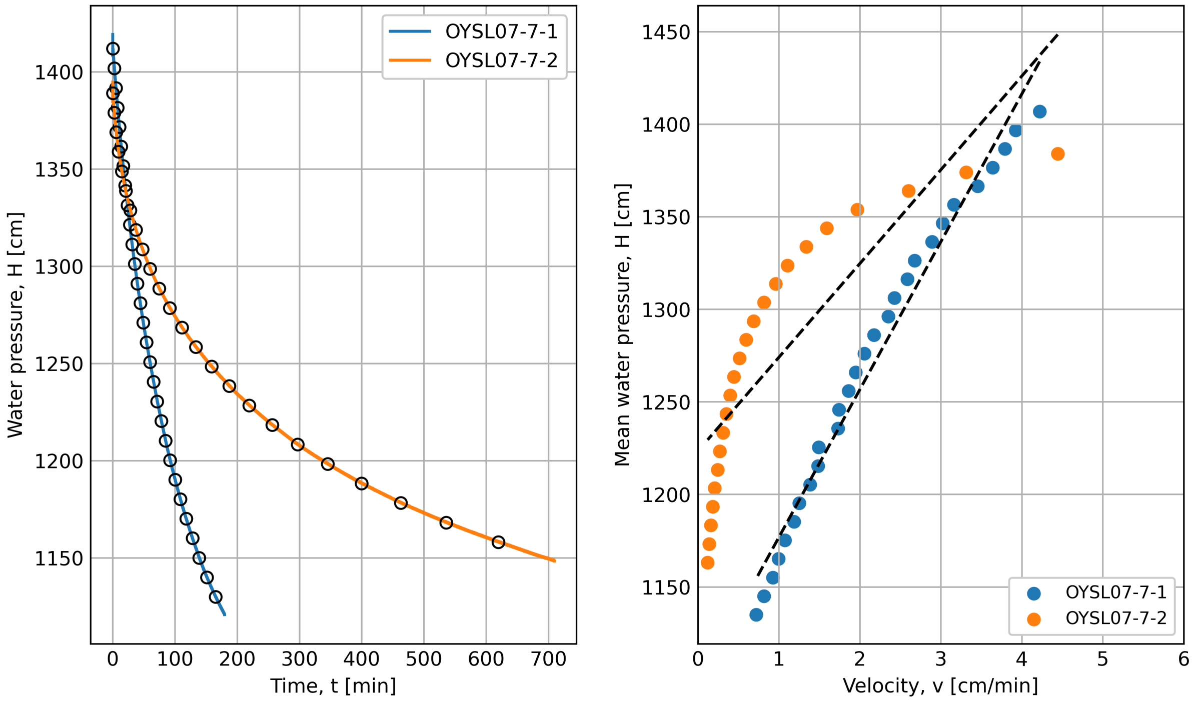

Figure 6.21: Pressure head and velocity of OYSL07.

As seen by both head pressure curves $H(t)$ in Figure 6.21, the pressure did not fully dissipate towards static water level within the pipe. The same amount of water was used for initial head pressure $H(t = 0)$, but there is a difference of 24.5 cm at initial head. This may be due to the rate water was poured down in the water rod. The levelogger was lowered to same depth location for both test. The head pressure curves $H(t)$ show big difference in velocity, as OYSL07-7-1 dissipates faster than OYSL07-7-2. Good fit is ensured for OYSL07-7-1 as the velocity is consistent, but OYSL07-7-2 makes a sharp turn halfway, behaving parabolic, implies hydraulic fracture and different K for the two sections of the graph (Chapuis et al., 2009).

Table 6.16: Results from velocity graph in Figure 6.21

Test ID	H_0 [cm]	GWL bgl [m]	R^2 [-]	Est. K velocity graph [m/s]
OYSL07-7-1	1096.97	1.97	0.9768	1.647E-07
OYSL07-7-2	1223.35 (1131.75)*	0.71 (1.62)*	0.702 (0.98)*	2.596E-07 (4.103E-08)*
*Interpretation of last 10 points				

Large variation is shown in back-calculated GWL in Table 6.16, due to the parabolic behaviour and bad fit of linear regression line of OYSL07-7-2. By a linear fit of the last 10 points in the velocity plot of OYSL07-7-2, the back-calculated GWL approaches same level as OYSL07-7-1, but with very low estimated hydraulic conductivity.

Figure 6.22 shows the corrected head pressure H_r and the semi-log Hvorslev plot. H_r for OYSL07-7-2 is corrected with the H_0 intercept pressure in parentheses in Table 6.16, the final portion of the velocity graph of OYSL07-7-2.

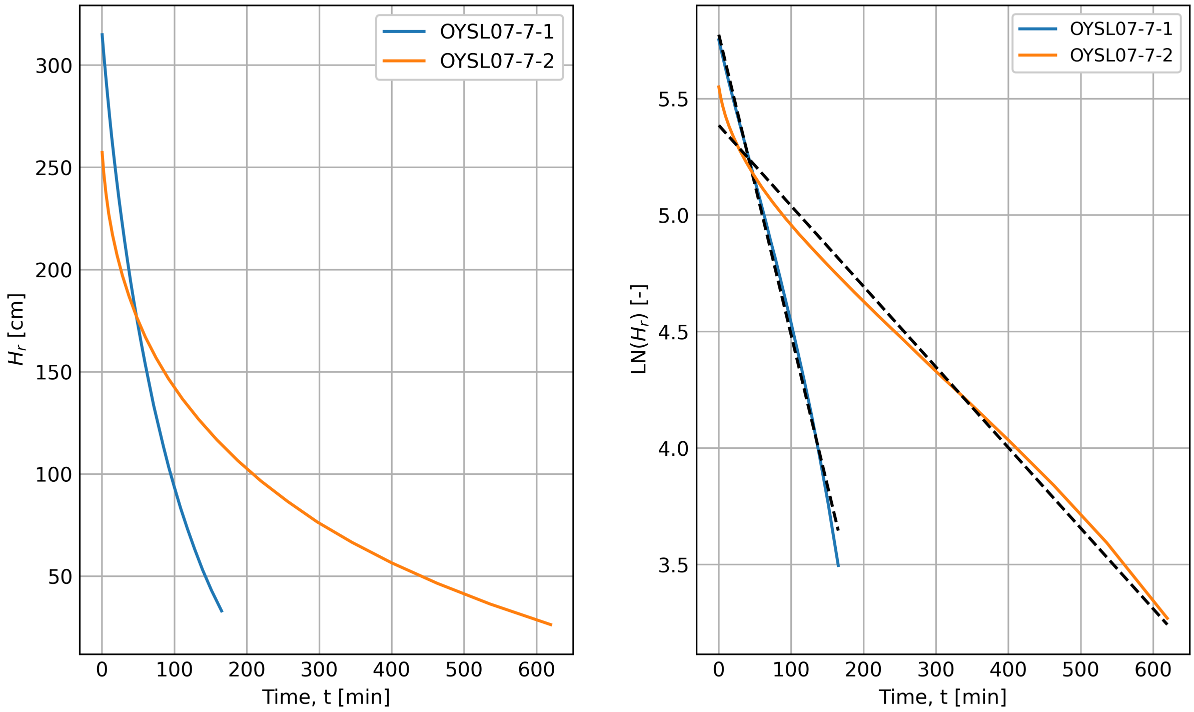

Figure 6.22: Corrected water pressure H_r and semi-log plot using both methods.

Table 6.17 shows interpret results. The fit of the linear regression curves is overall good, but OYSL07-7-2 show initial dilation. The estimated Hvorslev hydraulic conductivity in Table 6.17 is within the same power as the estimated velocity hydraulic conductivity in Table 6.16.

Table 6.17: Results from semi-log plot in Figure 6.22

Test ID	R^2 [-]	Est. K Hvorslev graph [m/s]
OYSL07-7-1	0.9947	1.696E-07
OYSL07-7-2	0.9960	4.548E-08

6.4.3 Falling Head Interpretation

Error in Estimation of Piezometric Level

Corrected head difference $H_r = H(t) - H_0$ gave some negative values for tests; OYSL03, OYSL05 and OYSL07, implying that the piezometric level was lower than the static water level (GWL) presented in Table 6.14. This implies that the linear regression of the velocity plot doesn't fully represent the small parabolic trend, when velocities becomes small. Since every test started with 10-15 minutes logging of water pressure before initiating falling head, and that the measurement point depth location on the logger was known, back-calculation of the water level inside the pipe is possible. Since falling head tests started about 10 days after installation of water standpipes, except for test OYSL05-5-1, it was can be assumed that the water level inside the pipe represents the actual GWL in the surrounding soil. By following this assumption, the actual head difference H_r is presented in Equation (6.5) below, where $H(t=\infty)$ was the lowest measured pressure 10-15 minutes prior to the initiated head. This is only true, if no clogging of the filter has occurred.

$$H_r = H(t) - H(t=\infty) \tag{6.5}$$

Results from assumed actual head difference in falling head tests are shown in Figure 6.23 and Table 6.18 for OYSL03, OYSL05 and OYSL06. Since assumed $H_0 = H(t = \infty)$, the velocity graph was skipped. Chapuis interpolation method was used, interpolation points marked with circles in H_r plots, with selecting condition $\Delta 10$ cm and exclusion of data first 10 seconds of each test.

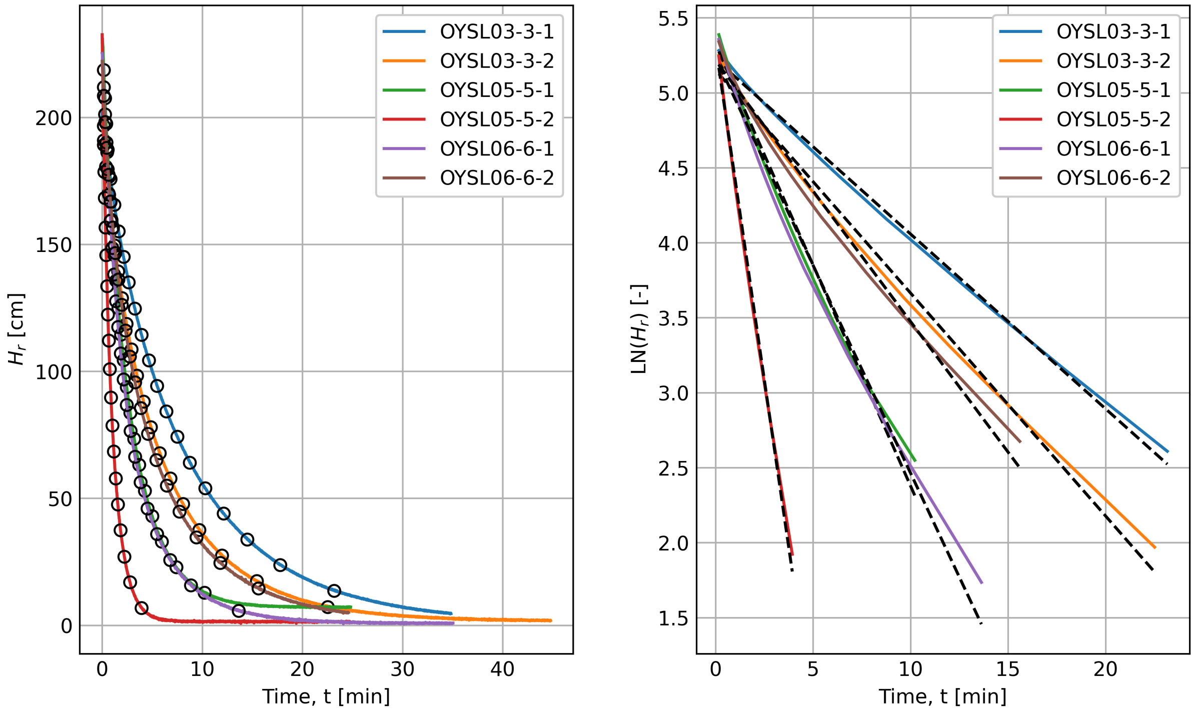

Figure 6.23: Actual head difference H_r and semi-log plot.

The semi-log plot $LN(H_r)$ with time in Figure 6.23 results in almost straight lines, implying correct correction of head difference, with very good overall linear fit. Still OYSL05-5-2 differs one order of magnitude in estimated hydraulic conductivity from OYSL05-5-1. H_r plot of OYSL05-5-2, red line in Figure 6.23, has the fastest fall in head pressure and therefore the highest estimated hydraulic conductivity. The same volume of water was poured into the standpipe for OYSL05-5-1 and OYSL05-5-2, as can be seen by $H(t = 0)$ in Table 6.18. The tests were performed at different dates, refer to Table 6.12, with OYSL05-5-1 performed only one day after installation. The initial static water level $H(t = \infty)$ is almost at same level, proposing little effect of letting system settle for a long time before performing falling head tests at this depth.

Table 6.18: Results from assumed actual head difference.

Test ID	H(t=∞) [m]*	H(t=0) [cm]	GWL bgl [m]	R^2 [-]	Est. K Hvorslev [m/s]
OYSL03-3-1	4.2864	202.24	2.31	0.9969	1.532E-06
OYSL03-3-2	4.3156	197.17	2.28	0.9923	1.954E-06
OYSL05-5-1	7.8914	232.57	2.31	0.9880	3.873E-06
OYSL05-5-2	7.9315	232.54	2.27	0.9968	1.172E-05
OYSL06-6-1	5.9596	225.17	2.24	0.9835	3.644E-06
OYSL06-6-2	5.9874	222.09	2.21	0.9858	2.288E-06

*Measured static water level [m] in levelogger before applying pressure head

6.4.4 Conclusion Falling Head Tests

The performance of the falling head tests is evaluated by percentage difference between the two methods, velocity and Hvorslev, and presented in Table 6.19 where difference under 10 % is considered acceptable (Weber et al., 2016).

For interpret hydraulic conductivity using velocity method in Table 6.14 and Hvorslev method in Table 6.15, the difference of calculated K is acceptable for all tests, except OYSL05-5-2 and slightly OYSL07-7-2*. The difference between velocity method and the stabilized static water level H_0, named "real H_0 Hvorslev" in Table 6.19, is also big. This affirms that the accuracy of the velocity method is questionable in this study of Øysand sediments.

Table 6.19: Difference in results from Velocity and Hvorslev method.

Test ID	Velocity versus Hvorslev [%]	Velocity versus real H_0 Hvorslev [%]
OYSL03-3-1	8.12	41.64
OYSL03-3-2	3.17	54.09
OYSL05-5-1	4.67	43.28
OYSL05-5-2	34.12	28.99
OYSL06-6-1	3.73	52.55
OYSL06-6-2	7.88	78.56
OYSL07-7-1	2.96	-
OYSL07-7-2*	10.29	-

*Interpretation of last 10 points, see Table 6.16.

Table 6.20 shows the internal variation for test results. Internal variation between tests, i.e. like OYSL05-5-1 and OYSL05-5-2, is overall big. The same volume of water was used to initiate the falling head, but results seem to be affected by other factors. By use of the simple Equation (3.3), the soil deformation gets neglected. This may have an impact, as the changes in hydraulic head gives Δu in the surrounding soil, inducing either consolidation or swelling of finer grained sediments (Chapuis, R.P, 1998). The filter may also be victim of soil clogging by finer grains after the first performed test.

Table 6.20: Difference in internal results from Velocity and Hvorslev method.

Test ID	Internal velocity [%]	Internal Hvorslev [%]	Internal Hvorslev real H_0 [%]
OYSL03-3-1	-	-	-
OYSL03-3-2	37.11	26.09	24.21
OYSL05-5-1	-	-	-
OYSL05-5-2	89.23	111.44	100.66
OYSL06-6-1	-	-	-
OYSL06-6-2	17.28	13.15	45.70
OYSL07-7-1	-	-	-
OYSL07-7-2*	120.22	115.43	-

*Interpretation of last 10 points, see Table 6.16.

6.5 Estimated Hydraulic Conductivity from Old CPTU Tests

Hydraulic conductivity is estimated from previous CPTU runs by NGI at both test locations, using interpretation methods presented in Section 3.8.

6.5.1 Test Location 1

Much like the corrected cone resistance plot in Figure 4.5, the estimated K varies within test location 1, as the cone resistance varies. Est. K varies approximately within the range 10E-04 to 10E-08, where OYSC61 displays the most distorted result, as seen in Figure 6.24.

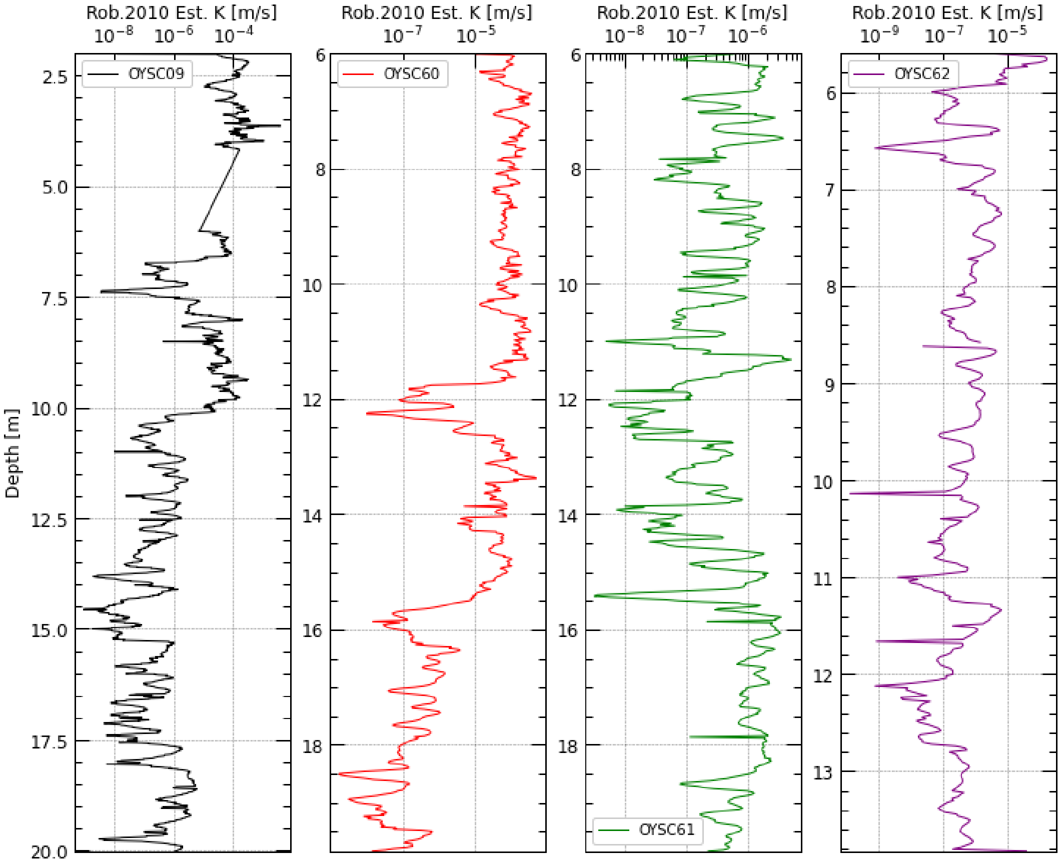

Figure 6.24: Estimated hydraulic conductivity from old CPTU runs at test location 1.

6.5.2 Test Location 2

The estimated hydraulic conductivity K from CPTU at test location 2 can be approximated into two sections:

Depth 6.5 - 12.0 m: 2.0E-07 m/s

Depth 12.0 - 20.0 m: 2.0E-05 m/s

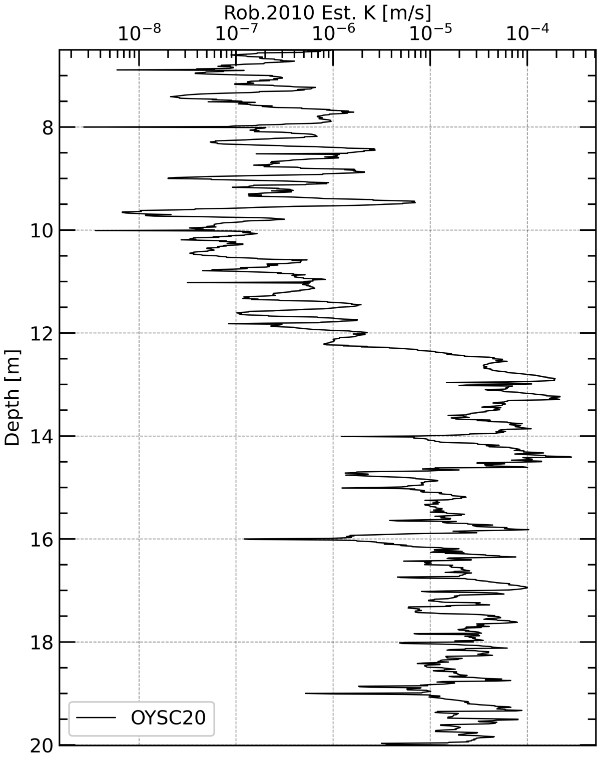

Figure 6.25: Estimated hydraulic conductivity from old CPTU runs at test location 2.

Chapter 7

Laboratory Tests

This chapter presents laboratory tests to determine hydraulic conductivity. These was performed to have a benchmark comparison for hydraulic conductivity determined by in-situ field tests at depth 10.0 m.

7.1 Measured Results

Orientation, borehole, depth and mean effective consolidation stress for specimens tested in triaxial cell is shown in Table 7.1. The complete grain size distribution curves of tested specimens is shown in Appendix E.

Table 7.1: Specimen tested in triaxial cell.

Test ID	Orientation	Borehole	Depth range, bgl [m]	σ'_m [kPa]	Initial height [cm]
1C	Vertical	OYSB10	13.325 - 13.485	88	10.858
2Af	Horizontal	OYSB21	10.053	66	7.256
2Bf	Horizontal	OYSB21	10.16	66	7.767
2Cf	Vertical	OYSB21	10.08 - 10.11	66	2.839
1Bf*	-	-	-	-	

f = frozen sample.
* Dummy trial for coring procedure test.

7.1.1 Correction

In this setup, large axial strain during thawing occurred to every frozen specimen, as seen in Table 7.2. This may be due to the applied axial load during thawing, a fault in the load sensor due to gradual temperature change leading to an unconsciously bigger axial load, in-situ heaving during the freezing procedure and compression of this heaving during thawing or a combination of these.

Due to thawing performed with a mix of air and cold water in the drainage lines, i.e. thawing before flushing stage, no volume change by the GDS controllers was measured. But a change in volume is anticipated because of the axial strain in Table 7.2, because only axial and correlating negative radial change implying no volume change does not concur with the natural process of heaving and thawing. As mentioned in Section 5.2.2, the silty sand was expected to heave during ground freezing (S. Quinteros, 2022). Ice lenses can be spotted in the bottom corner of specimen 2Bf in Figure 7.1b. When the ice crystals melts, the volume decreases leading to compaction of the specimen. This can lead to grain rearrangement within the specimen (Chamberlain and Gow, 1979).

Area is key to calculate the correct hydraulic conductivity. Because of the unknown deformation process during thawing, the area after consolidation was used for calculation of hydraulic conductivity, as shown in Table 7.2. Therefore, as the calculated volumetric strain under consolidation might imply good sample quality, the axial strain during thawing reveals bad sample quality and that the initial in-situ fabric is disturbed.

Table 7.2: Axial strain during thawing of frozen specimen

Test ID	ΔH [mm]	Axial strain, ϵ_a [%]	Area after consolidation [cm^2]
2Af	1.767	2.44	23.204
2Bf	2.220	2.86	23.035
2Cf	1.37	4.83	23.163

(a) Specimen 2Af in frozen, intact state.

(b) Specimen 2Bf in frozen, intact state.

(c) Specimen 2Cf in frozen, intact state.

Figure 7.1: Frozen, intact specimens before build in triaxial cell.

7.1.2 Test 2Af

Triaxial Stages Results for Test 2Af

Test 2Af experienced axial deformation during thawing as seen in Figure 7.2, which after about 24 hours stabilized around 1.767 mm. The jumps in deformation at about 5000 sec is due to testing the axial LVDT and re-calibrating it, with addition to previous deformation. The deformation stabilized after approximately 22 hours, but the thawing can be assumed finished around 5000 sec, since the axial measurement is almost at same value as the stabilized thawing deformation.

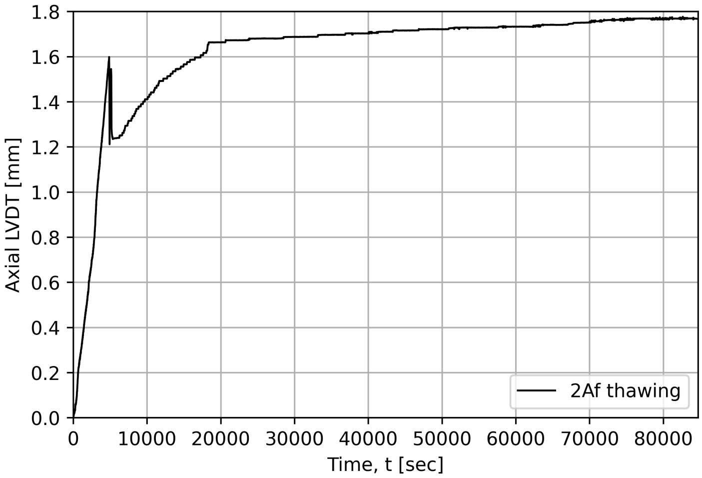

Figure 7.2: Axial deformation during thawing specimen 2Af.

Results from the different triaxial stages is shown in Table 7.3.

Table 7.3: Triaxial stages result for specimen 2Af

2Af	ϵ_a [%]	ϵ_V [%]	ΔH [mm]	End void ratio [-]	Water content [%]
Thawing	2.43	-	1.767	-	-
Saturation	2.65	-	1.924	-	-
Consolidation	2.86	0.67	2.078	-	-
End test	3.25	-	2.357	0.686	27.80

Hydraulic Conductivity Results for Test 2Af

Table 7.4 shows result for hydraulic conductivity tests performed on specimen 2Af. Initially, the volume ramp method was trialled first by a low gradient. Afterwards the amount of volume water at the same Δtime = 180 sec was increased, to increase gradient. The results for each run shows good ratio to the average determined hydraulic conductivity, as the variability ratio shows in Table 7.5.

Table 7.4: Hydraulic conductivity results for test 2Af at 21°C.

2Af	Runs [-]	Inflow/outflow [-]	Min/Max gradient, i [-]	Avg. K [m/s]
Volume ramp	8	-	0.58/1.60	2.111E-06
Target pressure	3	Min/max: 0.93 - 0.99	1.23/1.89	2.066E-06

The target pressure method was trialled at gradients a bit higher than volume ramp method, but gave almost the same result, both in average determined hydraulic conductivity and variability ratios. Inflow-outflow ratios shows acceptable flow conditions. In average, the target pressure runs was interpret over a time period of Δtime = 380 sec with volume change.

Table 7.5: Variability in determination of hydraulic conductivity for test 2Af.

2Af	Min ratio to Avg. K [-]	Max ratio to Avg. K [-]
Volume ramp	0.92	1.09
Target pressure	0.94	1.11

GSD of Test 2Af

Photo of split test 2Af and porous discs after triaxial run is shown in Figure 7.3. No shell or fragment contamination is visible. The visible soil is in line with result from the GSD test, as shown in Table 7.6, which resulted in silty sand that is medium graded.

Figure 7.3: Split specimen 2Af after triaxial hydraulic conductivity test.

The bottom porous disc in Figure 7.3 displays a fine, liquefied layer of soil mass. This is an indication that grain migration might have occurred during the hydraulic conductivity tests or the thawing process.

Table 7.6: GSD properties test 2Af

Soil fractions	% dry mass
Sand	46.2
Silt	49.9
Clay	3.9
D_{60} [mm]	0.06972
D_{10} [mm]	0.01020
C_u [-]	6.833

7.1.3 Test 2Bf

Triaxial Stages Results for Test 2Bf

Axial deformation during thawing of specimen 2Bf is shown in Figure 7.4. At about 8000 sec, ΔH stabilized at 2.220 mm. The thawing starts slow, but after 1000 seconds it shows linear tendencies up to $\Delta H = 0.5$ mm. Later the thawing is semi-linear, parabolic tendencies, with a lower gradient than the initial thaw stage.

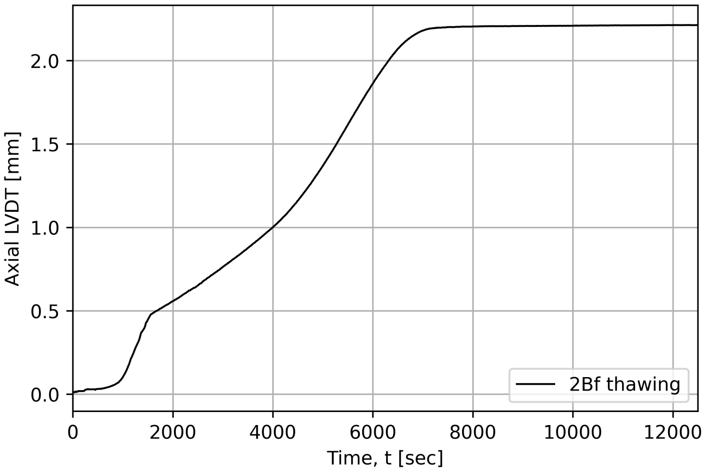

Figure 7.4: Axial deformation during thawing specimen 2Bf.

The results from triaxial stages for specimen 2Bf is shown in Table 7.7.

Table 7.7: Triaxial stages result for specimen 2Bf

2Bf	ϵ_a [%]	ϵ_V [%]	ΔH [mm]	End void ratio [-]	Water content [%]
Thawing	2.85	-	2.220	-	-
Saturation	3.00	-	2.331	-	-
Consolidation	3.24	0.68	2.517	-	-
End test	3.75	-	2.917	0.675	26.87

Hydraulic Conductivity Results for Test 2Bf

Test 2Bf was initially trialled with target pressure method at low gradient, increasing up to i=1.44 on last run. This gave hydraulic conductivity as presented in Table 7.8. Inflow-outflow ratio is within acceptable limits. In average, the volume change was interpret over a time period of ∆time = 505 sec.

Table 7.8: Hydraulic conductivity results for test 2Bf at 21°C.

2Bf	Runs [-]	Inflow/outflow [-]	Min/Max gradient, i [-]	Avg. K [m/s]
Target pressure	3	Min/max: 0.96 - 1.03	0.34/1.44	8.418E-07
Volume ramp	3	-	3.07/4.44	7.836E-07

Volume ramp method trials were pushed to a higher gradient, doubled from max gradient performed with target pressure method, to observe the difference made in the determined hydraulic conductivity. Volume ramp method has a 6.91% increase in average hydraulic conductivity, compared to target pressure method. All volume ramp runs were conducted with set time period of ∆time = 180 sec. Both measurement methods show good min and max ratio to their average determined hydraulic conductivity in Table 7.9.

Table 7.9: Variability in determination of hydraulic conductivity for test 2Bf.

2Bf	Min ratio to Avg. K [-]	Max ratio to Avg. K [-]
Target pressure	0.91	1.06
Volume ramp	0.94	1.07

GSD of Test 2Bf

No contamination or shell fragments were found in test 2Bf after dismounting, as shown in Figure 7.5. In this picture, the specimen is turned opposite of the position in the triaxial cell. The upper porous disc, i.e. bottom cap porous disc in the cell, show remains of fine grains due to grain migration either from thawing stage or from flows in hydraulic testing.

Figure 7.5: Split specimen 2Bf after triaxial hydraulic conductivity test.

The GSD results in Table 7.10 classifies specimen 2Bf as a medium graded silty sand.

Table 7.10: GSD properties test 2Bf

Soil fractions	% dry mass
Sand	39.8
Silt	57.4
Clay	2.8
D_{60} [mm]	0.06276
D_{10} [mm]	0.00933
C_u [-]	6.729

7.1.4 Test 2Cf

Triaxial Stages Results for Test 2Cf

Axial deformation of specimen 2Cf stabilized at 1.37 mm after 17500 sec, as seen in Figure 7.6 and remained unchanged till the next day. A slight swelling occurred after reaching top axial deformation at approximately 7500 sec, as the deformation declines slowly towards 1.37 mm at 17500 sec.

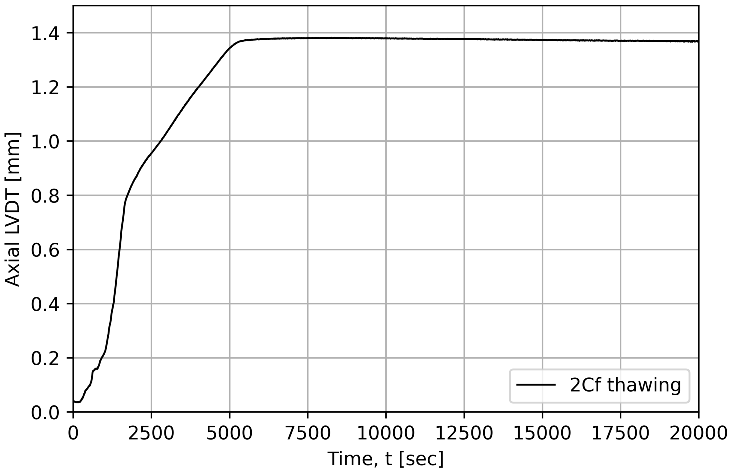

Figure 7.6: Axial deformation during thawing specimen 2Cf.

The results from triaxial stages for specimen 2Cf is shown in Table 7.7.

Table 7.11: Triaxial stages result for specimen 2Cf

2Cf	ϵ_a [%]	ϵ_V [%]	ΔH [mm]	End void ratio [-]	Water content [%]
Thawing	4.82	-	1.37	-	-
Saturation	5.09	-	1.445	-	-
Consolidation	5.36	1.84	1.522	-	-
End test	6.50	-	1.845	0.692	25.34

Hydraulic Conductivity Results for Test 2Cf

High gradients for both measuring methods was trialled on specimen 2Cf, as seen in Table 7.12. Volume ramp achieved a higher average hydraulic conductivity than target pressure, due to higher gradients. The target pressure was interpret over a time period Δtime = 450 sec on average, while volume ramp period was set to Δtime = 180 sec.

Table 7.12: Hydraulic conductivity results for test 2Cf at 21°C.

2Cf	Runs [-]	Inflow/outflow [-]	Min/Max gradient, i [-]	Avg. K [m/s]
Target pressure	4	Min/max: 0.97 - 1.01	3.84/8.84	1.746E-07
Volume ramp	3	-	5.76/14.40	2.064E-07

The measurements show acceptable variability by the ratios shown in Table 7.13 for both methods.

Table 7.13: Variability in determination of hydraulic conductivity for test 2Cf.

2Cf	Min ratio to Avg. K [-]	Max ratio to Avg. K [-]
Target pressure	0.90	1.07
Volume ramp	0.94	1.05

GSD of Test 2Cf

A small shell fragment was found in specimen 2Cf, as seen on the right side of the split specimen in Figure 7.7. This will affect the assumed linear flow through the specimen. liquefied grain mass is shown on the bottom porous disc, implying particle migration.

Figure 7.7: Split specimen 2Cf after triaxial hydraulic conductivity test.

The GSD properties in Table 7.14 show a substantial clay content in specimen 2Cf. Due to this, uniform coefficient was not determined.

Table 7.14: GSD properties test 2Cf

Soil fractions	% dry mass
Sand	24.3
Silt	63.7
Clay	12.0
D_{60} [mm]	0.039
D_{10} [mm]	-
C_u [-]	-

7.1.5 Test 1C

Triaxial Stages Results for Test 1C

Results from triaxial stages for the regular, not frozen, specimen 1C is shown in Table 7.15. From S. Quinteros et al., 2019 OCR for test location 1 is equal to 1.0. By comparing the volumetric strain ϵ_V with sample quality charts by Andersen and Kolstad, 1980, specimen 1C is evaluated to be of perfect quality, though the specimen is slightly out of depth range.

Table 7.15: Triaxial stages result for specimen 1C

1C	ϵ_a [%]	ϵ_V [%]	ΔH [mm]	End void ratio [-]	Water content [%]
Saturation	0.55	-	0.600	-	-
Consolidation	1.38	1.20	1.5	-	-
End test	1.610	-	1.748	0.891	32.45

Hydraulic Conductivity Results for Test 1C

Only target pressure method was applied for hydraulic testing of specimen 1C. The inflow/outflow ratio is within acceptable range and different gradients gave hydraulic conductivity as shown in Table 7.16. The average change in volume was interpret over a time period of $\Delta t = 308$ sec.

Table 7.16: Hydraulic conductivity results for test 1C at 21°C.

1C	Runs [-]	Inflow/outflow [-]	Min/Max gradient, i [-]	Avg. K [m/s]
Target pressure	3	Min/max: 0.89 - 0.97	4.61/9.08	3.188E-08

The variability between the different calculated values of hydraulic conductivity is deemed acceptable.

Table 7.17: Variability in determination of hydraulic conductivity for test 1C.

1C	Min ratio to Avg. K [-]	Max ratio to Avg. K [-]
Target pressure	0.96	1.07

GSD of Test 1C

Figure 7.8 shows split specimen 1C after hydraulic testing. Unfortunately, porous discs was not included in photo. No shell fragments were found in the specimen.

Figure 7.8: Split specimen 1C after triaxial hydraulic conductivity test.

Result from GSD test in Table 7.18 classifies specimen 1C as a medium graded sandy silt.

Table 7.18: GSD properties test 1C

Soil fractions	% dry mass
Sand	37.1
Silt	60.1
Clay	2.8
D_{60} [mm]	0.05868
D_{10} [mm]	0.00917
C_u [-]	6.398

7.2 Conclusion Laboratory Tests

7.2.1 Procedure

By assuming no ice lenses in specimens and no in-situ heaving during ground freezing, the axial strain during thawing can resort from the load cell. Load cell was zeroed and calibrated at -9°C but not afterwards at 21 °C. This can lead to wrong load calibration factors being employed by the software leading to fault in load applied by the bottom axial loader. By visual inspection, the load rod had connection with the top cap of the specimen during the entire procedure after initial zero readings. If more load than F = 0.001 kN were applied to the frozen specimens during thawing, they might have experienced a higher degree of anisotropic stress than intended.

The large amount of axial strain between stages consolidation and end test in the triaxial stages results tabs for the specimens is due to errors when connecting the hydraulic pump before hydraulic conductivity tests.

The drainage lines should have been saturated with frost fluid before thawing. Since frost fluid is based on a mixture between alcohol and water, the effect on soil mechanical properties can be assumed to be negligible. The difference in fluid properties could also have been assumed negligible resulting in volumetric change data during thawing.

7.2.2 Sample Quality

All frozen samples exhibited significant axial strain during thawing and ending up with a final void ratio that is considerable lower than the reference non-frozen specimen 1C. Specimen 2Bf and 1C has exactly the same clay content and differ only about 3 % in silt and sand content. The difference in final void ratio between tests 1C and 2Bf is $\Delta e = 0.216$. Unfortunately, initial index testing was not performed on either the frozen or not-frozen specimens. Therefore, no initial void ratio is calculated. Also, images showing the porous discs after triaxial hydraulic tests reveal much particle migration and a very wet, liquefied interior.

Compared with another silt location in Trøndelag, the final void ratio of the frozen specimens are within values for tests at same depth, similar GSD and water content (Bihs, Long, Nordal, 1 Department of Civil and Environmental Engineering, Norwegian University of Science and Technology (NTNU), 7491 Trondheim, Norway et al., 2020). However, the sampling procedure is different and since the frozen samples experienced compression during thawing, it is suggested that the void ratio should be higher for Øysand silt.

Change in horizontal stress in pressure plate located in silt layer was eminent during the freezing process (S. Quinteros, 2022). This implies volumetric change, i.e. heaving, in the silt during freezing procedure (Yoshimi et al., 1978).

In conclusion, the conducted hydraulic testing was made on a disturbed fabric, deviating from the goal in-situ initial fabric.

7.2.3 Hydraulic Conductivity

Due to the different initial height of frozen vertical and horizontal specimen and no correlation between determined hydraulic conductivity and orientation, no conclusion about anisotropy can be made with confidence. The hydraulic conductivity is within range of suggested results by soil fraction (Janbu, 1989).

By using Equation (3.21) and temperature readings from in-situ falling head tests loggers, the final determined hydraulic conductivity laboratory tests at average temperature 4°C is presented in Table 7.19 for both methods.

Table 7.19: In-situ temperature 4°C corrected hydraulic conductivity for laboratory tests.

Hydraulic conductivity at in-situ 4°C, K [m/s]		
Test ID	Target pressure	Volume ramp
2Af	1.284E-06	1.312E-06
2Bf	5.234E-07	4.872E-07
2Cf	1.086E-07	1.283E-07
1C	1.982E-08	-

Chapter 8

Comparison of Results and Evaluation of Methodology

In this chapter, all results from performed tests are presented in same plots for easier comparison. The results are evaluated in relationship with each other in order to recommend a hydraulic profile for each location. Secondly the different tools and employed methodology is discussed and evaluated.

8.1 Test Location 1 Comparison and Evaluation

To present the results in a comparable manner and due to the lateral variability present in test location 1, see Section 4.2.1, the various employed field and laboratory tests are divided into two groups as presented in Figure 8.1. Within each group, the following tests were performed:

Group A: Falling head tests, HPT, CPTU

Group B: HPT, CPTU, Triaxial hydraulic testing

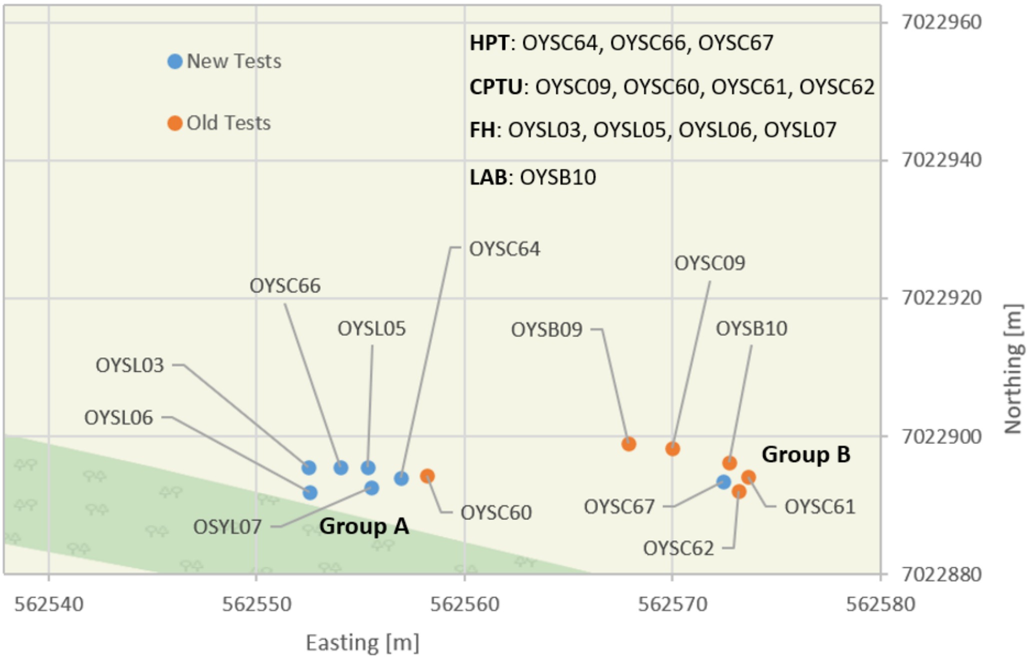

Figure 8.1: Evaluated positions at test location 1.

8.1.1 Group A

Figure 8.2 shows the compiled result for hydraulic conductivity at test location 1a from 6.0 to 20.0 m depth.

The falling head tests display internal variation, see Section 6.4.4, but are nevertheless treated with the most weight, i.e. benchmark, for comparison of the derived result from direct-push HPT tool and estimate of hydraulic conductivity by derived CPTU parameters. Big variability is present at all levels of depth and the hydraulic conductivity ranges from 3.0E-04 to 1.0E-08 m/s.

From depth 6.0 to 11.5 m, the HPT results from approaches Section 3.7.2 and Section 3.7.3, ending with "MC" and "B" in Figure 8.2, display very similar result as the estimated hydraulic conductivity from CPTU test OYSC60. There is a small noticeable difference between HPT MC and HPT B, where the first approach display overall higher values of K. HPT MC displays less internal variation than HPT B. The last approach of HPT results, see Section 3.7.4, ending with "Z" in Figure 8.2 display very little internal variation, but differs from HPT MC and HPT B by approximately 2 values of exponential powers. Also, HPT Z trends less stable than both HPT B and HPT Z, displaying a profile with big jumps in values of K.

Below 11.5 m depth, both HPT MC and HPT B starts to display much more internal variation. The results of OYSL07 is outside empirical model range for HPT MC and not within set range of HPT B with hydraulic efficiency factor E set to value 1.0, see Section 3.7.3. By comparison with falling head tests, the HPT Z approach fits best.

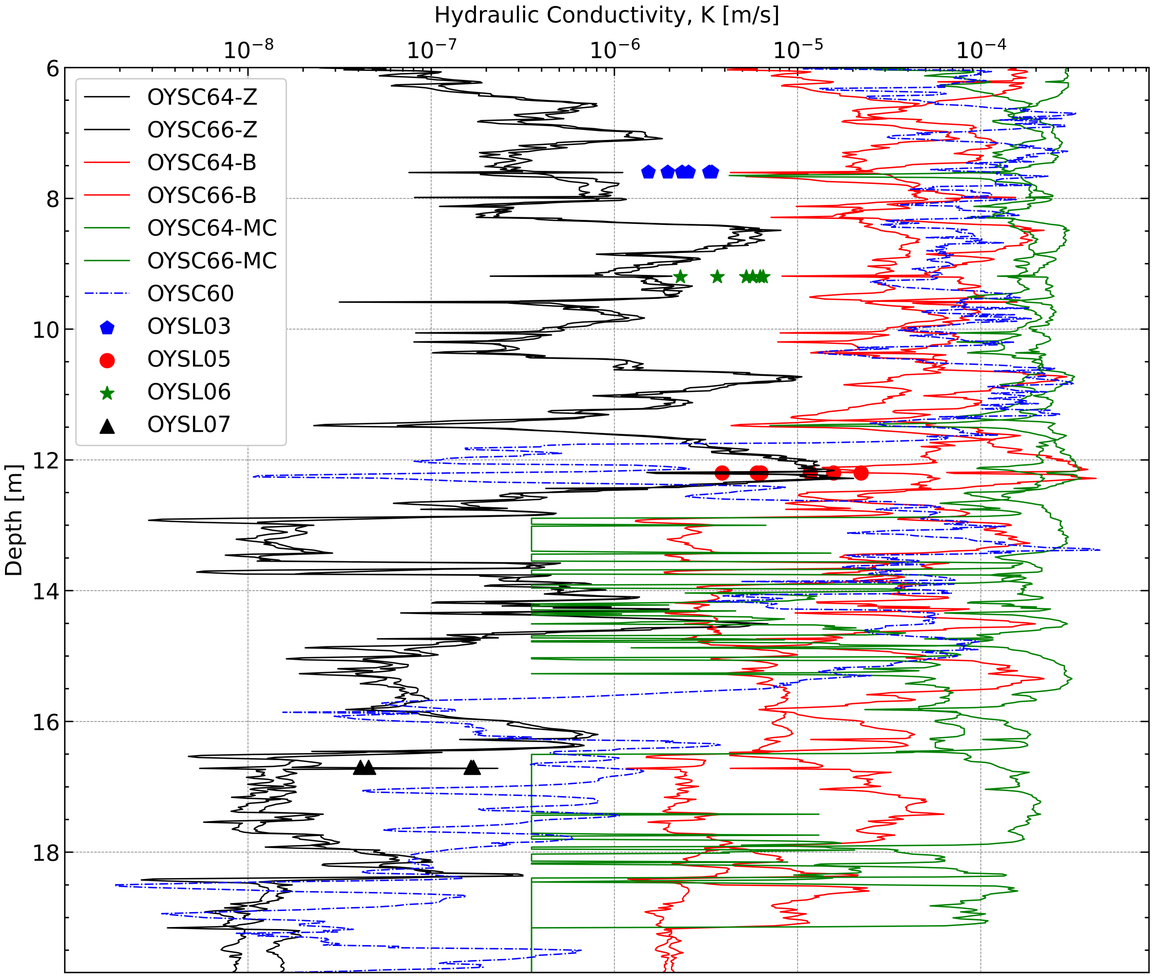

Figure 8.2: Compiled results of hydraulic conductivity at test location 1a.

Recommended Hydraulic Profile 1a

The final recommended hydraulic profile for test location 1a is shown in Figure 8.3, along with estimation of *K* from CPTU OYSC60 for comparison. Big difference in hydraulic conductivity at initial depth and down towards 11.5 m between the two direct-push methods is eminent.

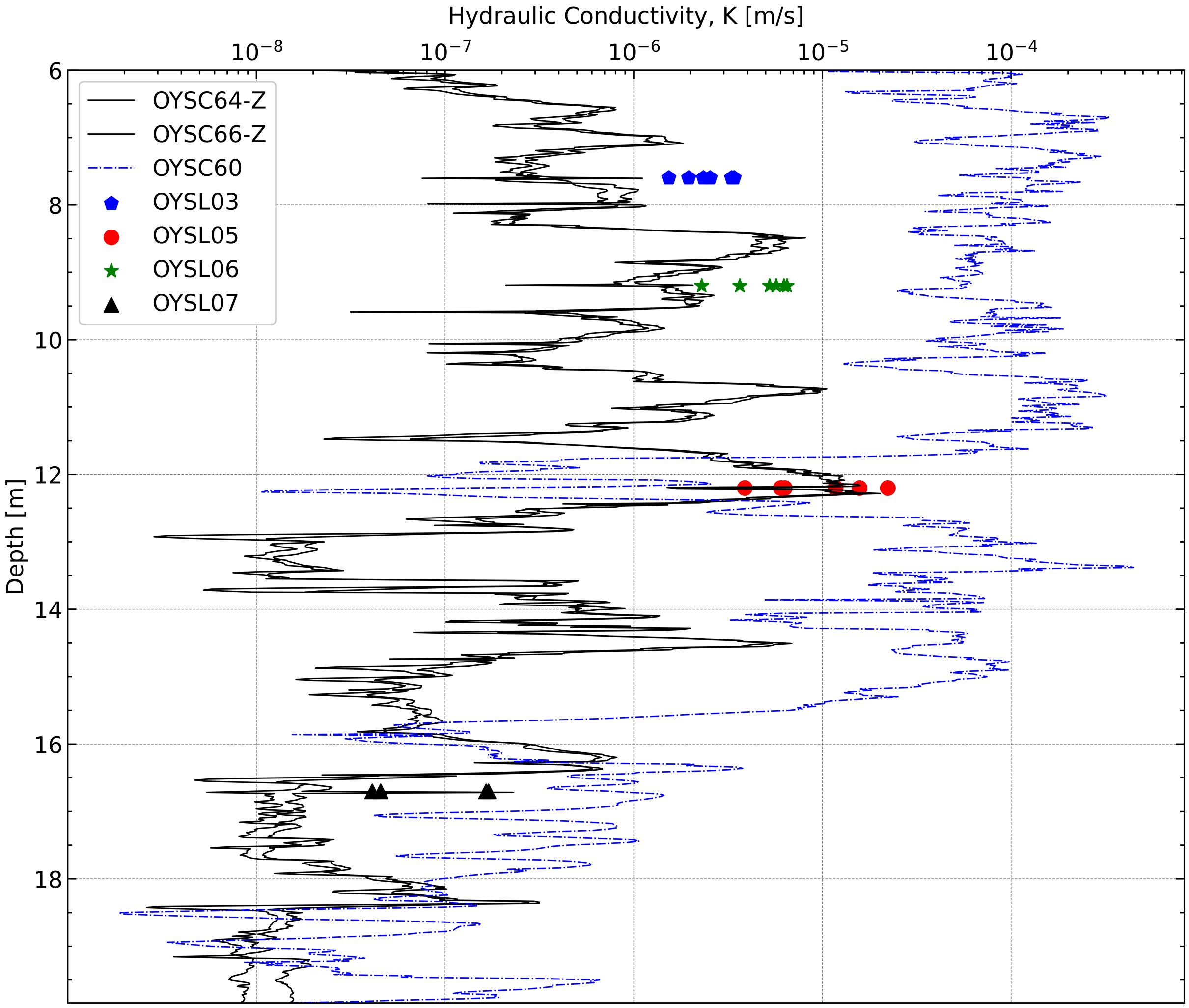

Figure 8.3: Recommended hydraulic profile for test location 1a.

8.1.2 Group B

The compiled results for hydraulic conductivity from depth 5.0 to 20.3 m at test location 1b is shown in Figure 8.4.

Overall, the results are relative coherent with difference of about two in exponential power. The lowest calculated hydraulic profile is from HPT MC approach, ranging from 2.0E-04 m/s towards empirical model limit of 3.0E-07 m/s. HPT MC displays some variability towards depth 12.0 m, but show more jumps and flickering in deeper depths. The HPT B approach displays the most stable hydraulic profile, when compared to HPT MC and HPT Z, but is closer to HPT MC in values of *K*. HPT Z approach displays much wandering within the approximate set range of the results and displays the lowest values of *K*.

Variation is eminent in the estimated profiles of *K* from CPTU, where only OYSC09 and OYSC61 goes to deeper depths at 20.0 m. As estimated *K* is derived from normalized cone correction and side sleeve friction, soil layer variability can be implied. From 6.0 to 10.0 m depth, both OYSC62 and OYSC61 follows HPT Z closely, but this trend dilutes at deeper depths.

The low K value, together with high void ratio and the GSD properties of specimen 1C, see Section 7.1.5, implies a low permeable, high compressible soil at this layer. None of the direct-push methods are close to K from triaxial specimen 1C. HPT Z, OYSC09, OYSC61 and OYSC62 is closest at about 2.0E-08 to 8.0E-08. The EC measurements of HPT OYSC67 shows about 90 mS/m at test depth 13.4 m, and rises further towards maximum EC at 18.5 m depth. The GSD of OYSB09 in Appendix D shows rising clay content with depth, which confirms the EC measurements. In Figure 4.5 the corrected cone resistance in test location 1b ranges from 3.5 to 8.0 MPa, but increases with depth and stabilize around 7.0 MPa for 20.0 m depth. This would normally imply coarser material which derives into higher permeability, see OYSC61 and OYSC09 in Figure 8.4 below 18.0 m, but this contradicts the EC measurements, GSD and HPT Z values of K. Therefore, the suggested hydraulic profile of HPT Z is recommended.

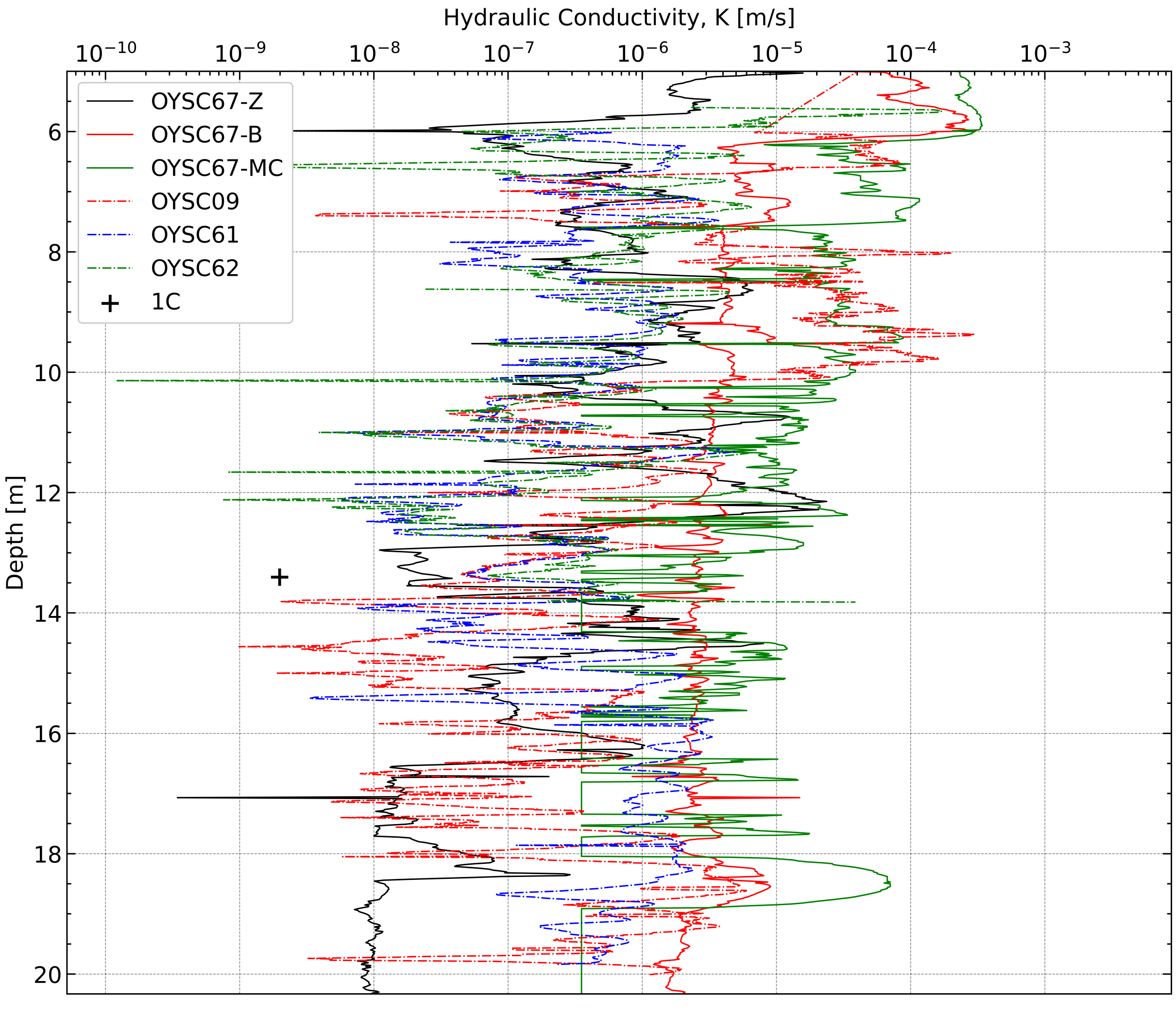

Figure 8.4: Compiled results of hydraulic conductivity at test location 1b.

Recommended Hydraulic Profile 1b

Recommended hydraulic profile for test location 1b is shown in Figure 8.5. HPT Z of OYSC67 is highlighted and CPTU estimates are included for comparison.

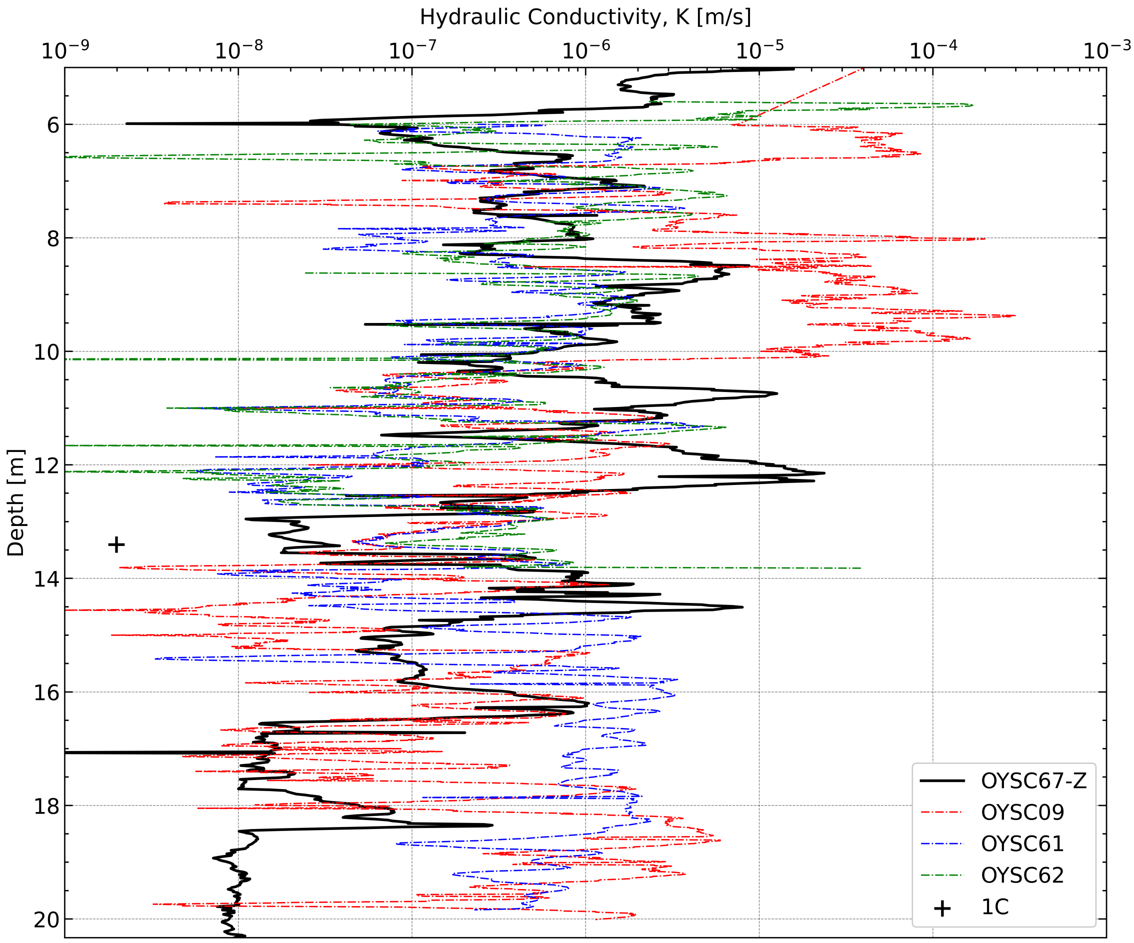

Figure 8.5: Recommended hydraulic profile for test location 1b.

8.2 Test Location 2 Comparison and Evaluation

At test location 2 the hydraulic conductivity of laboratory tests at around 10.0 m depth, Flow Cone stationary tests and CPTU penetration derived estimates are included. The positions of the different test is viewed in Figure 8.6.

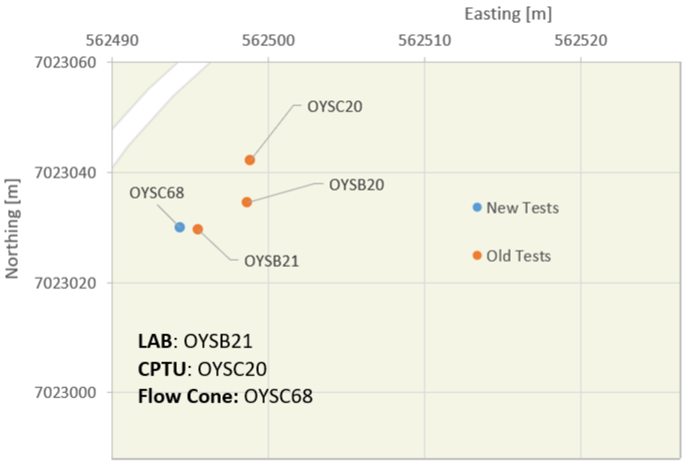

LAB: OYSB21
CPTU: OYSC20
Flow Cone: OYSC68

Figure 8.6: Evaluated positions at test location 2.

Figure 8.7 shows the compiled results of hydraulic conductivity, limited to range 6.0 to 12.0 m depth, as only old CPTU OYSC20 goes deeper into a gravelly sand layer.

Below 7.0 m depth, both estimates of K from CPTU display similar results overall, with only a few variations that are mostly short depth duration. Both CPTU estimates concur with calculated K from Flow Cone at depth 7.9 and 10.0 m, see FC1 and FC2 in Figure 8.7.

FC2 is set to the assumed value of stabilized head from initial constant flow rate test, see Section 6.2.6. In Table 6.11, a theoretical min/max range was established. This is shown in Figure 8.7 by the horizontal solid green line. The concluded theoretical range is amplified by the concurring results of the CPTU estimates, but lack corroboration from the horizontal laboratory tests 2Af and 2Bf. Due to this, the minimum value of K derived from FC2 is expected to be higher.

Hydraulic conductivity from laboratory tests display K spanning one value of exponential power in difference. All frozen specimens are deemed disturbed and compacted from initial fabric state. This indicates that an even higher hydraulic conductivity could be present in-situ. However, the images of triaxial specimens in Section 7.1 reveals much liquefied fine material at the porous discs. Also the interior soil shows sign of wet, rearranged soil fabric. This indicates particle migration and rearrangement, high hydraulic gradients or turbulent flow through the specimen, resulting in a higher hydraulic conductivity. The GSD properties reveal variability in content, as the vertical specimen from the centre of the original 103 mm core, has a clay content of 12.0 %, while the horizontal specimens is at around 3.0 - 4.0 %. All these factors have an impact on the hydraulic conductivity.

Nevertheless, the hydraulic profile presented in Figure 8.7 with K suggested by CPTU estimates, confirmed by FC1 at 7.9 m depth and interpret to be within acceptable range for around FC2 at 10.0 m depth is recommended for test location 2.

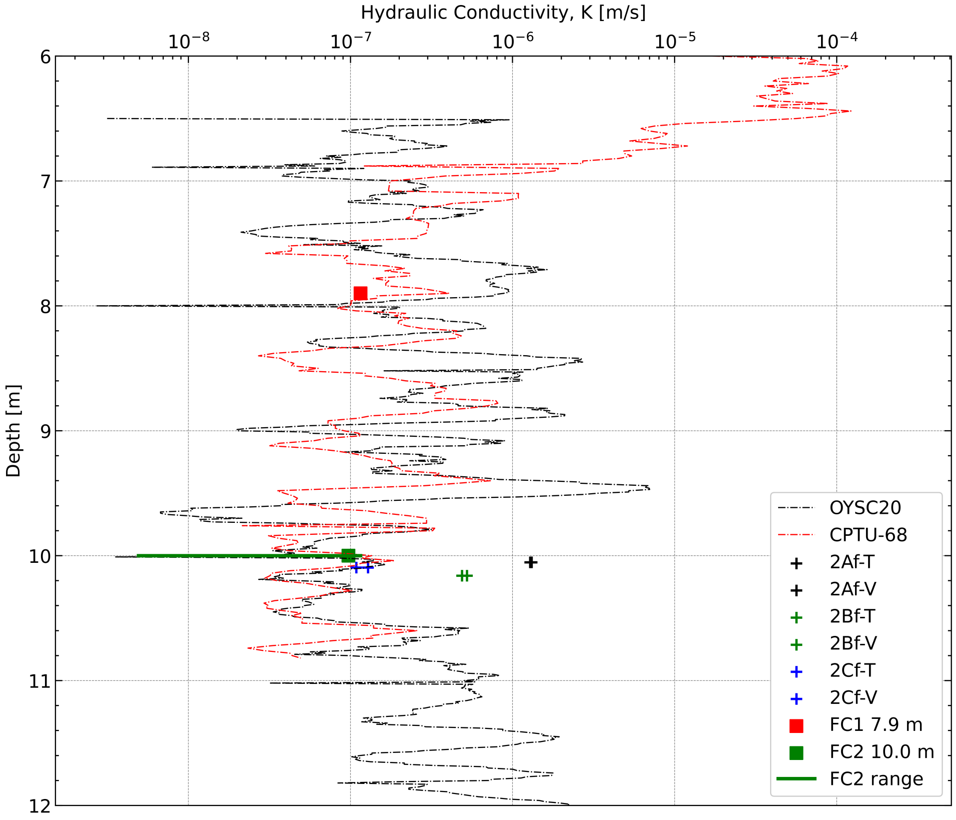

Figure 8.7: Compiled results of hydraulic conductivity and recommended profile at test location 2. Abbreviations T and V represents target pressure or volume ramp method, while FC stands for Flow Cone.

8.3 Evaluation of Interpretation Methodology for Flow Cone and HPT

Different methodologies was employed for interpretation and calculation with measured data from field tests Flow Cone and HPT, while well known methods was used for in-situ falling head tests and hydraulic test. Through comparison and discussion of hydraulic results in previous section and fresh field experience from working with the tools, the different methodologies for Flow Cone and HPT are evaluated. Similar for both tools is that they are only evaluated under saturated conditions for granular soil mixtures in this thesis.

8.3.1 HPT

One of the key limitations for estimating hydraulic conductivity using the HPT tool is the single outlet port. As the water is injected on only one side, at fairly high flow rates and from a relative small outlet port, it is unknown how the flow pattern truly behaves while advancing the probe down into the soil. The flow can move up along the rods while advancing or wash out the surrounding soil, creating hydraulic fracturing while it advances.

One of the fundamental approximations of HPT is that the excess pore pressure generated by penetration has dissipated by the time the outlet port passes a given depth. This has huge impact, as all the models is based on valid Darcy's law, using corrected HPT pressure P_c and flow rate Q with empirical factor or other parameters. To uphold this approximation, the outlet port with pressure sensor is located 406 mm from the probe tip. This may not be enough for certain soil conditions as undrained clay or partially-drain contractive silts. Also during probe advancement, the generated high stress along and near the probe tip cause local shear failure, like for the CPTU, leading to plasticized soil being pushed to the side and creating a disturbed zone. This leads to volumetric change, i.e. alters void ratio, along with excess pore pressure, which also changes the hydraulic conductivity. In complex soil layers with mixed fractions, these effects are worse than for a singe fraction sediment, as the compaction, i.e. disturbed zone, can be greater with finer grains filling in voids between larger grains. The only model that takes this partially into consideration is the HPT BO approach, see Section 3.7.3. In this thesis, the hydraulic efficiency factor in Equation (3.14) was set to value 1.0, representing zero loss of hydraulic conductivity due to zone disturbance. Tuning this to create best fit estimation of K compared to results from other in-situ tests is not very efficient in the short term view. If committed, a database with best fit efficiency factors correlated to cheaper, more used methods of in-situ sounding or soil stratification could be established.

HPT BO in Section 3.7.3 is the only interpretation methodologies that takes penetration speed into account, see Equation (3.14). This allows for penetration speed v and flow injection rate Q to be fine tuned for soil formations with expected low hydraulic conductivity, allowing the flow more time to penetrate the surrounding soil reducing the risk of up-rod stream of water and stabilizing pressure P_{tot}. This should offer better and more stable estimations of hydraulic conductivity in low permeable soil formations.

As seen by the comparison plots and recommended hydraulic profiles in Section 8.1, the method of best fit was a inverse-modeled, i.e. site specific tuned, HPT ZH presented in Section 3.7.4. This was largely due to similar soil stratification and the linear nature of Equation (3.15), not taking low flow-pressure relationships into consideration, which might lead to deviation from Darcy's law. The HPT MC empirical model, see Section 3.7.2, avoids this through Equation (3.13) logarithmic nature and forced boundary limits. This is why the HPT MC had overall the worst fit compared to the falling head tests in Section 8.1.

Common for all methods is the non-stable, flickering and jumping behaviour in the plots of hydraulic conductivity. Overall, HPT BO approach was most stable, as due to the final part of the Equation (3.14), because when corrected pressure P_c gets high the more it limits the K due to its negative exponential. The logarithmic Equation (3.13) from HPT MC approach will be stable within its optimal range, but less stable in low permeable formations. The linear HPT ZH approach of Equation (3.15) will be as unstable as its inputs, therefore demanding good measurements to be precise. This also goes for all methodologies, as more stable pressure and flow, will result in more stable estimates of K.

8.3.2 Flow Cone

In this thesis, the stationary phase of Flow Cone testing has been investigated. Flow Cone is designed to produce a radial flow through a cylindrical filter and by allowing the excess pore pressure commenced by the probe advancement to dissipate, the volumetric change at the beginning of stationary test phase should reset. Flow Cone is not intended for use in clays, i.e. undrained condition, but as silt can behave partially drained, the dissipation of initial excess pore pressure can take a while. This was eminent of for both stopping depth, at 7.9 and 10.0 m. The dissipation of initial excess pore pressure at 7.9 m depth is shown in Figure 8.8. Even starting with lower max pressure u_f than some of the dissipation tests after constant flow rate, see Figure 6.5, the dissipation took about 683 sec. This is almost twice as long as for the dissipation of excess pore pressure after constant flow rate tests, even for the first two tests at 7.9 m depth, were no disturbance by high gradient was concluded. As the velocity of the dissipation is similar to the followed constant flow rate tests, the duration is longer for the initial excess pore pressure. This implies that constant flow rate tests influences the dissipation of applied excess pore pressure. Due to this, along with the very high ratios of pore pressure versus effective stress in both directions and the behaviour of corrected measured pore pressure u_f at increasing constant flow rates, suggests that the method dealing with estimation of coefficient of consolidation, should not be implemented after constant flow rate tests, but rather as individual stationary tests. The use of time factor T^* at assumed position of 10 radii behind cone shoulder, see Section 3.6.2, fits overall good for ranges between 80.0 - 20.0 %, but evaluation for the top and bottom part should be performed. Unfortunately, no hydraulic conductivity was derived from estimated coefficients of horizontal consolidation because of time limitation.

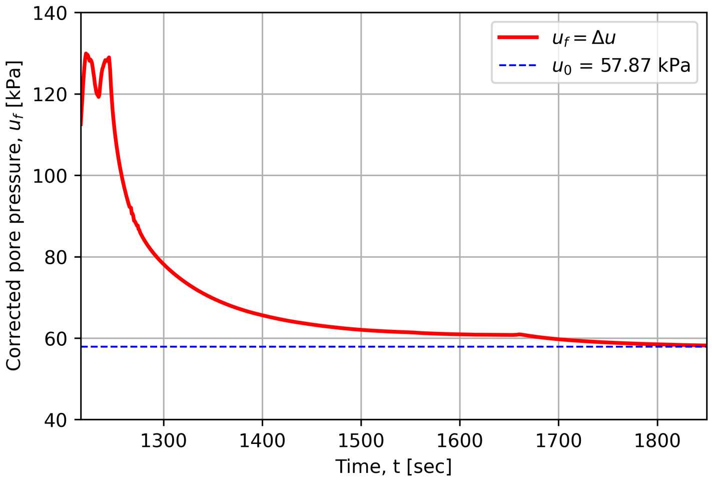

Figure 8.8: Initial excess pore pressure after stop penetration for Flow Cone stationary test at depth 7.9 m. Also showing some of the pressure during penetration.

The simple method for calculation of hydraulic conductivity is based on Darcy's law. As discussed in Section 8.2, the fit of employed method is estimated to be good, compared to CPTU estimates. Unfortunately, during field procedure, the high values of u_f, i.e. hydraulic gradient, was hard to spot in the operating software. This lead to previously mentioned problems with hydraulic fracture, disturbance, radial plasticizing and elastic compression. More trials of Flow Cone, with more care of pore pressure versus effective stress ratios should be performed.

Chapter 9

Conclusion and Recommendations for Further Work

9.1 Conclusion

In this study, the field tests performed at Øysand characterized the in-situ hydraulic conductivity as recommended hydraulic profiles for two test locations. Methodologies were evaluated and some suggested ways forward is presented.

Hydraulic conductivity calculated from Flow Cone using constant rate method shows promising results for Øysand sand. Only two depths were trialled with several constant flow rates tested. Unfortunately, control over in-situ pore pressure versus effective stress ratio was lost and employed flow rates led to hydraulic fracture, assumed particle migration and disturbance of surrounding soil. Only three out of twelve flow rates could be interpret with current constant flow rate method, were no disturbance was concluded.

Interpretation of dissipation of initiated excess pore pressure after constant flow rate tests were performed. Estimated coefficients of horizontal consolidation is suggested, but should be affirmed. Dissipation tests is suggested to be performed in own test depths, but this should be affirmed by more tests with lower Δu and no assumed disturbance under constant flow rate tests.

Unfortunately, the newest version prototype of the hydraulic module, FCHM2 did not function as designed. This would enable pore pressure u_f to be measured directly at mid filter position.

The empirical models for estimation of hydraulic conductivity using the HPT is very site specific and limited by model limits. Further development of more site specific empirical models could eventually increase accuracy of HPT, if model criterion could be linked to stratification and in-situ conditions.

Physical approach by (Borden et al., 2021) for estimation of hydraulic conductivity demands fine tuning of parameters penetration speed and flow rate and the hydraulic efficiency factor for optimization of accurate values for low permeable zones.

The electric conductivity measurements by the Wenner array of the HPT is a handy tool to indicate clay content in soil sediments. Clay content at indicated depths, were confirmed by one GSD test.

Considering field operations, HPT is faster and slightly more mobile than Flow Cone. At present state both tools requires moving and handling of relative much equipment for setup at another position. Liquid water is required for both tools, limiting their use during winter season in Norway.

Laboratory tests of frozen ground specimen from Øysand experienced substantial axial strain under thawing procedure. Soil sample quality is therefore concluded as bad and in-situ fabric is disturbed. Hydraulic testing was nevertheless performed, without any conclusion to anisotropy. Hydraulic conductivity relates to a certain degree with results from performed field tests. Performed GSD test confirmed clay content at greater depths for test location 1.

9.2 Recommendations for Further Work

The Flow Cone system should be tested in a environment that visualize the flow pattern and behaviour of the soil under different pore pressure u_f to investigate hydraulic fracture, particle migration and plastification. This could also confirm the assumed radial flow pattern in this study. Both constant flow rate and dissipation should be tested. This could be performed in a big 3-D sandbox with glass walls. Other soil fractions and mixtures should also be tested, especially silt, to see the effects of partially drainage condition in live action.

Further, basic testing of the constant flow rate method should be performed to gain confidence in this method. This should be performed on various granular soils, to gain knowledge and benchmark results for later comparison.

A methodology that incorporates a spherical model of flow for Flow Cone on compressible soil should be further investigated and trialled. Spherical flow could appear in compressible soils, as partially drained conditions would lead to volumetric changes in the soil. Also, the volume factor or flexibility of the Flow Cone system should be investigated and determined.

The employed shape factor for Flow Cone filter should be controlled by using FEM simulations and further investigated in more complex soil models to fully represent the flow geometry, anisotropy of the soil, geometry of the soil cavity and boundary conditions.

The flow pattern created by the HPT should be investigated during penetration run. This would lead to more knowledge about the impact the single, small outlet port has on the surrounding soil and if any anomalies in the flow direction is present.

The physical approach named HPT BO in this thesis should be investigated using correct flow rate and penetration speed in semi-permeable soil formations, like test location 1 at Øysand. This could affirm the approach and help HPT take compressibility of the soil into consideration.

Bibliography

Andersen, A. and P. Kolstad (1980). *The NGI 54 mm samplers for undisturbed sampling of clays and representative sampling of coarser materials*. OCLC: 36635429. Oslo: Norges Geotekniske Institutt. ISBN: 978-82-546-0068-9.

Bihs, Annika, Mike Long, Steinar Nordal, 1 Department of Civil and Environmental Engineering, Norwegian University of Science and Technology (NTNU), 7491 Trondheim, Norway et al. (2020). 'Geotechnical characterization of Halsen-Stjørdal silt, Norway'. In: *AIMS Geosciences* 6.3, pp. 355–377. ISSN: 2471-2132. DOI: `10.3934/geosci.2020020`. URL: `http://www.aimspress.com/article/10.3934/geosci.2020020`.

Bihs, Annika, Mike Long, Steinar Nordal and Priscilla Paniagua (2021). 'Consolidation parameters in silts from varied rate CPTU tests'. In: *AIMS Geosciences* 7.4, pp. 637–668. ISSN: 2471-2132. DOI: `10.3934/geosci.2021039`. URL: `http://www.aimspress.com/article/doi/10.3934/geosci.2021039`.

Bjerrum, L. et al. (June 1972). 'Hydraulic fracturing in field permeability testing'. In: *Géotechnique* 22.2, pp. 319–332. ISSN: 0016-8505, 1751-7656. DOI: `10.1680/geot.1972.22.2.319`. URL: `https://www.icevirtuallibrary.com/doi/10.1680/geot.1972.22.2.319`.

Borden, Robert C., Ki Young Cha and Gaisheng Liu (Mar. 2021). 'A Physically Based Approach for Estimating Hydraulic Conductivity from HPT Pressure and Flowrate'. In: *Groundwater* 59.2, pp. 266–272. DOI: `10.1111/gwat.13039`.

Chamberlain, Edwin J. and Anthony J. Gow (Apr. 1979). 'Effect of freezing and thawing on the permeability and structure of soils'. In: *Engineering Geology* 13.1, pp. 73–92. ISSN: 00137952. DOI: `10.1016/0013-7952(79)90022-X`.

Chapuis, Robert P. (Aug. 2012). 'Predicting the saturated hydraulic conductivity of soils: a review'. In: *Bulletin of Engineering Geology and the Environment* 71.3, pp. 401–434. DOI: `10.1007/s10064-012-0418-7`.

Chapuis, Robert P., L. D. Suits and T. C. Sheahan (2009). 'Interpreting Slug Tests with Large Data Sets'. In: *Geotechnical Testing Journal* 32.2, p. 101058. DOI: `10.1520/GTJ101058`.

Chapuis, R.P (1st Oct. 1998). 'Overdamped slug test in monitoring wells: review of interpretation methods with mathematical, physical, and numerical analysis of storativity influence'. In: *Canadian Geotechnical Journal* 35.5, pp. 697–719. DOI: `10.1139/t98-041`.

Collins, K. and A. McGown (June 1974). 'The form and function of microfabric features in a variety of natural soils'. In: *Géotechnique* 24.2, pp. 223–254. DOI: `10.1680/geot.1974.24.2.223`.

Dawidowski, J.B. and A.J. Koolen (Feb. 1987). 'Changes of soil water suction, conductivity and dry strength during deformation of wet undisturbed samples'. In: *Soil and Tillage Research* 9.2, pp. 169–180. DOI: `10.1016/0167-1987(87)90083-3`.

Dejam, Morteza, Hassan Hassanzadeh and Zhangxin Chen (Oct. 2017). 'Pre-Darcy Flow in Porous Media: PRE-DARCY FLOW IN POROUS MEDIA'. In: *Water Resources Research* 53.10, pp. 8187–8210. DOI: `10.1002/2017WR021257`.

Delleur, Jacques W., ed. (16th Nov. 2006). *The Handbook of Groundwater Engineering*. 2nd ed. Boca Raton: CRC Press. 1320 pp. ISBN: 978-0-429-12209-5. DOI: `10.1201/9781420006001`.

Fredlund, D.G., Anqing Xing and Shangyan Huang (1st Aug. 1994). 'Predicting the permeability function for unsaturated soils using the soil-water characteristic curve'. In: *Canadian Geotechnical Journal* 31.4, pp. 533–546. DOI: `10.1139/t94-062`.

Gundersen, A.S. et al. (23rd June 2022). 'Flow cone–new CPTU add-on module trialled in Halden silt'. In: Tonni, Laura and Guido Gottardi. *Cone Penetration Testing 2022*. 1st ed. London: CRC Press, pp. 138–143. DOI: `10.1201/9781003308829-13`. URL: `https://hdl.handle.net/11250/3051158`.

Gundersen, Aleksander S. et al. (2019). 'Field verification tests of the newly developed flow cone tool—In-situ measurements of hydraulic soil properties'. In: *AIMS Geosciences* 5.4, pp. 784–803. DOI: `10.3934/geosci.2019.4.784`.

Hansbo, S. (Feb. 2001). 'Consolidation equation valid for both Darcian and non-Darcian flow'. In: *Géotechnique* 51.1, pp. 51–54. DOI: `10.1680/geot.2001.51.1.51`.

Hvorslev, Mikael Juul (1951). 'Time lag and soil permeability in ground-water observations'. In.

Janbu, N. (1989). *Grunnlag i geoteknikk*. 2. opplag. OCLC: 39260901. Trondheim: Tapir Forlag. ISBN: 978-82-519-0519-0.

Jefferies, M, Davies, M and Pincus, H (1993). 'Use of CPTu to Estimate Equivalent SPT N60'. In: *Geotechnical Testing Journal* 16.4, p. 458. DOI: `10.1520/GTJ10286J`.

Khalifa, M.-Abderahmane O.A., Imam Wahyudi and Pierre Thomas (Dec. 2002). 'New Extension of Darcy's Law to Unsteady Flows'. In: *Soils and Foundations* 42.6, pp. 53–63. DOI: `10.3208/sandf.42.6_53`.

Krage, Chris, Nick Broussard and Jason Dejong (May 2014). 'Estimating rigidity index based on CPT measurements'. In: 3rd International Symposium on Cone Penetration Testing, Las Vegas, Nevada, USA - 2014.

Liu, Gaisheng et al. (Mar. 2012). 'Hydraulic conductivity profiling with direct push methods'. In: *Grundwasser* 17.1, pp. 19–29. DOI: `10.1007/s00767-011-0182-9`.

Lunne, Tom, Peter K. Robertson and John J. M. Powell (1997). *Cone penetration testing in geotechnical practice*. 1. ed. London Weinheim: Blackie Academic & Professional. 312 pp. ISBN: 978-0-7514-0393-0.

M. C. Powers (1953). 'A New Roundness Scale for Sedimentary Particles'. In: *SEPM Journal of Sedimentary Research* Vol. 23. ISSN: 1527-1404. URL: `https://pubs.geoscienceworld.org/jsedres/article/23/2/117-119/112811`.

Martínez, Francisco G. H. et al. (2017). *Piezoprobe test interpretation on soft clay*. In: *19th International Conference on Soil Mechanics and Geotechnical Engineering (Seoul)*.

McCall, Wes (28th Mar. 2013). 'Using Hydraulic Profiling Tool (HPT) Logs for Site Characterization'. Webinar. Webinar. URL: `https://geoprobe.com/literature/hpt-webinar-presentation` (visited on 2nd May 2023).

McCall, Wesley and Thomas M. Christy (June 2020). 'The Hydraulic Profiling Tool for Hydrogeologic Investigation of Unconsolidated Formations'. In: *Groundwater Monitoring & Remediation* 40.3, pp. 89–103. DOI: `10.1111/gwmr.12399`.

Mitchell, James Kenneth and Kenichi Soga (2005). *Fundamentals of soil behavior*. 3rd ed. OCLC: ocm56942499. Hoboken, N.J: John Wiley & Sons. 577 pp. ISBN: 978-0-471-46302-3.

Oda, Masanobu (June 1977). 'Co-Ordination Number and its Relation to Shear Strength of Granular Material'. In: *Soils and Foundations* 17.2, pp. 29–42. DOI: `10.3208/sandf1972.17.2_29`.

Quinteros, Santiago (2022). 'On the initial fabric and triaxial behaviour of an undisturbed and reconstituted fluvial sand'. PhD thesis. Imperial College London.

Quinteros, Santiago et al. (2019). 'Øysand research site: Geotechnical characterisation of deltaic sandy-silty'. In: *AIMS Geosciences* 5.4, pp. 750–783. DOI: `10.3934/geosci.2019.4.750`.

Quinteros, V. Santiago and J. Antonio H. Carraro (Jan. 2023). 'The initial fabric of undisturbed and reconstituted fluvial sand'. In: *Géotechnique* 73.1, pp. 1–15. DOI: `10.1680/jgeot.20.P.121`.

Ratnam, S., K. Soga and R. W. Whittle (Sept. 2001). 'Revisiting Hvorslev's intake factors using the finite element method'. In: *Géotechnique* 51.7, pp. 641–645. DOI: `10.1680/geot.2001.51.7.641`.

Robertson, P K and Ce (Fear) Wride (1st June 1998). 'Evaluating cyclic liquefaction potential using the cone penetration test'. In: *Canadian Geotechnical Journal* 35.3, pp. 442–459. DOI: `10.1139/t98-017`.

Robertson, P. (2009). 'Estimating in-situ soil permeability from CPT & CPTu'. In: URL: `https://www.semanticscholar.org/paper/Estimating-in-situ-soil-permeability-from-CPT-%26-Robertson/143ebf250cd68ec7d6699042af6add0ec008c252`.

Robertson, P. K. (1st Feb. 1990). 'Soil classification using the cone penetration test'. In: *Canadian Geotechnical Journal* 27.1, pp. 151–158. DOI: `10.1139/t90-014`.

Robertson, P. K. et al. (1st Aug. 1992). 'Estimating coefficient of consolidation from piezocone tests'. In: *Canadian Geotechnical Journal* 29.4, pp. 539–550. DOI: `10.1139/t92-061`.

Saetersdal, Reidar (Dec. 1981). 'Heaving conditions by freezing of soils'. In: *Engineering Geology* 18.1, pp. 291–305. DOI: `10.1016/0013-7952(81)90068-5`.

Sandven, Rolf et al. (17th Oct. 2017). *Compendium Geotechnics Field and Laboratory Investigations*.

Schneider, James A. et al. (Nov. 2008). 'Analysis of Factors Influencing Soil Classification Using Normalized Piezocone Tip Resistance and Pore Pressure Parameters'. In: *Journal of Geotechnical and Geoenvironmental Engineering* 134.11, pp. 1569–1586. DOI: `10.1061/(ASCE)1090-0241(2008)134:11(1569)`.

Sivathayalan, S and Vaid, Y (2004). 'Evaluation of Static Liquefaction Potential Using Undisturbed Sand Specimens'. In: *Proceedings of the 13th World Conference on Earthquake Engineering, Vancouver, BC, Canada*, pp. 1–6.

Slowiok, M. et al. (23rd June 2022). 'Determination of hydraulic conductivity using HPT & CPTu'. In: *Cone Penetration Testing 2022*. 1st ed. London: CRC Press, pp. 697–702. ISBN: 978-1-00-330882-9. DOI: `10.1201/9781003308829-102`. URL: `https://www.taylorfrancis.com/books/9781003308829/chapters/10.1201/9781003308829-102`.

Standards Norway (7th Jan. 2008). *Eurocode 7: Geotechnical design Part 2: Ground investigation and testing*.

— (5th Jan. 2018a). *Geotechnical investigation and testing Identification and classification of soil Part 1: Identification and description (ISO 14688-1:2017)*.

— (7th Jan. 2018b). *Geotechnical investigation and testing Laboratory testing of soil Part 9: Consolidated triaxial compression tests on water saturated soils (ISO 17892-9:2018)*.

— (5th Jan. 2019). *Geotechnical investigation and testing Laboratory testing of soil Part 11: Permeability tests (ISO 17892-11:2019)*.

Sully, John P et al. (25th Sept. 1999). 'An approach to evaluation of field CPTU dissipation data in overconsolidated fine-grained soils'. In: *Canadian Geotechnical Journal* 36.2, pp. 369–381. DOI: `10.1139/t98-105`.

Teh, C. I. and G. T. Houlsby (Mar. 1991). 'An analytical study of the cone penetration test in clay'. In: *Géotechnique* 41.1, pp. 17–34. DOI: `10.1680/geot.1991.41.1.17`.

Weber, Simon, Francois Duhaime and Robert Chapuis (Oct. 2016). 'Interpreting in situ variable-head permeability tests: An automated Excel spreadsheet program'. In.

Yoshimi, Yoshiaki, Munenori Hatanaka and Hiroshi Oh-oka (Sept. 1978). 'Undisturbed Sampling of Saturated Sands by Freezing'. In: *Soils and Foundations* 18.3, pp. 59–73. DOI: `10.3208/sandf1972.18.3_59`.

Zeh, Rainer M. and Karl Josef Witt (2007). 'The Tensile Strength of Compacted Clays as Affected by Suction and Soil Structure'. In: *Experimental Unsaturated Soil Mechanics*. Ed. by T. Schanz. Vol. 112. Series Title: Springer Proceedings in Physics. Berlin, Heidelberg: Springer Berlin Heidelberg, pp. 219–226. ISBN: 978-3-540-69872-2. DOI: `10.1007/3-540-69873-6_21`.

Zhao, Zhanfeng and Walter A. Illman (Sept. 2022). ‘Improved high-resolution characterization of hydraulic conductivity through inverse modeling of HPT profiles and steady-state hydraulic tomography: Field and synthetic studies’. In: *Journal of Hydrology* 612. DOI: `10.1016/j.jhydrol.2022.128124`.

Appendix A

Borehole log from NGTS Øysand Test Location 1

Borehole log of position OYSB09 from (S. Quinteros et al., 2019).

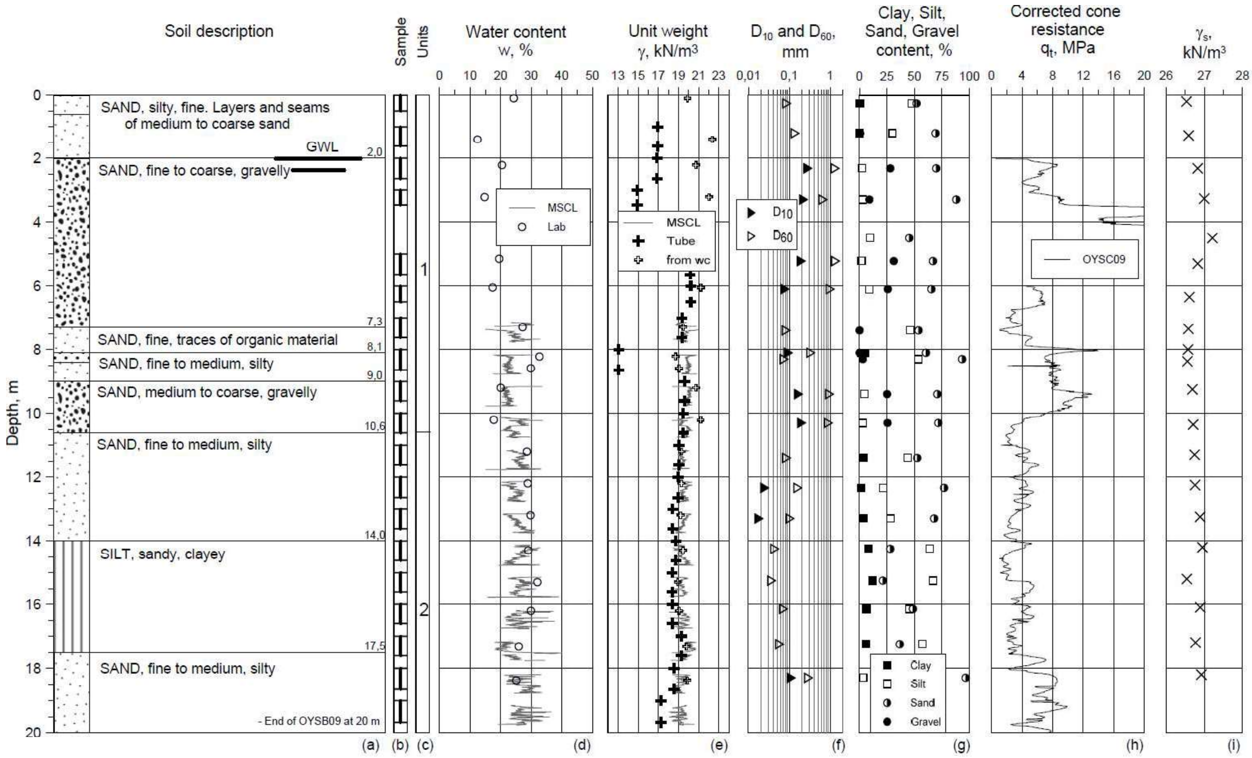

Figure 7. Borehole log (OYSB09). * Multi sensor Core Logging, ** qt =qc + u2(1 − a) after [13].

Appendix B

Borehole log from NGTS Øysand Test Location 2

Borehole logs containing data from several test methods and boreholes around test location 2 from (S. Quinteros, 2022).

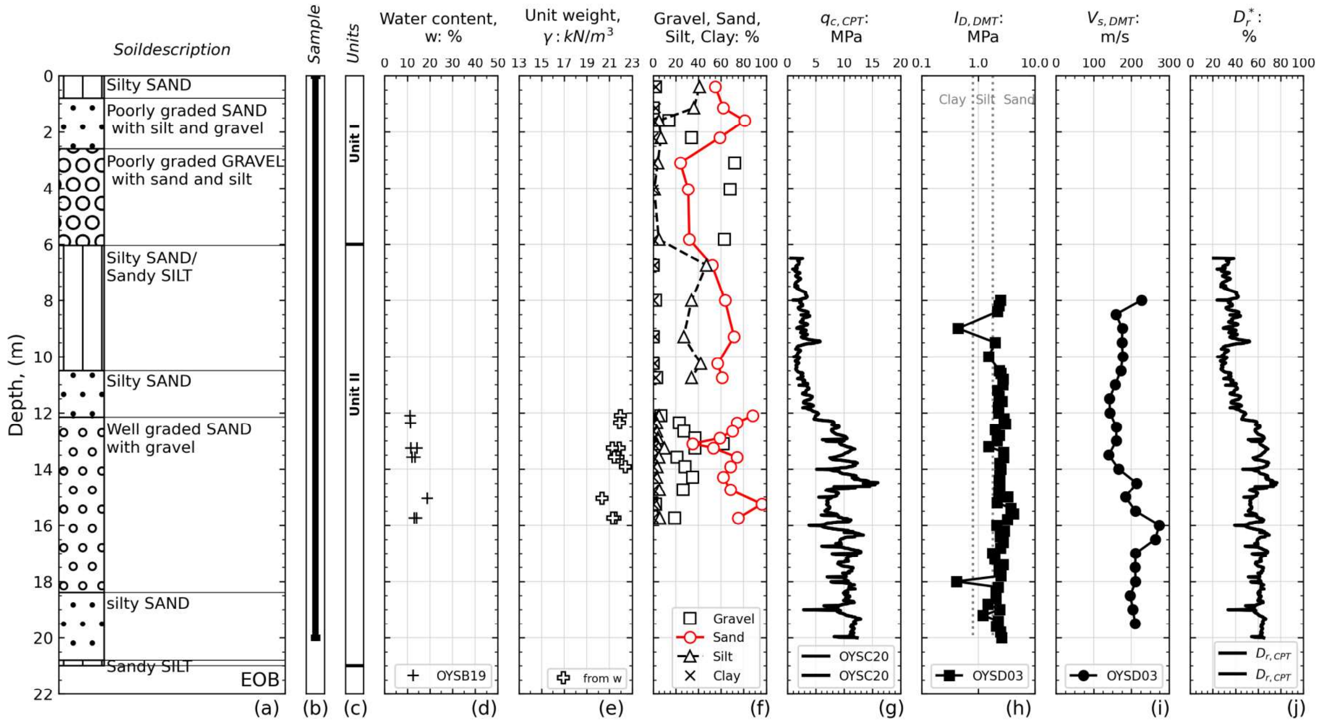

* D_r after Jamiolkowski et al. (2003)

Figure 4.4 Borehole log showing the variation of soil characteristics with depth prior to ground freezing

Appendix C

CPTU Soil Behaviour Type Interpretation

Soil classification charts by (P. K. Robertson, 1990) and (Schneider et al., 2008).

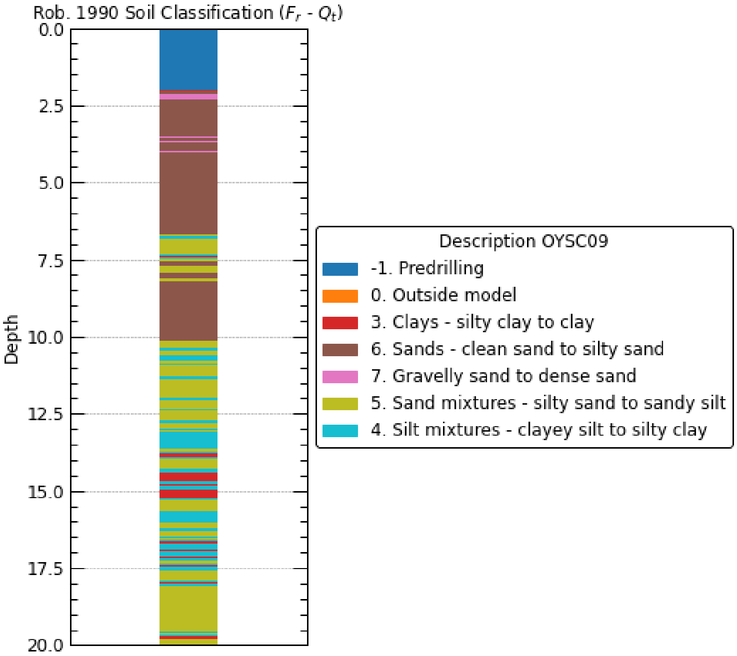
Rob. 1990 Soil Classification (F_r - Q_t)
Depth
0.0
2.5
5.0
7.5
10.0
12.5
15.0
17.5
20.0
Description OYSC09
-1. Predrilling
0. Outside model
3. Clays - silty clay to clay
6. Sands - clean sand to silty sand
7. Gravelly sand to dense sand
5. Sand mixtures - silty sand to sandy silt
4. Silt mixtures - clayey silt to silty clay

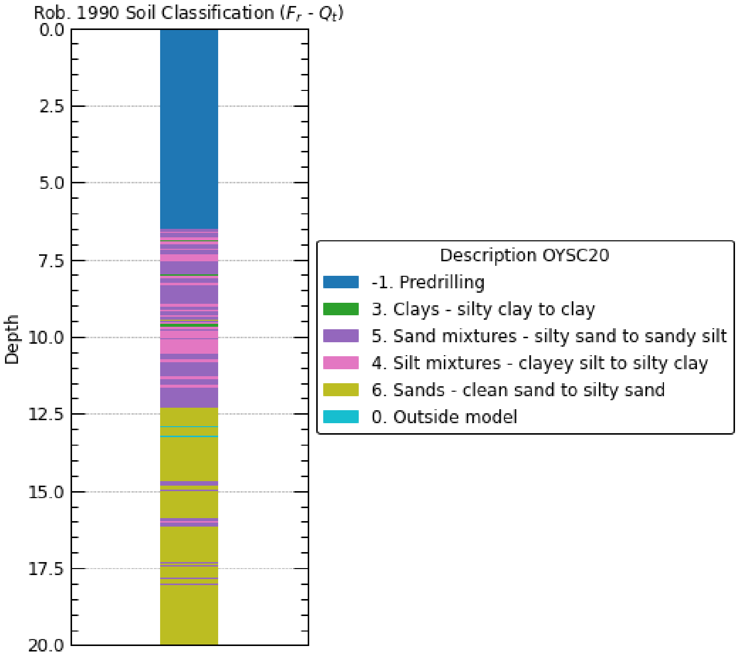
Rob. 1990 Soil Classification (F_r - Q_t)
Depth
0.0
2.5
5.0
7.5
10.0
12.5
15.0
17.5
20.0
Description OYSC20
-1. Predrilling
3. Clays - silty clay to clay
5. Sand mixtures - silty sand to sandy silt
4. Silt mixtures - clayey silt to silty clay
6. Sands - clean sand to silty sand
0. Outside model

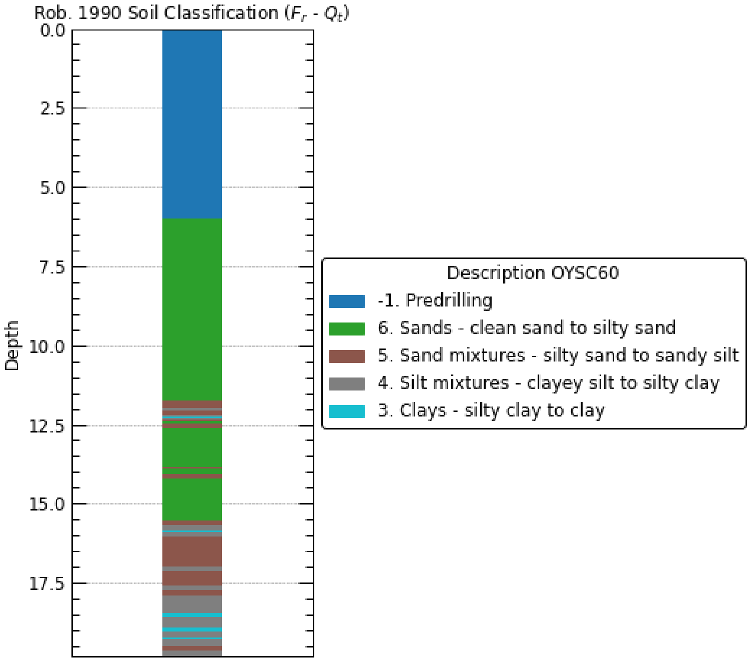
Rob. 1990 Soil Classification (F_r - Q_t)
Depth
0.0
2.5
5.0
7.5
10.0
12.5
15.0
17.5
Description OYSC60
-1. Predrilling
6. Sands - clean sand to silty sand
5. Sand mixtures - silty sand to sandy silt
4. Silt mixtures - clayey silt to silty clay
3. Clays - silty clay to clay

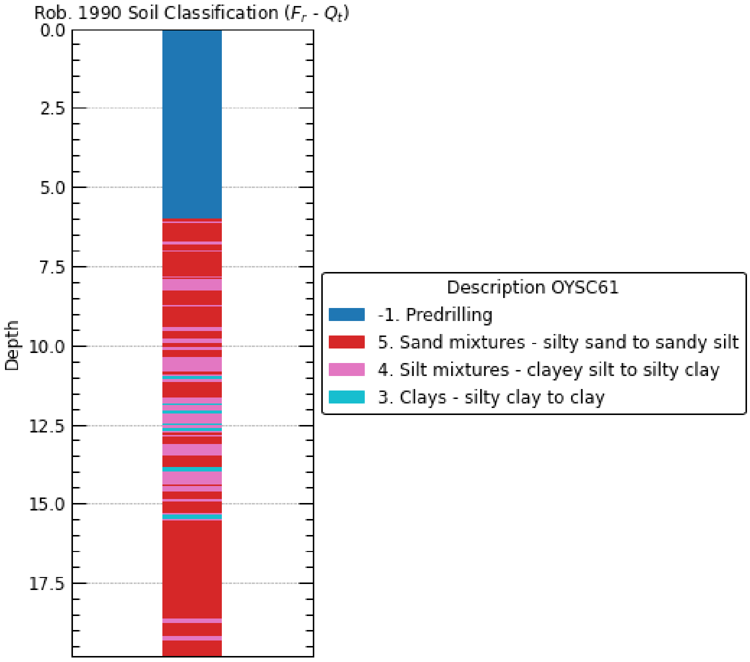
Rob. 1990 Soil Classification (F_r - Q_t)
Depth
0.0
2.5
5.0
7.5
10.0
12.5
15.0
17.5
Description OYSC61
-1. Predrilling
5. Sand mixtures - silty sand to sandy silt
4. Silt mixtures - clayey silt to silty clay
3. Clays - silty clay to clay

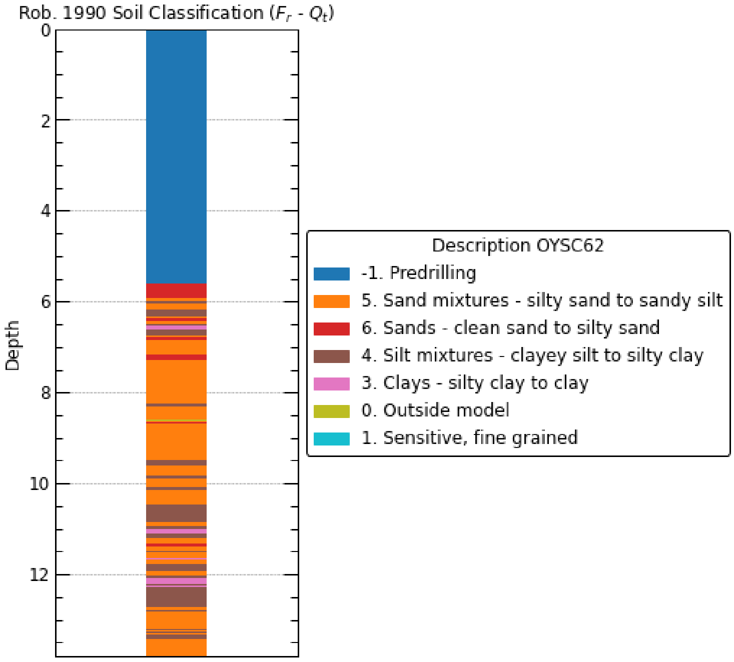
Rob. 1990 Soil Classification (F_r - Q_t)
Depth
0
2
4
6
8
10
12
Description OYSC62
-1. Predrilling
5. Sand mixtures - silty sand to sandy silt
6. Sands - clean sand to silty sand
4. Silt mixtures - clayey silt to silty clay
3. Clays - silty clay to clay
0. Outside model
1. Sensitive, fine grained

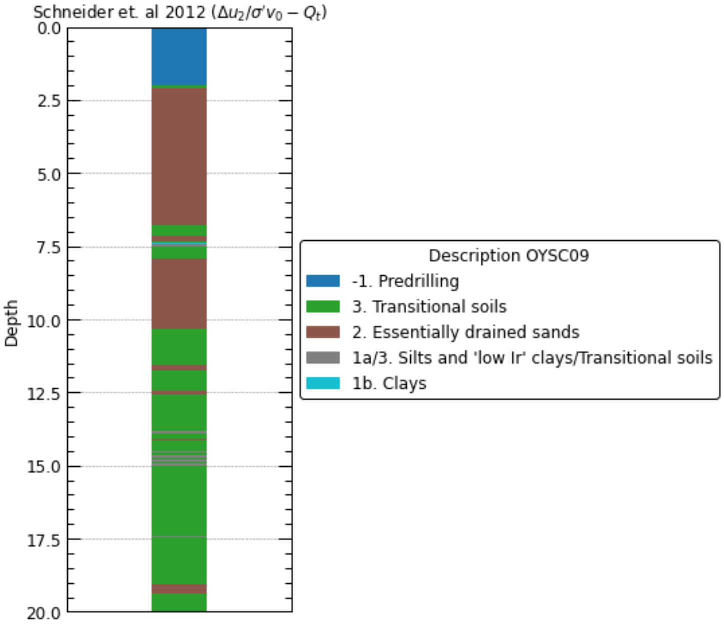
Schneider et. al 2012 ($\Delta u_2/\sigma' v_0 - Q_t$)
Depth
0.0
2.5
5.0
7.5
10.0
12.5
15.0
17.5
20.0
Description OYSC09
-1. Predrilling
3. Transitional soils
2. Essentially drained sands
1a/3. Silts and 'low Ir' clays/Transitional soils
1b. Clays

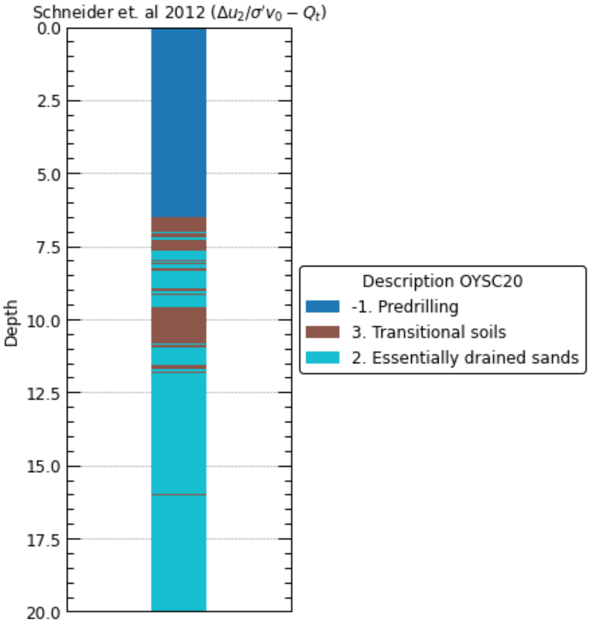
Schneider et. al 2012 ($\Delta u_2/\sigma' v_0 - Q_t$)
Depth
0.0
2.5
5.0
7.5
10.0
12.5
15.0
17.5
20.0
Description OYSC20
-1. Predrilling
3. Transitional soils
2. Essentially drained sands

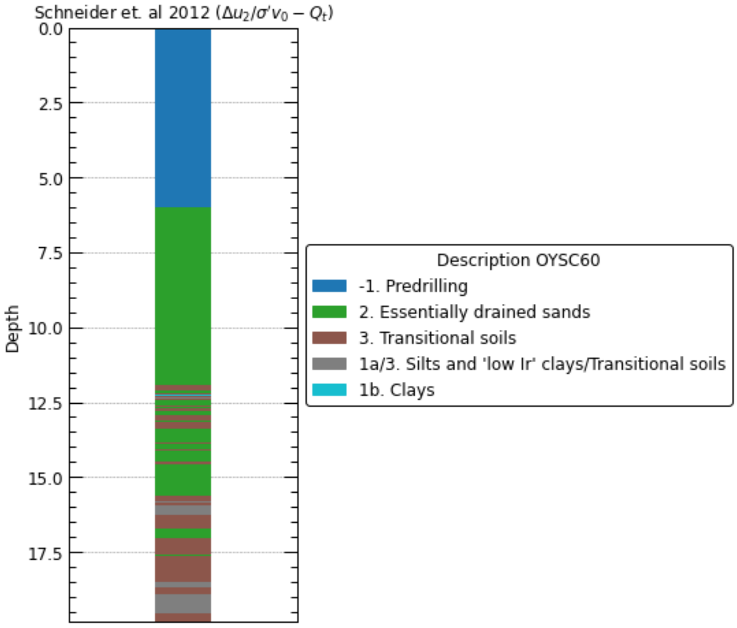
Schneider et. al 2012 ($\Delta u_2/\sigma' v_0 - Q_t$)
Depth
0.0
2.5
5.0
7.5
10.0
12.5
15.0
17.5
Description OYSC60
-1. Predrilling
2. Essentially drained sands
3. Transitional soils
1a/3. Silts and 'low Ir' clays/Transitional soils
1b. Clays

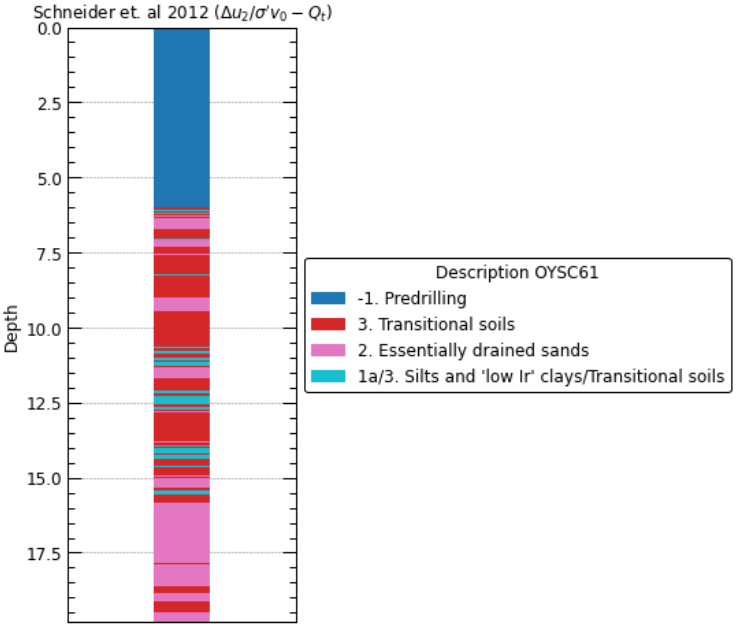
Schneider et. al 2012 ($\Delta u_2/\sigma' v_0 - Q_t$)
Depth
0.0
2.5
5.0
7.5
10.0
12.5
15.0
17.5
Description OYSC61
-1. Predrilling
3. Transitional soils
2. Essentially drained sands
1a/3. Silts and 'low Ir' clays/Transitional soils

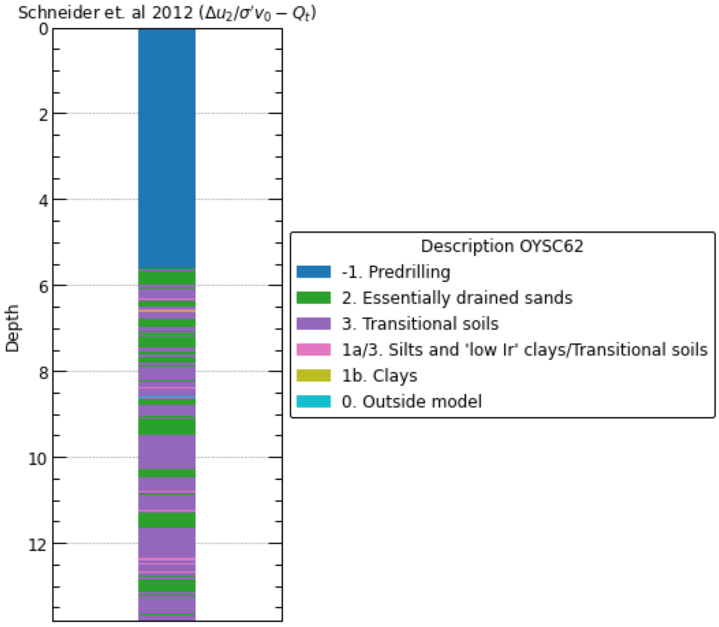
Schneider et. al 2012 ($\Delta u_2/\sigma' v_0 - Q_t$)
Depth
0
2
4
6
8
10
12
Description OYSC62
-1. Predrilling
2. Essentially drained sands
3. Transitional soils
1a/3. Silts and 'low Ir' clays/Transitional soils
1b. Clays
0. Outside model

Appendix D

GSD OYSB09

GSD done by NGI for borehole OYSB09.

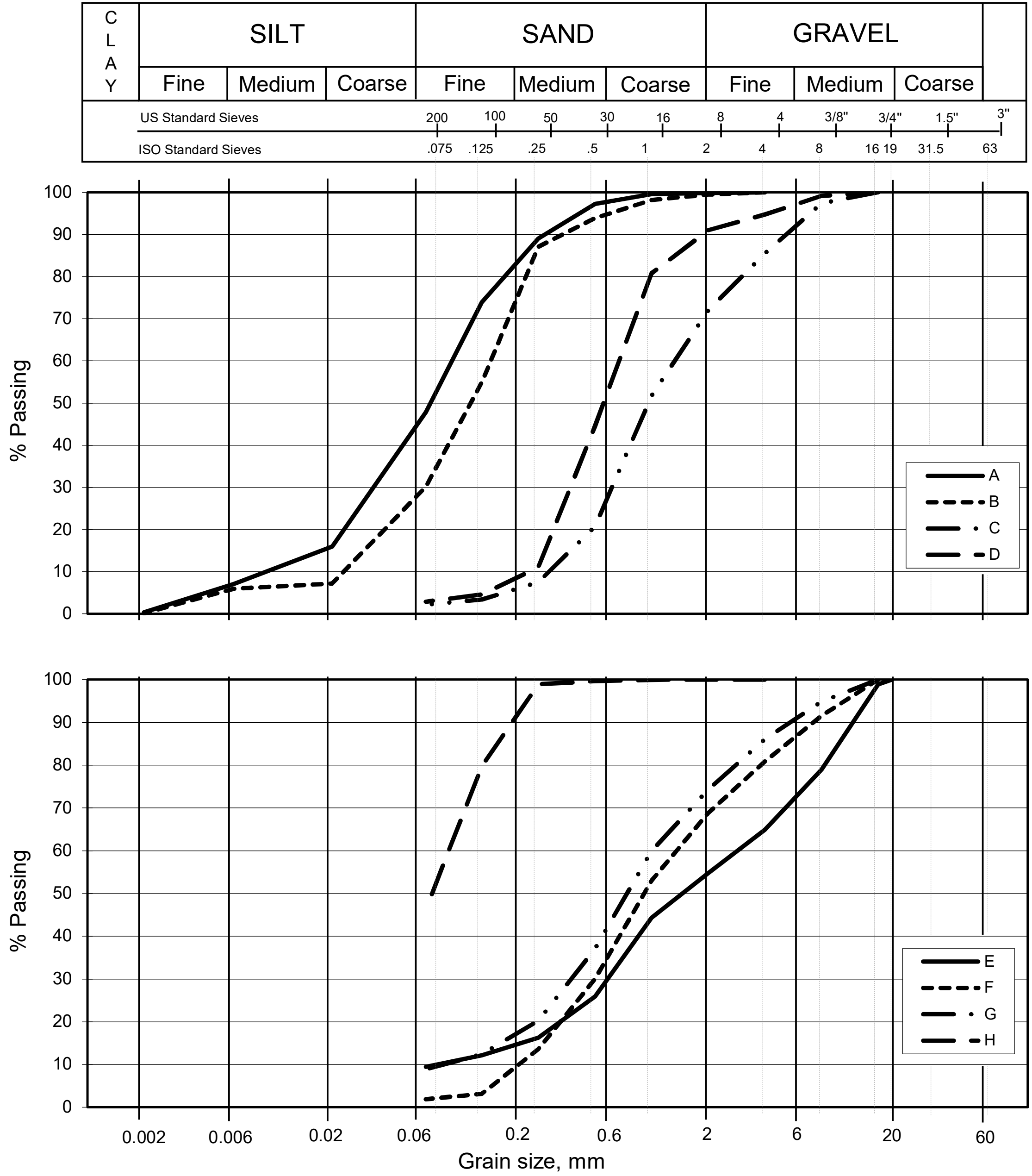

Curve	Boring No.	Sample No.	Depth m	D_{10} mm	D_{60} mm	Clay cont. %	Soil Description	Method dry/wet-sieving
A	9	1	0.26	0.009	0.087	0.4	SILT, sandy	wet siev. + f.d
B	9	2	1.20	0.023	0.139	0.1	SAND, fine, silty	wet siev. + f.d
C	9	3	2.32	0.285	1.328		SAND, coarse, gravelly	wet sieving
D	9	4	3.30	0.223	0.673		SAND, medium to coarse	wet sieving
E	9	5	4.50	0.073	2.864		Sandy, gravelly material	wet sieving
F	9	6	5.22	0.197	1.360		SAND, medium to coarse, gravelly	wet sieving
G	9	7	6.10	0.078	1.004		SAND, coarse to medium, gravelly	wet sieving
H	9	8	7.40		0.083		SAND, fine	wet sieving

Rev. 2 / Dato 2017-02-15 / Sign. SK

#VALUE!

Norwegian Geotest Sites

Grain size distribution curves OYSB09 0.26 - 7.40 m depth

Document No.	20160154-01-R
Figure No.	OYSB09-PSD-1
Date	2017.05.03
Drawn by / Checked	FI/TSF/JRO/MAS

Curve B: Not according to standard

Curve E: Removed sieving >19mm = 12.14g =2.36%

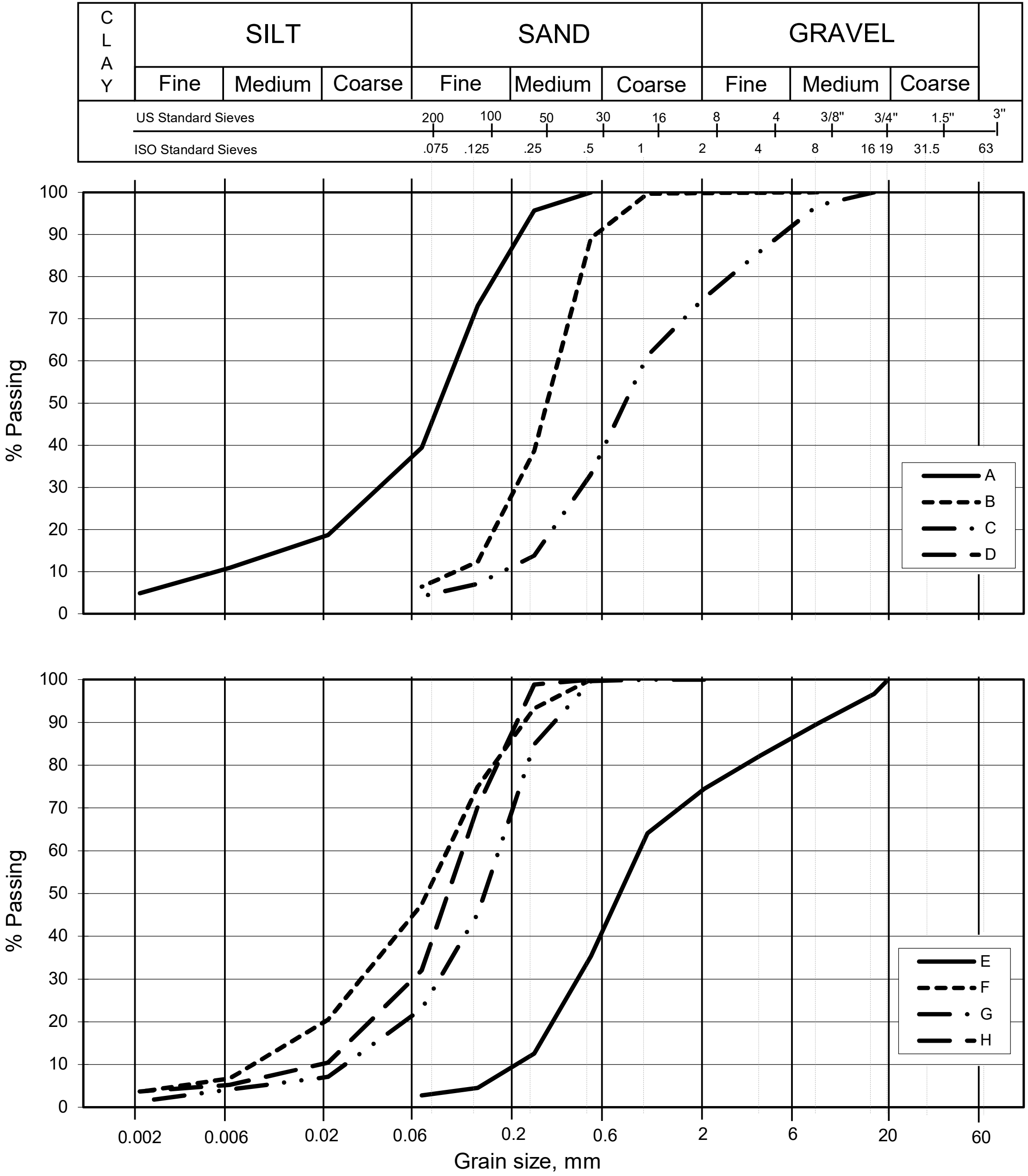

Curve	Boring No.	Sample No.	Depth m	D_{10} mm	D_{60} mm	Clay cont. %	Soil Description	Method dry/wet-sieving
A	9	9	8.10	0.005	0.096	4.9	SAND, fine, silty	fall.drop
B	9	9	8.30	0.095	0.335		SAND, medium	wet sieving
C	9	10	9.40	0.168	0.971			wet sieving
D								
E	9	11	10.30	0.200	0.906		SAND, medium to coarse, gravelly	wet sieving
F	9	12	11.40	0.008	0.086	3.6	Sandy, silty material	fall.drop
G	9	13	12.34	0.025	0.162	1.4	SAND, medium to fine, silty	wet siev. + f.d
H	9	14	13.30	0.018	0.104	3.7	SAND, fine, silty	fall.drop

Rev. 2 / Dato 2017-02-15 / Sign. SK

#VALUE!

Norwegian Geotest Sites

Grain size distribution curves OYSB09 range 8.10 - 13.30 m depth

Document No. 20160154-01-R	
Figure No. OYSB09-PSD-2	
Date 2017.06.19	Drawn by / Checked FI/FP

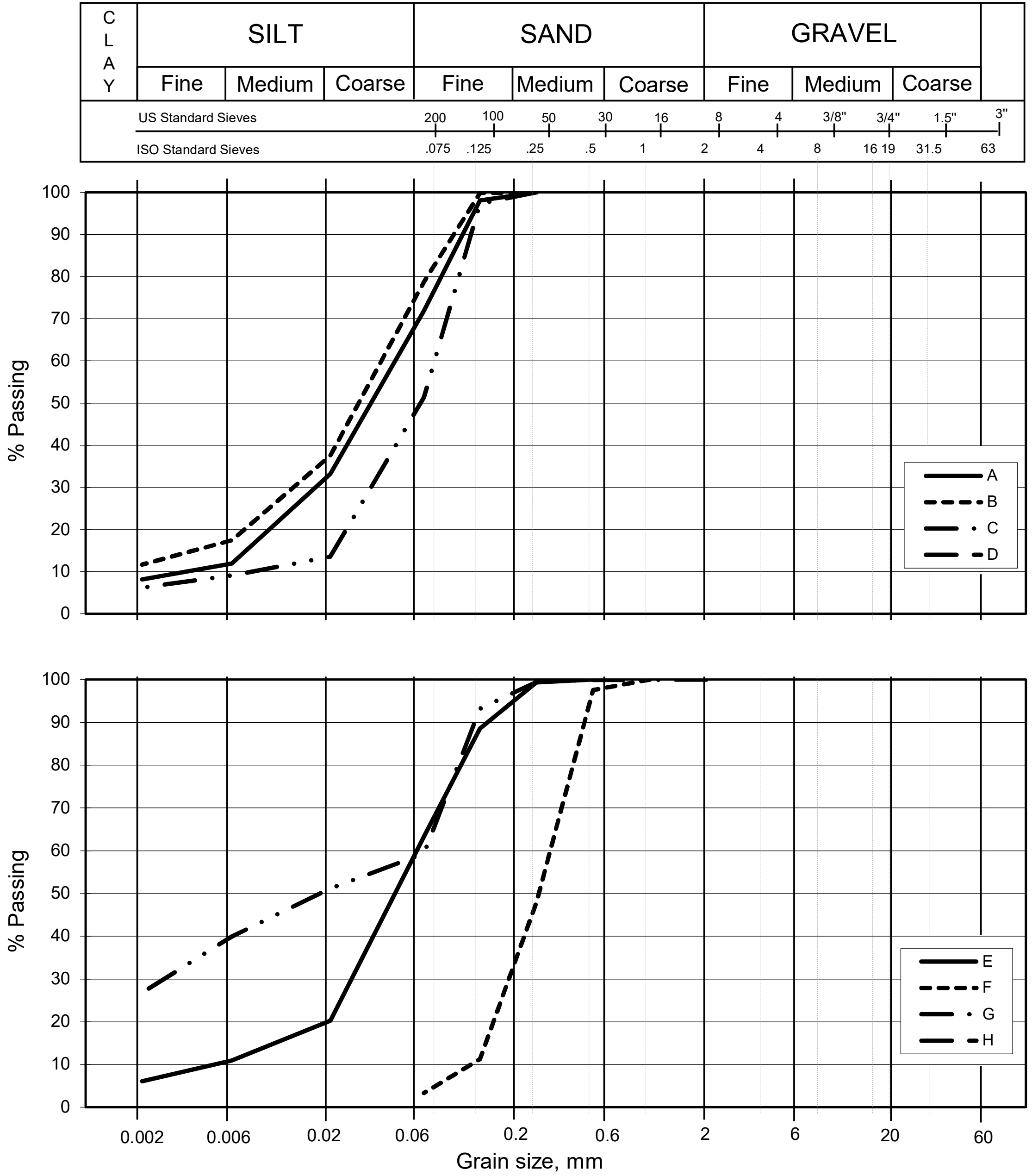

Curve	Boring No.	Sample No.	Depth m	D_{10} mm	D_{60} mm	Clay cont. %	Soil Description	Method dry/wet-sieving
A	9	15	14.25	0.003	0.044	8.2	SILT, sandy, clayey	fall.drop
B	9	16	15.25		0.037	11.7	SILT, sandy, clayey	fall.drop
C	9	17	16.15	0.008	0.072	6.2	SILT, sandy, clayey	fall.drop
D								
E	9	18	17.25	0.005	0.058	6.1	SILT, sandy, clayey	fall.drop
F	9	19	18.30	0.112	0.296		SAND, medium to fine	wet sieving
G	9	20	19.24		0.064	26.8	CLAY, sandy, silty	x siev. + f.d
H								

Rev. 2 / Dato 2017-02-15 / Sign. SK

#VALUE!

Norwegian Geotest Sites

Grain size distribution curves OYSB09 range 14.25 - 19.24 m depth

Document No.
20160154-01-R

Figure No.
OYSB09-PSD-3

Date	Drawn by / Checked
2017.06.19	TSF/FP/JRO

NGI

Appendix E

GSD OYSB21

GSD done by NGI on triaxial trialled frozen samples from OYSB21.

PARTICLE SIZE DISTRIBUTION

acc. to NS-EN 17892-4:2016 and laboratory procedure LLP008

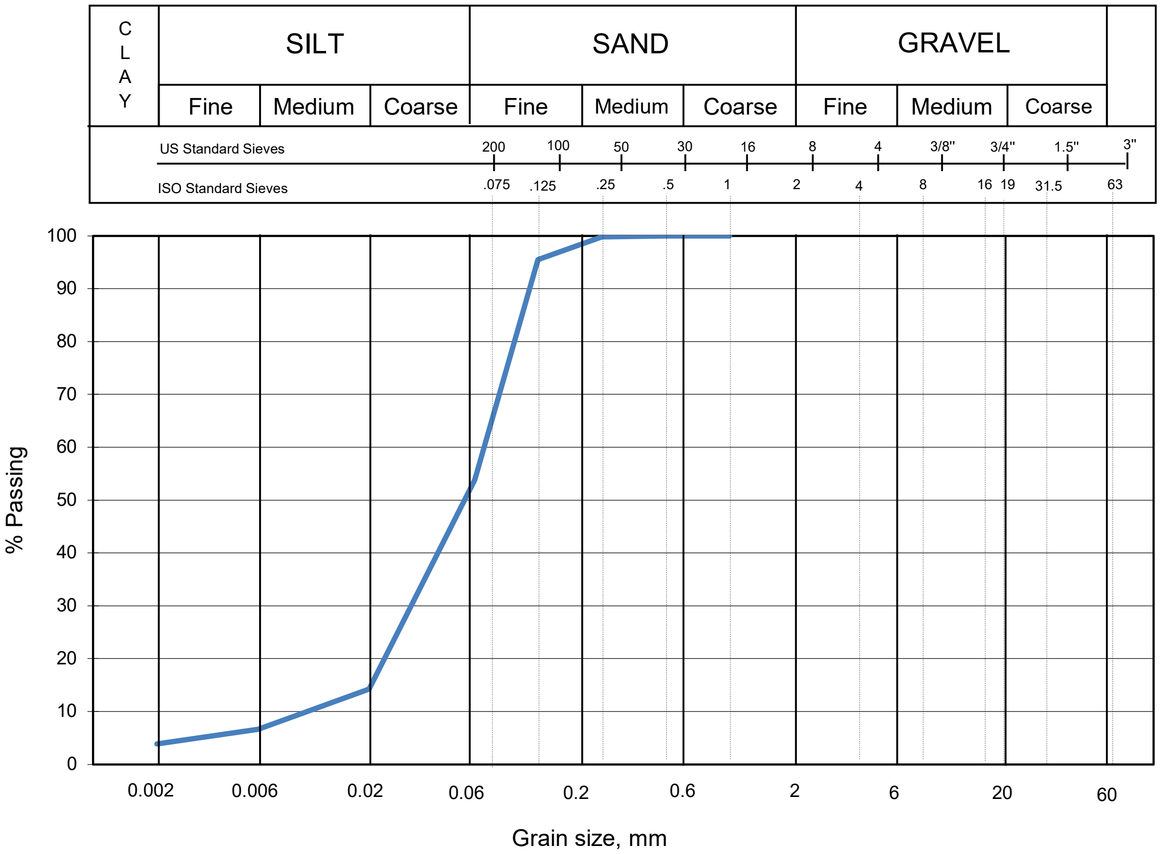

Sieving	
Particle size mm	% passing
63	
31.5	
19	
16	
8	
4	
2	
1	100
0.5	100
0.25	100
0.125	96
0.063	54
0.020	14
0.006	7
0.002	4

Soil description	SILT, sandy
Test method(s)	wet sieving + Falling drop
Assumed particle density (Mg/m3)	2.75

Soil fractions	% dry mass
Very coarse	0.0
Gravel	0.0
Sand	46.2
Silt	49.9
Clay	3.9

Remarks

Minimum total mass not achieved

Grading analysis	
D60 (mm)	0.06972
D10 (mm)	0.01020
CU (D60/D10)	6.833

Rev. 04/2019-06-18/ Sign. FI

SP GeoPerm

Boring: OYSB21

Test: 2Af - Horizontal

Depth: 10.053 m

Document No.
20200275-01-R

Figure No.
OYSB21-2Af

Date	Drawn/appr.
15.05.2023	EvS/KLo

C:\Users\KLo\AppData\Local\Temp\KeyLAB\0d815c86-98f0-4a61-8dd5-4d2e87771ce8\[PSD English Report.xlsm]Sheet 002

PARTICLE SIZE DISTRIBUTION

acc. to NS-EN 17892-4:2016 and laboratory procedure LLP008

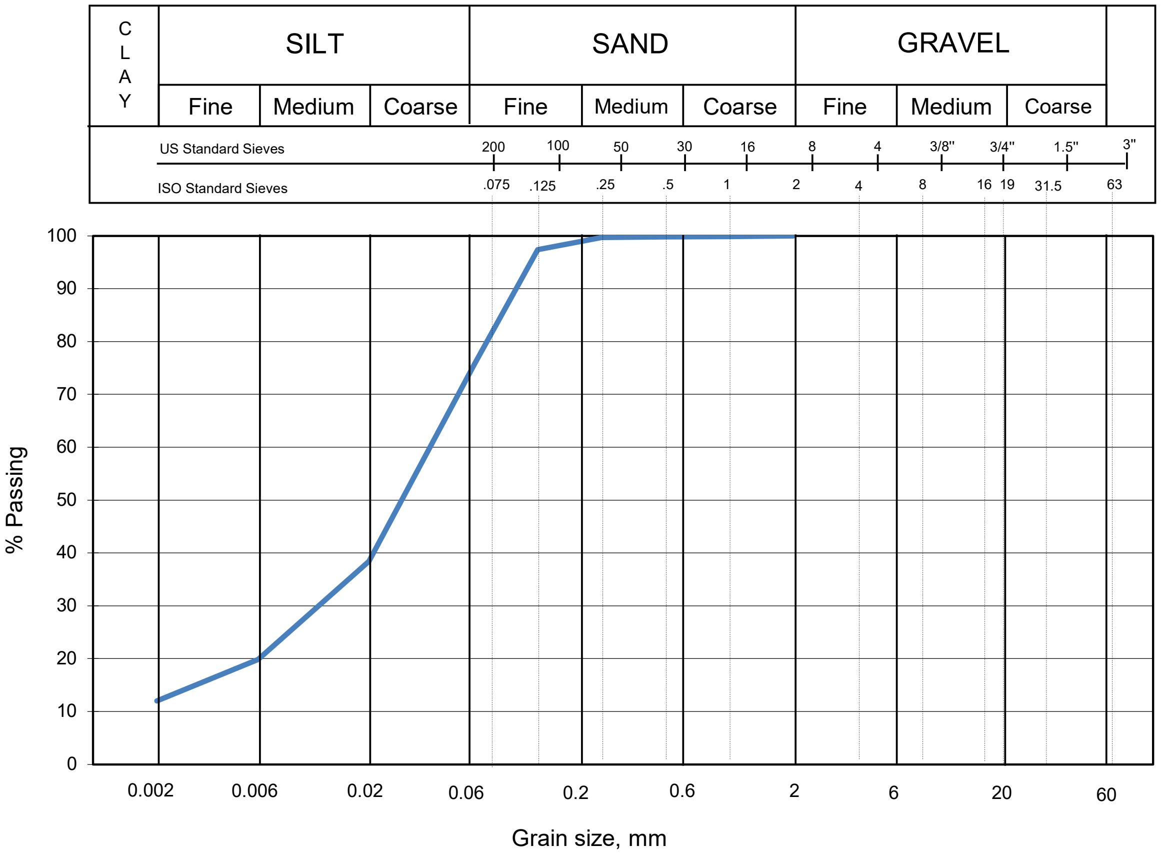

Sieving	
Particle size mm	% passing
63	
31.5	
19	
16	
8	
4	
2	100
1	100
0.5	100
0.25	100
0.125	97
0.063	76
0.020	38
0.006	20
0.002	12

Soil description	SILT, sandy, clayey
Test method(s)	wet sieving + Falling drop
Assumed particle density (Mg/m3)	2.75

Soil fractions	% dry mass
Very coarse	0.0
Gravel	0.0
Sand	24.3
Silt	63.7
Clay	12.0

Remarks

Minimum total mass not achieved

Grading analysis	
D60 (mm)	0.039
D10 (mm)	
CU (D60/D10)	

Rev. 04/2019-06-18/ Sign. FI

SP GeoPerm

Boring: OYSB21

Test: 2Cf - Vertical

Depth: 10.08-10.11 m

Document No.	20200275-01-R
Figure No.	OYSB21-2Cf
Date	15.05.2023
Drawn/appr.	EvS/KLo

C:\Users\KLo\AppData\Local\Temp\KeyLAB\0d815c86-98f0-4a61-8dd5-4d2e87771ce8\[PSD English Report.xlsm]Sheet 003

PARTICLE SIZE DISTRIBUTION

acc. to NS-EN 17892-4:2016 and laboratory procedure LLP008

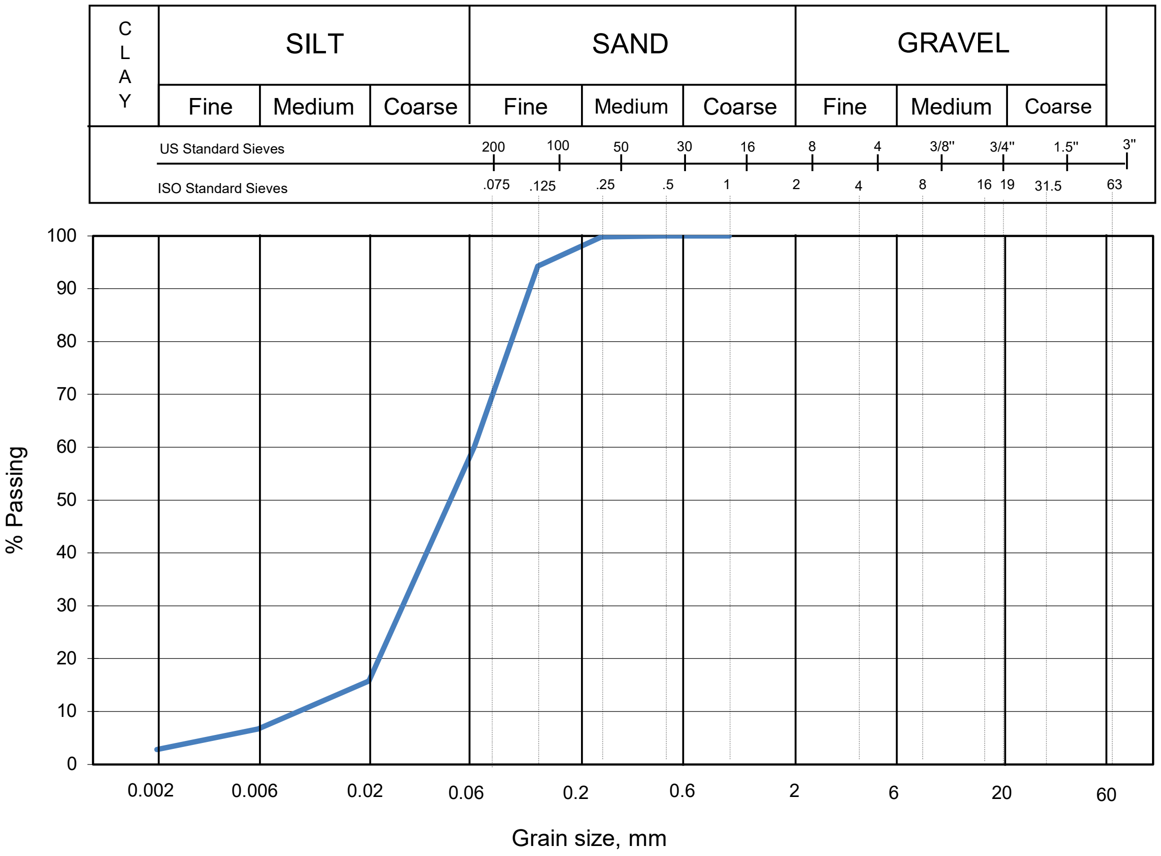

Sieving	
Particle size mm	% passing
63	
31.5	
19	
16	
8	
4	
2	
1	100
0.5	100
0.25	100
0.125	94
0.063	60
0.020	16
0.006	7
0.002	3

Soil description	SILT, sandy
Test method(s)	wet sieving + Falling drop
Assumed particle density (Mg/m3)	2.75

Soil fractions	% dry mass
Very coarse	0.0
Gravel	0.0
Sand	39.8
Silt	57.4
Clay	2.8

Remarks

Grading analysis	
D60 (mm)	0.06276
D10 (mm)	0.00933
CU (D60/D10)	6.729

Rev. 04/2019-06-18/ Sign. FI

C:\Users\KLo\AppData\Local\Temp\KeyLAB\0d815c86-98f0-4a61-8dd5-4d2e87771ce8\[PSD English Report.xlsm]Sheet 004

SP GeoPerm

Boring: OYSB21

Depth: 10.16 m

Test: 2Bf - Horizontal

Document No.
20200275-01-R

Figure No.
OYSB21-2Bf

Date	Drawn/appr.
15.05.2023	EvS/KLo

PARTICLE SIZE DISTRIBUTION

acc. to NS-EN 17892-4:2016 and laboratory procedure LLP008

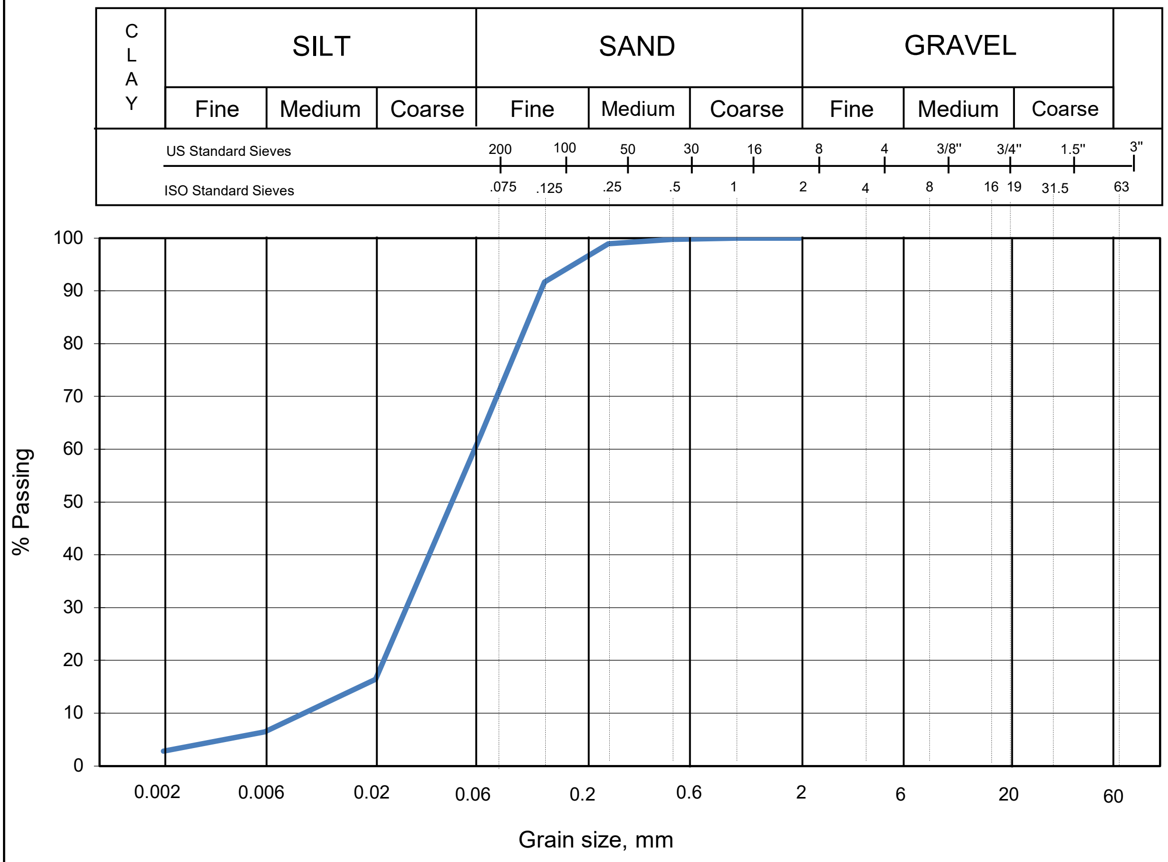

Sieving	
Particle size mm	% passing
63	
31.5	
19	
16	
8	
4	
2	100
1	100
0.5	100
0.25	99
0.125	92
0.063	63
0.020	16
0.006	6
0.002	3

Soil description	SILT, sandy
Test method(s)	wet sieving + Falling drop
Assumed particle density (Mg/m3)	2.75

Soil fractions	% dry mass
Very coarse	0.0
Gravel	0.0
Sand	37.1
Silt	60.1
Clay	2.8

Remarks

Grading analysis	
D60 (mm)	0.05868
D10 (mm)	0.00917
CU (D60/D10)	6.398

Rev. 04/2019-06-18/ Sign. FI

SP GeoPerm

Boring: OYSB10

Tube: 1C - Vertical

Depth: 13.18-13.325 m

Document No. 20200275-01-R	
Figure No. OYSB10-1C	
Date 15.05.2023	Drawn/appr. EvS/KLo

NTNU

Norwegian University of
Science and Technology